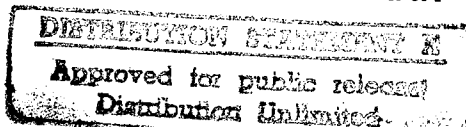# U. S. Army Communications-Electronics Command

Night Vision & Electronic Sensors Directorate

Title: PHOTOREFRACTIVE TUNGSTEN BRONZE CRYSTALS FOR OPTICAL LIMITERS AND FILTERS

Author(s): RATNAKAR R. NEURGAONKAR

Address: ROCKWELL SCIENCE CENTER
THOUSAND OAKS, CA 91360

Type of Report (Final, Interim, etc.):

FINAL TECHNICAL REPORT

Date: JANUARY, 1996

DTIC QUALITY INSPECTED 4

Contract Number

DAAB07-88-C-E243

Report Number

NV-95-C03

19960212 228 Fort Belvoir, Virginia 22060-5806

DISCLAIMER NOTICE

UNCLASSIFIED

Technical Report
distributed by

**DEFENSE
TECHNICAL
INFORMATION
CENTER**

DTIC Acquiring Information-
Imparting Knowledge

UNCLASSIFIED

THIS DOCUMENT IS BEST
QUALITY AVAILABLE. THE
COPY FURNISHED TO DTIC
CONTAINED A SIGNIFICANT
NUMBER OF PAGES WHICH DO
NOT REPRODUCE LEGIBLY.

Rockwell International

Science Center

REPORT DOCUMENTATION PAGE

1a. REPORT SECURITY CLASSIFICATION	1b. RESTRICTIVE MARKINGS
Unclassified	

2a. SECURITY CLASSIFICATION AUTHORITY	3. DISTRIBUTION/AVAILABILITY OF REPORT
	Approved for public release; distribution unlimited
2b. CLASSIFICATION/DOWNGRADING SCHEDULE	

4. PERFORMING ORGANIZATION REPORT NUMBER(S)	5. MONITORING ORGANIZATION REPORT NUMBER(S)
SC5550.FR	

6a. NAME OF PERFORMING ORGANIZATION	6b. OFFICE SYMBOL (If Applicable)	7a. NAME OF MONITORING ORGANIZATION
Rockwell International Science Center		

6c. ADDRESS (City, State and ZIP Code)	7b. ADDRESS (City, State and ZIP Code)
P. O. Box 1058 Thousand Oaks, CA 91358	

8a. NAME OF FUNDING/SPONSORING ORGANIZATION	8b. OFFICE SYMBOL (If Applicable)	9. PROCUREMENT INSTRUMENT IDENTIFICATION NUMBER
		Contract No. DAABO7-88-C-E243

8C. ADDRESS (City, State and ZIP Code)	10. SOURCE OF FUNDING NOS.			
	PROGRAM ELEMENT NO.	PROJECT NO.	TASK NO.	WORK UNIT ACCESSION NO.

11. TITLE (Include Security Classification)

PHOTOREFRACTIVE TUNGSTEN BRONZE CRYSTALS FOR OPTICAL LIMITERS AND FILTERS

12. PERSONAL AUTHOR(S)

NEURGAONKAR, RATNAKAR R.

13a. TYPE OF REPORT	13b. TIME COVERED	14. DATE OF REPORT (Year, Month, Day)	15. PAGE COUNT
FINAL REPORT	FROM 08/10/88 TO 05/31/94	1994, NOVEMBER	

16. SUPPLEMENTARY NOTATION

REPRODUCTION IN WHOLE OR IN PART IS PERMITTED FOR ANY PURPOSE OF THE UNITED STATES GOVERNMENT.

17.	COSATI CODES		18. SUBJECT TERMS (Continue on reverse if necessary and identify by block number)
FIELD	GROUP	SUB-GROUP	Photorefractive, Tungsten Bronze, single crystals, dopants, speed, coupling, growth techniques, optical quality, laser hardening, sensor protection, focusing, external electric field , dark conductivity, electro-optic effect.

19. ABSTRACT (Continue on reverse if necessary and identify by block number)

The photorefractive tungsten bronze SBN:60 and BSKNN-2 crystals were investigated for sensor protection applications with considerable success. Our best photorefractive crystals exhibit response times of ~ 10 µs with coupling > 25 cm-1. This fast response was achieved using suitable dopant combinations, external field and focusing the incoming 1W/cm2 laser beam. Prototype limiters based on these photorefractive crystals have been tested at the University of Arkansas and their overall performance is promising for sensor protection applications.

20. DISTRIBUTION/AVAILABILITY OF ABSTRACT	21. ABSTRACT SECURITY CLASSIFICATION
Same as Report	Unclassified

22a. NAME OF RESPONSIBLE INDIVIDUAL	22b. TELEPHONE NUMBER	22c. OFFICE SYMBOL
R. R. Neurgaonkar	(805)-373-4109	

DoD FORM 1473   Previous editions are obsolete.

TABLE OF CONTENTS

Page

8.1 Growth and optical properties of ferroelectric tungsten

bronze crystals.

8.2 Cr^{3+} - doped SBN:60 single crystals for photorefractive applications.

8.3 Growth and ferroelectric properties of Tungsten Bronze $Sr_{2-x}Ca_xNaNb_5O_{15}$

single crystals.

8.4 Enhancing the response time for photorefractive beam fanning.

8.5 The use of applied electric fields on the photorefractive tungsten

bronze ferroelectrics.

8.6 Enhanced photorefractive beam fanning due to internal and external

electric fields.

8.7 Photorefractive self-focusing and defocusing as an optical limiter.

8.8 Improved photorefractive time response using a cylindrical lens.

8.9 Observation of self-trapping of an optical beam due to the photorefractive effect.

8.10 Photorefractive spatial solitons.

LIST OF FIGURES

◆ Rockwell

LIST OF TABLES

1.0 EXECUTIVE SUMMARY

The purpose of this contract was to develop superior materials for optical limiters for sensor protection against high power lasers. To be effective such limiters must respond in ~ 1 μs to laser power of 1W/cm^2 . When this program started, $LiNbO_3$, $BaTiO_3$ and tungsten bronze (T.B.) materials were the best candidates; however, each material was inadequate for practical applications. For example, $LiNbO_3$ was too slow, $BaTiO_3$ was not growable in large sizes and tungsten bronze $Sr_{1-x}Ba_xNb_2O_6$ (SBN) was only emerging. As a result of this program, we have achieved a response in the range of 10 μs at 1 W/cm^2 for 0.02 wt% Ce-doped $Sr_{0.6}Ba_{0.4}Nb_2O_6$ (SBN:60) crystals with the aid of an external electric field and focusing of the laser beam. Prototype optical limiters are being designed and tested using this crystal at the University of Arkansas.

Among the tungsten bronzes, we selected high optical figure-of-merit (n^3r_{ij}/ε) SBN:60 and $Ba_{1.5}Sr_{0.5}K_{0.25}Na_{0.75}Nb_{15}$ (BSKNN-2), and studied the role of various dopants .We found that the photorefractive speed and coupling were promising for Ce- and Cr-doped crystals. For example, in SBN:60 doped with 0.02 wt% Ce^{3+}, the response was 40-60 ms while the coupling was > 20 cm^{-1} at 1 W/cm^2 without any external parameters. When this particular crystal was subjected to an external electric field of 1-3 kV/cm and the laser beam was focused to an intensity of 10^3-10^4 W/cm^2, the photorefractive response improved to the range of 10 μs in the wavelength range of 400-720 nm. To improve this response to ~ 1 μs, we adopted double doping schemes, and in particular Cr^{3+} + Mo^{4+} (0.02 wt%) doped SBN:60 crystals showed promising results. We believe that this crystal should produce the desired 1 μs response under the same external conditions as were used for Ce-doped SBN:60.

Through this program, we identified and grew materials within the T. B. family that meet the requirements for sensor protection, namely, singly and doubly doped SBN:60 and BSKNN-2. Their performance in prototype optical limiters (built at the Unversity of Arkansas) confirms the suitability of this T. B. technology for sensor protection. Figure 1.1 summarizes the progress made in this program over the last six years.
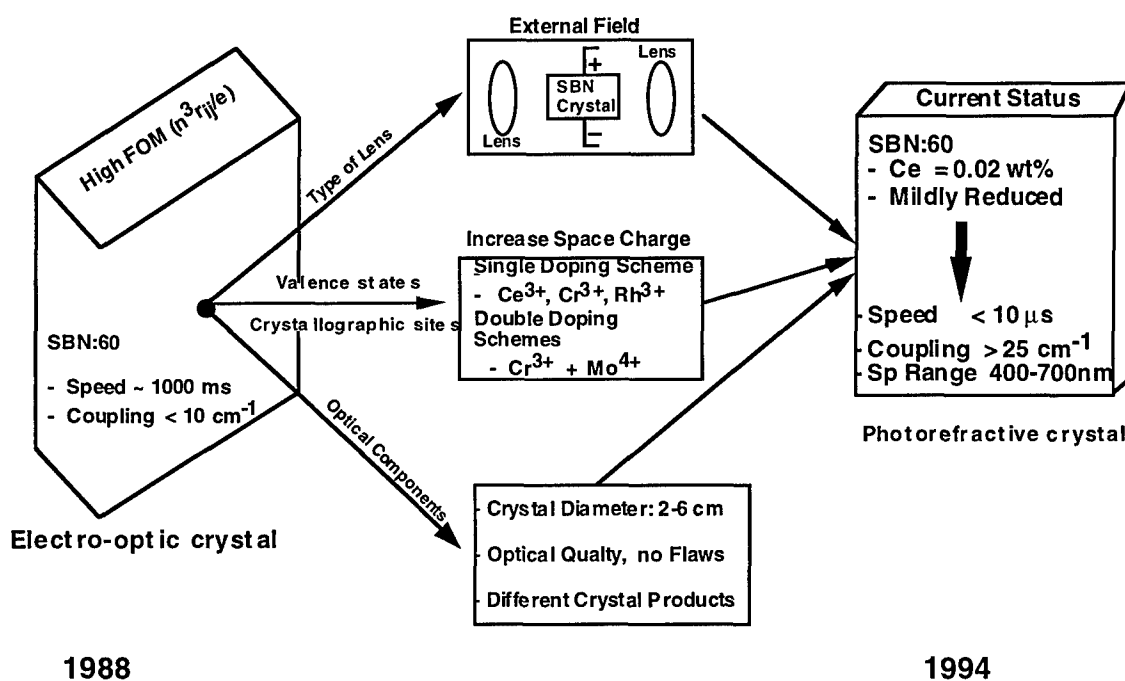
SC-0633-E

Figure 1.1 -- Targeted program goals: Photorefractive speed and coupling.

2.0 PROGRESS

A five year program of materials development for sensor protection was conducted at the Rockwell Science Center in collaboration with several groups. The tungsten bronze materials were selected for these studies because of the high optical figures-of-merit available in this family and the possibility of growing large size (> 5 cm diameter) single crystals of optical quality. Measurements have shown that some of these bronzes exhibit exceptional speed of response and high coupling of the levels required in sensor protection systems.

The overall program was designed by the Night Vision and Electronic Sensors Directorate (NVESD) at Fort Belvoir as a collaboration among Rockwell - the University of Arkansas - NVESD to develop optical limiters for sensor protection systems. The University of Arkansas provided photorefractive characterization and prototype limiter designs. At the NVESD, the role of dopants was studied to optimize limiter performance using the tungsten bronze SBN:60 and BSKNN-2 crystals. Using these inputs, Rockwell developed suitable high figure-of-merit tungsten bronze hosts, appropriate doping schemes and growth techniques. This effort produced a large amount of information regarding limiter technology, including the identification of practical sensor protection alternatives. This report describes the Rockwell materials development effort and the results of optical and photorefractive measurements on these materials. Section 3.1 presents the background on tungsten bronze materials and Section 3.2 on crystal growth and associated problems.

2.1 Introduction to Tungsten Bronze Materials

Tungsten bronze ferroelectrics are very useful for electro-optic, piezoelectric, pyroelectric and millimeter wave applications, and more recently for photorefractive applications.[1-21] Considerable work has been published on the development of this family of materials; however, these materials did not find widespread initial application due to the lack of crystals of adequate size and quality. At the Rockwell International Science Center, we have systematically studied the major growth problems, crystal habits and classification of these materials based on their ferroelectric and optical properties.[22-37] In this report, we present our major findings on the growth of these crystals, their classification and their potential for sensor protection applications.

2.2 Background: Fundamental Properties

A number of ferroelectrics of present or potential commercial importance have the tungsten bronze structure. This structure is typified by oxygen octahedra linked at the corners in a complex way to yield three types of openings, two of which normally contain the A_1 and A_2 cations as shown in Figure 3.1. The B cations, typically niobium (Nb^{5+}) or tantalum (Ta^{5+}), are inside the oxygen octahedra. The tungsten bronze compositions are characterized by the chemical formulae $(A_1)_4(A_2)_2C_4B_{10}O_{30}$ or $(A_1)_4(A_2)_2B_{10}O_{30}$, in which the A_1 cations are in the 15-fold coordinated site, the A_2 cations are in the 12-fold coordinated site, the C cations are in the 9-fold coordinated site and the B cations are in two different 6-fold coordinated sites. Detailed descriptions of this structure have been given in several articles.[38-40] Only two compositions, $K_3Li_2Nb_5O_{15}$ and $K_3Li_2Ta_5O_{15}$, can be represented by the first chemical formula where all five crystallographic sites are filled.[41-42] For this reason, these compositions are known as "stuffed" bronzes. All other tungsten bronzes are called either "filled" or "unfilled" bronzes with the 9-fold coordinated site vacant and the 15- and 12-fold coordinated sites either fully or partially occupied. For example, lead metaniobate and strontium barium niobate have unfilled unit cells containing $Pb_5Nb_{10}O_{30}$ and $(Sr,Ba)_5Nb_{10}O_{30}$ (usually simplified to $PbNb_2O_6$ and $(Sr,Ba)Nb_2O_6$) where the A sites are only 5/6 filled. Although the presumption is that the distribution among the 15- and 12-fold coordinated A sites is random, more likely in SBN, Ba^{2+} predominantly occupies the 15-fold coordinated site since Ba^{2+} (1.74 Å) is substantially larger than Sr^{2+} (1.54 Å).

Like the ferroelectric perovskite family, the bronze family embraces more than 150 compounds and solid solutions, including several morphotropic phase boundary systems.[43-44] Because of the structural complexity which accommodates a wide range of cationic substitutions, often the ferroelectric transition can be achieved in the desired temperature range with suitable ferroelectric and optical properties.

2.3 Crystal Growth and Associated Problems

Table 2.1 lists a number of tungsten bronze single crystals grown in our work and their ferroelectric and optical properties. The Czochralski pulling technique was used for these growths, with the crystals pulled from 5 x 5 cm platinum crucibles in an oxygen atmosphere to minimize the reduction of Nb^{5+} to Nb^{4+}. All of the crystals listed in Table 2.1 were grown along the [001] direction, except for the $K_3Li_2Nb_5O_{15}$ crystals where the best growth direction was found to be along [110]. Crystal cracking during cool-down through the paraelectric/ferroelectric phase

transition was initially a problem for most of these crystals, but this problem has now been minimized, particularly for SBN and BSKNN .

SC43117
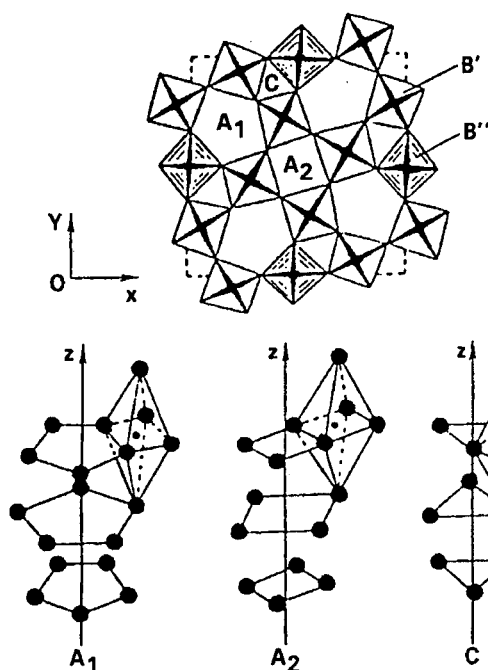
• CHEMICAL FORMULAE
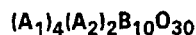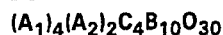
$(A_1)_4(A_2)_2C_4B_{10}O_{30}$

$(A_1)_4(A_2)_2B_{10}O_{30}$

A_1 = 15-FOLD COORDINATED SITE
A_2 = 12-FOLD COORDINATED SITE
C = 9-FOLD COORDINATED SITE
B = 6-FOLD COORDINATED SITE (TWO SITES)

• CRYSTAL STRUCTURE

4/mmm TO 4mm (TETRAGONAL-TETRAGONAL)
4mmm TO mm2 (TETRAGONAL-ORTHORHOMBIC)

• KNOWN SYSTEMS

150 COMPOUNDS OR
SOLID SOLUTIONS BETWEEN END MEMBERS
SEVERAL MORPHOTROPIC PHASE BOUNDARY
SYSTEMS

Figure 2.1 -- Projection of the tungsten bronze structure parallel to [001].

Based on ferroelectric and optical studies of both tetragonal and orthorhombic bronze crystals, we have classified this family into four different groups shown in Figure 3.2. These classifications are:

1. Crystals exhibiting strong transverse effects with 4mm symmetry (e.g. SBN) : <001> polar axis.

2. Crystals exhibiting strong longitudinal effects with 4mm symmetry (e.g. BSKNN): <001> polar axis.

3. Crystals exhibiting strong transverse and longitudinal effects with mm2 symmetry (e.g. $Sr_{2-x}Ca_xNaNb_5O_{15}$): <001> polar axis.

4. Crystals exhibiting strong longitudinal effects with mm2 symmetry (e.g. $Pb_{1-x}Ba_xNb_2O_{15}$): <100> or <010> polar axis.

TABLE 2.1

Ferroelectric Tungsten Bronze Crystals Grown at Rockwell

Composition	Growth Temp (°C)	Pull Rate (mm/hr)	Dielectric Constant	Diameter (cm)	T_c (°C)	r_{ij} $\times 10^{-12}$ m/V
$Sr_{0.75}Ba_{0.25}N_2O_6$ (SBN:75)	1480	4-5	$\varepsilon_{33} = 3000$	4.0	56	$r_{33} = 1400$
$Sr_{0.6}Ba_{0.4}Nb_2O_6$ (SBN:60)*	1485	5-7	$\varepsilon_{33} = 1000$	5.0	78	$r_{33} = 420$
$Ba_{1.5}Sr_{0.5}K_{0.5}Na_{0.5}Nb_5O_{15}$*	1470	3-4	$\varepsilon_{11} = 1000$	1.5	209	$r_{51} = 230$
$Ba_{0.5}Sr_{1.5}K_{0.75}Na_{0.25}Nb_5O_{15}$*	1475	4-5	$\varepsilon_{11} = 1100$	2.0	172	$r_{51} = 400$
$Sr_{1.9}Ca_{0.1}NaNb_5O_{15}$* (SCNN)	1500	2-3	$\varepsilon_{33} = 1740$	1.0	270	$r_{33} = 720$
			$\varepsilon_{11} = 1700$			$r_{51} = 230$
$Pb_{0.6}Ba_{0.4}Nb_2O_6$ (PBN:60)	1350	1-2	$\varepsilon_{11} = 1900$	1.5	320	$r_{51} > 2000$

* Grown in the present work.

Over 25 different bronze crystal compositions have been grown (with some of them listed in Table 2.1) and in some cases they have been modified to meet the requirements for electro-optic, photorefractive and piezoelectric applications All of these crystals have been grown by the Czochralski technique.[23-35] Although we have grown and characterized many tungsten bronze crystals for the last fifteen years, we have concentrated on a few crystals as summarized in Figure 2.3.

Ba$_2$-xSr$_x$K$_1$-yNa$_y$Nb$_5$O$_{15}$ Type (4mm)
• Large longitudinal effects
  r$_{51}$, d$_{15}$, ε$_{11}$
• Square or octahedron shape crystals
• T$_c$ > 150°C
• Moderate polarization (P$_3$)

Addition of K$^+$ and Na$^+$

Sr$_1$-xBa$_x$Nb$_2$O$_6$ Type (4mm)
• Large transverse effects
  r$_{33}$, ε$_{33}$, d$_{33}$
• Cylindrical shape (24-facets)
• T$_c$ < 150°C
• Moderate polarization (P$_3$)

T.B. Family
(A$_1$)$_4$(A$_2$)$_2$C$_4$B$_{10}$O$_{30}$
or
(A$_1$)$_4$(A$_2$)$_2$B$_{10}$O$_{30}$

mm2 : 4mm ON K$^+$; Na$^+$ Ratio

Addition of Na$^+$

Sr$_2$-xCa$_x$NaNb$_5$O$_{15}$ Type (mm2)
• Large longitudinal and transverse effects
  r$_{15}$, d$_{15}$ and r$_{33}$, d$_{33}$
• Cylindrical crystals
• T$_c$~200-300°C
• Large polarization (P$_3$)

PbNb$_2$O$_6$-Type (mm2)
• Large longitudinal effects
  r$_{51}$, d$_{15}$ ε$_{11}$
• T$_c$~350°C
• Large polarization (P$_2$)
  (Pb$_2$KNb$_5$O$_{15}$ Exception)

(mm2) and (mm2)
Symmetry of end member

Mixing of | mm2 + mm2
or
mm2 + 4mm

Morphotropic phase boundary materials

r$_{33}$, d$_{33}$ ε$_{33}$, P$_2$ (mm2 Form)
r$_{51}$, d$_{15}$, e$_{11}$, P$_3$ (4mm form)
• T$_c$ 150 to 400°C
• Exceptionally large polarization (P$_3$ or P$_2$)

Figure 2.2 -- Classification of tungsten bronze crystals.

1988   1990   1993   1993-1994

Large r$_{33}$
SBN
BSTN

SBN
BSKNN

Large r$_{51}$
BSKNN
PBN, KLN

SCNN
BSKNN
SBN

- Excellent FOM
- Large size and Excellent
  Optical Quality

Large r$_{33}$ & r$_{51}$
SCNN
KBN

Large n^{3}r$_{ij}$/ε

Time ~ 10-30 ms

Coupling > 35 cm^{-1}

Storage:
As Grown > 1 Day
Oxidized 1-8 Days

Current Status
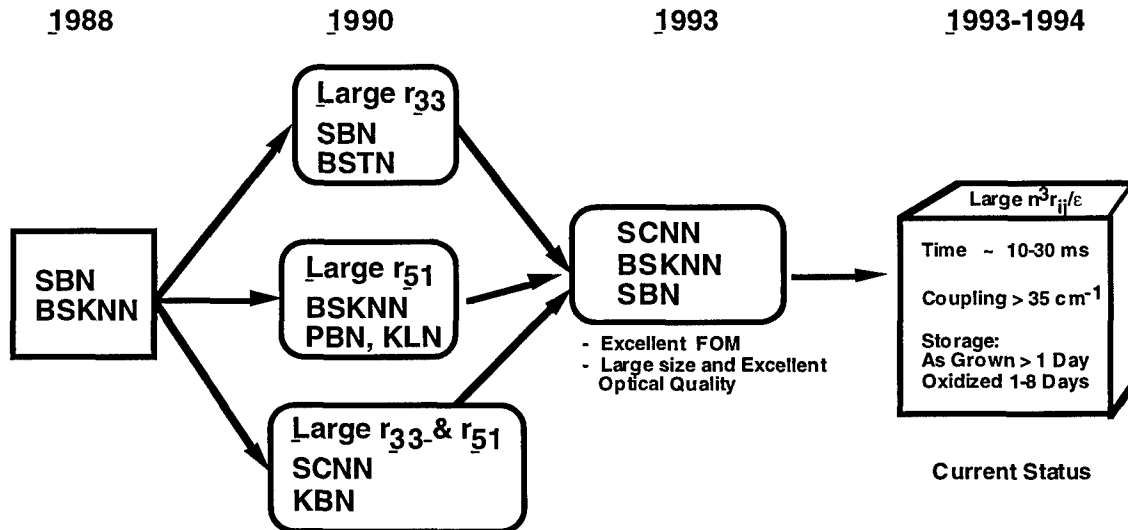
Figure 2.3 -- Chronological development of tungsten bronze crystals.

Tungsten bronze crystals are relatively easy to grow compared to most ferroelectric crystals based on perovskite, layered structure Bi$_4$Ti$_3$O$_{12}$, and lead germanates, phosphate and vanadates. This is due in part because the bronzes have simple phase transitions and are usually free of 90° twins which occur in perovskite single crystals. Among the growth problems associated with these crystals (Figure 3.4), we have found the following to be major contributors toward poor

7

crystal quality:

1. Multicomponent solid solution systems make it difficult to control crystal homogeneity.

2. Exchange among crystallographic sites, specifically of the 15- and 12-fold coordinated ions such as Ba^{2+}, Sr^{2+}, K^+, La^{3+}, causing severe striation problems.

3. High temperature growths (up to 1500 °C) cause volatilization and oxidation-reduction (Nb^{5+} to Nb^{4+}) problems.

4. Cracking of crystals when thermally cycling through phase transitions. This is often aggravated by crystal imperfections.

SC38172

DEFECTS
- CORING
- STRIATION AND OTHER DEFECTS
- INCLUSIONS
- STRAIN

CRACKING OF CRYSTALS
- FERRO-FERRO
  4 mm → mm2
- PARA-FERRO
  4/mmm → 4mm
- THERMAL CRACKING

MULTICOMPONENT-SOLID SOLUTIONS
- TRUE CONGRUENT MELTING COMPOSITION
- COMPOSITIONAL FLUCTUATIONS

TEMP INSTABILITY

TRANSITIONS

STRUCTURAL INFLUENCE

COMPOSITION

CONTAMINATION

PROBLEMS ASSOCIATED WITH GROWTH OF TUNGSTEN BRONZE CRYSTALS

SITE PREFERENCES
- FLUCTUATION OF Ba^{2+}, Sr^{2+}, Na^+ ON 15- AND 12-FOLD CO-ORDINATED SITES

OTHERS

HIGH TEMP GROWTH
- CONTAINER PROBLEM IrO_2-CONTAMINATION
- OXIDATION-REDUCTION $Nb^{5+} \rightleftharpoons Nb^{4+}$
- VOLATILIZATION Pb^{2+}, K^+, Na^+

MATERIAL RELATED
- VISCOSITY
- SUPER COOLING
- VAPOR PRESSURE
- PHASE TRANSITION
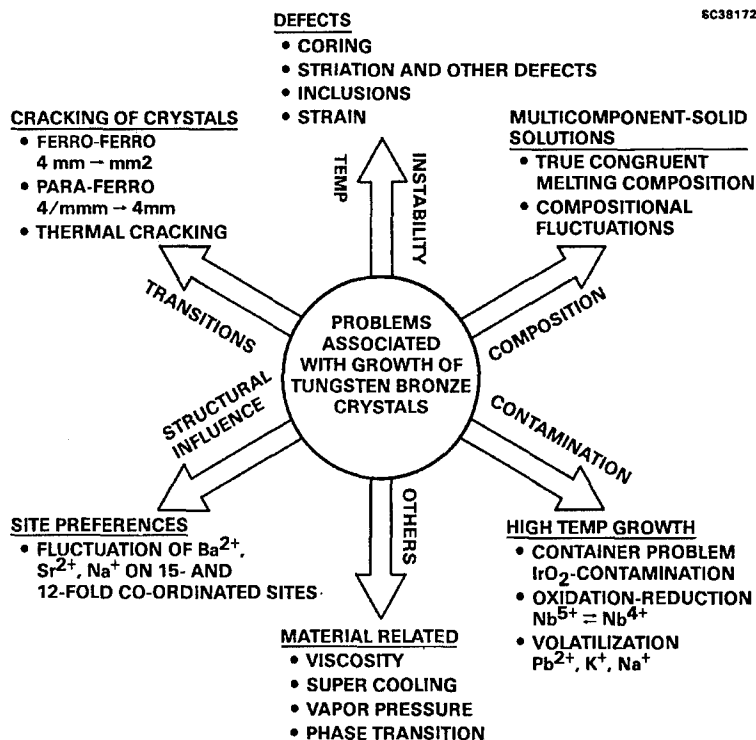
Figure 2.4 -- Problems associated with the growth of tungsten bronze crystals.

Nevertheless, several bronze compositions have been grown as large size, defect-free crystals, including SBN (> 4 cm diameter) and $Ba_{2-x}Sr_xK_{1-y}N_yNb_5O_{15}$ (> 1.5 cm diameter) which have excellent optical quality.

Currently, we grow SBN:60 crystals as large as 6 cm diameter and $Ba_{0.5}Sr_{1.5}K_{0.75}Na_{0.25}Nb_5O_{15}$ (BSKNN-2) crystals up to 4 cm diameter. Figures 2.5 and 2.6

8

show typical Ce-doped SBN:60 and BSKNN-2 crystals grown along the [001] direction. Although the Czochralski technique is now well developed for large size crystals, we have also grown smaller crystals, typically in the range of 1.5 to 2 cm diameter, to quickly assess the photorefractive properties of different dopants. Table 2.2 summarizes the dopants used in these crystals. Information on these photorefractive dopants and their role in SBN and BSKNN are discussed in Section 3.0.
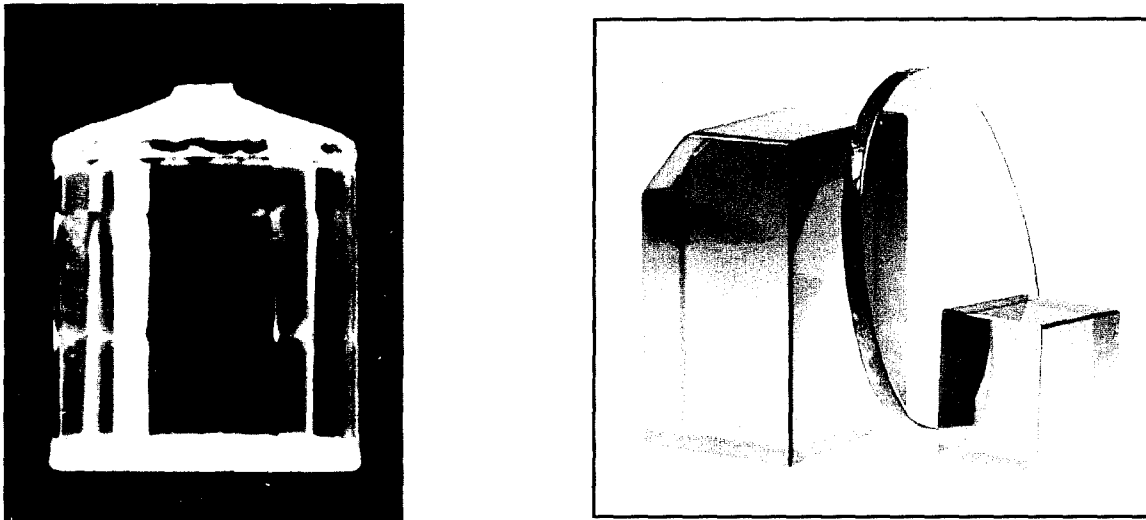
Figure 2.5 -- Tungsten bronze SBN single crystal boule and Products
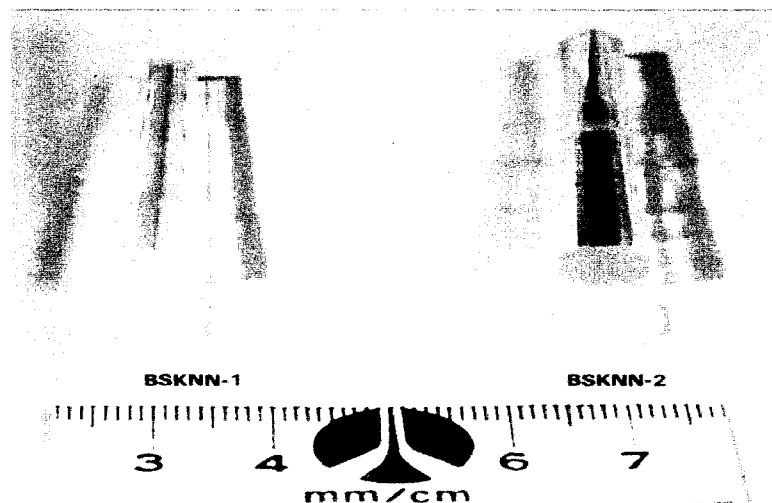
Figure 2.6 -- Tungsten bronze BSKNN single crystal grown along [001].

Table 2.2
Photorefractive Dopants in Tungsten Bronze Crystals

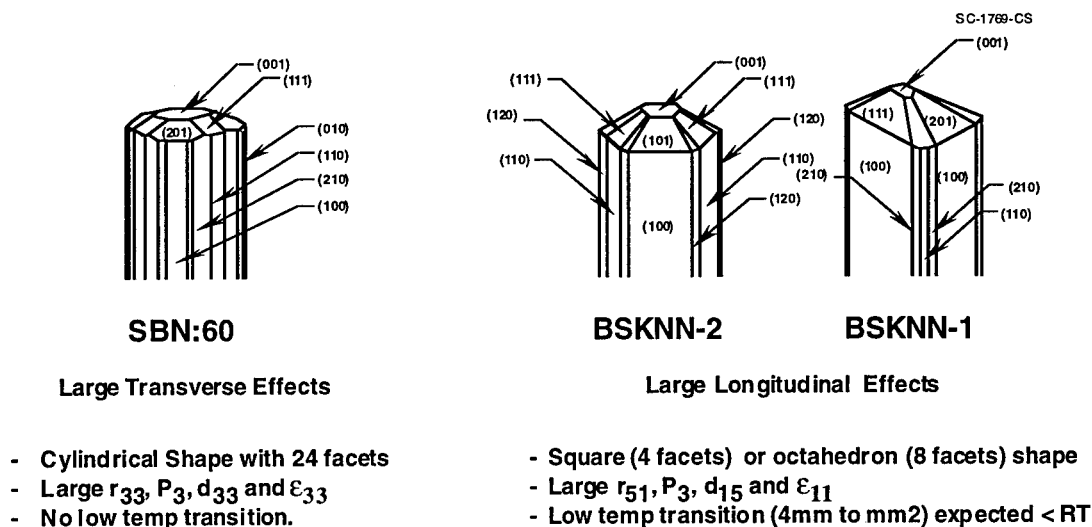| Dopant	Color	Dopant Levels	Crystal Quality
Ce^{3+}/Ce^{4+}	Pink	0.005 to 0.10%	Excellent
Fe^{2+}/Fe^{3+}	Pale yellow	0.005 to 0.02%	Striations at high levels
Rh^{3+}/Rh^{4+}	Yellow	0.010 to 0.12%	Excellent
Cr^{3+}/Cr^{4+}	Greenish	0.005 to 0.080%	Striations at high levels
$Cr^{3+} + Mo^{4+}$	Greenish	0.010 to 0.040%	Excellent
$Cr^{3+} + Fe^{3+}$	Greenish	0.010 to 0.040%	Excellent

We were the first group to grow SCNN solid solution crystals and establish their optical and ferroelectric properties. It is interesting to note that SCNN crystals exhibit both transverse (r_{33}) and longitudinal (r_{51}) electro-optic coefficients large and nearly equal. This is a unique feature within this family of crystals, but the growth of these orthorhombic crystals was found to be extremely difficult, with the growth technique being successful only for small size crystals, typically in the range of 1 cm diameter. Since these SCNN crystals are technologically important for many applications, we are exploring other growth techniques to grow these crystals in larger sizes (> 3 cm diameter). If SCNN crystals become available in large sizes, they present a major breakthrough for optical applications, including laser hardening, data storage and guided wave optics.

SBN crystals have a distinct cylindrical growth habit with 24 well-defined facets, each facet corresponding to a definite crystallographic orientation. For this reason, precise orientation and cutting of these crystals is a greatly simplified task. BSKNN crystals have distinctly different growth habits, growing either with 4 or 8 well-defined facets (Figure 3.7). Based on our observation of five different BSKNN compositions, those with larger unit cells grow with 4 facets, while compositions having smaller unit cells grow with 8 facets. The compositional region in which switching from 4 to 8 facets takes place is not yet established. In spite of these differences, both types of crystals exhibit strong longitudinal ferroelectric and electro-optic effects.

SC-1769-CS

SBN:60	BSKNN-2	BSKNN-1
Large Transverse Effects	**Large Longitudinal Effects**	

- Cylindrical Shape with 24 facets
- Large r_{33}, P_3, d_{33} and ε_{33}
- No low temp transition.

- Square (4 facets) or octahedron (8 facets) shape
- Large r_{51}, P_3, d_{15} and ε_{11}
- Low temp transition (4mm to mm2) expected < RT

Figure 2.7 -- Growth habits for tetragonal tungsten bronze crystals.

All BSKNN single crystals have ferroelectric and optical characteristics similar to $BaTiO_3$; however, these tungsten bronze crystals are free of 90° twins; hence the growth of large size (> 4 cm diameter) BSKNN crystals is possible. Because of these attractive features, BSKNN crystals present major advantages for large scale applications and subsequent commercialization.

2.4   Quality of Tungsten Bronze Crystals

The optical quality and uniformity of doped SBN:60 and and BSKNN-2 single crystal boules grown in our work were evaluated by optical and ferroelectric measurement techniques. Based on these measurements, we found that the photorefractive speed and coupling are sensitive to both the crystal quality and uniformity; however, crystal samples from the same boule show identical properties.

A typical non-uniformity is the presence of striations which reflect temperature variations at the growth interface between the solid and liquid. Figure 2.8 shows micrographs of high striated (a), weakly striated (b) and optical quality (c) SBN:60 crystals grown by the Czochralski technique.
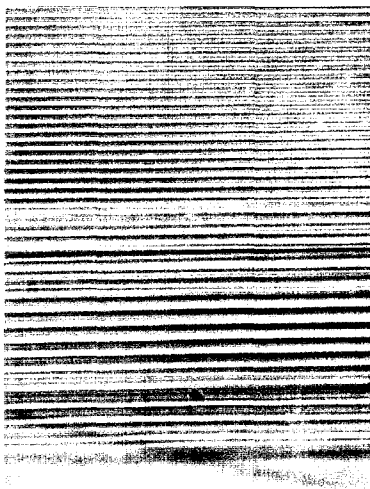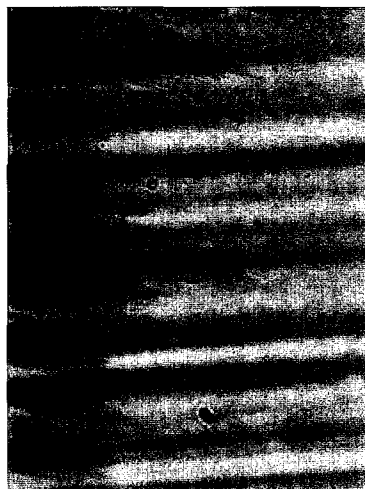
| Highly Striated | Weakly Striated | No Striations |

Figure 2.8 -- Striation patterns observed in SBN:60 single crystals.

A number of years ago, we systematically studied the growth conditions that give rise to striations, and found that we could suppress striations by adequate temperature control. Our work in the current project was restricted to maintaining high optical quality and, therefore, uniform photorefractive properties were achieved throughout each boule.

Another factor affecting photorefractive properties is the oxidation state of the dopants as well as niobium. We found that if a high oxygen pressure is not properly maintained during cooldown, the donor:acceptor ratio fluctuates, and this reflects on the photorefractive properties. Also, non-uniformity within a given crystal will occur because of oxygen vacancy diffusion. For this reason, cut crystal samples were annealed at ~600-650 °C to insure uniform oxidation. Table 2.3 summarizes our results on oxidation/reduction of Ce-doped SBN:60 crystals. We also investigated the partial reduction of other dopants, e.g. Cr, Rh and Fe, with similar results. This work shows that mildly reducing conditions can be favorable to achieve fast photorefractive response in these materials.

Table 2.3

Effects of Oxidation/Reduction on Ce-doped SBN:60

Annealing Conditions	Speed of Response (ms)	Dark Conductivity (Ω^{-1} - cm^{-1})
450 - 600°C		
1. Oxygen Atmosphere	Fast	~ 10^{-15}
2. Reducing Conditions	Faster	> 10^{-14}
> 600°C		
1. Oxygen Atmosphere	Fast	~ 10^{-15}
2. Reducing Conditions[*]	-----	> 10^{-13}

[*] Crystals are opaque, and do not exhibit photorefractive effects.

Our experience with photorefractive dopants has shown that they do not have a major impact on the ferroelectric properties of the crystal host at moderate doping levels, save for slight alterations of the ferroelectric phase transition temperature and slight (10 - 15%) increases in the dielectric constant at room temperature. In instances where the phase transition temperature has changed with doping, it invariably decreases from its undoped value for a given crystal composition. This effect can be understood by recognizing that the onset of spontaneous polarization in the ferroelectric phase requires the long-range cooperative coupling of individual dipoles, since the crystal free energy minimum per unit cell at $P = P_s$ is much less than kT at room temperature.[45] The introduction of dopant impurities necessarily perturbs the long-range coupling, so that the onset of an ordered spontaneously polarized state occurs at a lower temperature. This effect is small at typical doping levels, however, with changes being typically only a few degrees Centigrade. While this has little effect on the dielectric constant at room temperature for high-T_c crystals such as BSKNN, it can increase the dielectric constant (and hence, the electro-optic coefficient) more significantly in crystals such as SBN:60 and SBN:75 which have T_c well below 100 °C. This occurs because of the strong temperature dependence of the dielectric constant as $T \rightarrow T_c$, since the dielectric constant in these bronze crystals closely follows the Curie-Weiss law,

$$\varepsilon \approx C/(\Theta - T) \qquad (2.1)$$

where $\Theta = T_c$ due to the second-order nature of the phase transition.

The room-temperature spontaneous polarization is not significantly affected by crystal doping at these concentrations; this is true even for the low-T_c bronze crystals since P_s has only a weak temperature dependence at temperatures more than 15 - 20 °C below T_c.[45] The one exception to this is in crystals which have been moderately to strongly reduced, typically by annealing in a low oxygen partial pressure atmosphere above 500 °C. In these instances, the bulk polarization can be as much as 20-25% lower than in fully oxidized crystals, with this reflecting upon the piezoelectric properties (and the electro-optic constants) as well. Whether this is due to an overall reduction of the polar displacement, or to a pinning of local microdomains by vacancy defects, is not known at present, although recent work on $BaTiO_3$ [46] indicates that domain-pinning is the primary contributor.

It is worthwhile to note that aside from measurements of the dielectric and spontaneous polarization properties of these crystals, a simple measurement of the d_{33} piezoelectric coefficient has proven to be a highly effective, simple test of the quality of a given crystal and the completeness of poling to a single domain state. This test necessarily reflects upon the linear electro-optic coefficients r_{ij}, since both d_{33} and r_{ij} depend linearly upon the static dielectric constant, the spontaneous polarization and the respective electrostriction/electro-optic quadratic constants.

Based on our long-standing experience with tungsten bronze crystals, the d_{33} constant is known to fall within a given range of values depending on the particular crystal composition being examined; deviations below this range is an indication of potential problems with a given crystal growth. Hence this test, as well as other electrical measurements in particular instances, has been routinely applied to the crystals supplied for optical evaluation in this program to insure consistent ferroelectric behavior.

3.0 PHOTOREFRACTIVE PROPERTIES
OF TUNGSTEN BRONZE CRYSTALS

Oxide ferroelectrics exhibit the largest electro-optic effects of any known materials; however, they have wide optical bandgaps, and thus do not strongly absorb visible light. This deficiency can be overcome through the use of suitable dopants that absorb light in the desired spectral range (0.40 to 0.78 μm). By this means, tungsten bronze SBN:60 and BSKNN-2 have been endowed with excellent photorefractive properties, including speed and coupling. In particular, a speed of response of 10 μs at 1 W/cm^2 illumination has been demonstrated in SBN:60 due to the contribution of several factors. Starting from undoped SBN:60 with a speed of ~1 sec, we doped these crystals with Ce^{3+}, Cr^{3+}, Rh^{3+}, etc., to achieve response times in the range of 1-100 ms. Applying an electric field of 5-10 kV/cm to these doped crystals shortened the response time by an order of magnitude. Finally, focusing a 1 W/cm^2 laser beam improved the response time another 2 to 3 orders of magnitude, with times in the range of 10 μs. A discussion of these enhancements and the role of individual dopants are described in this section.

3.1 The Photorefractive Effect and the Selection of Dopants

The issues connected with the photorefractive effect include the sensitivity of the given material to illumination and the speed with which the index can be made to change. In spontaneously polarized ferroelectrics, light-induced free carriers are displaced along the polar axis of the crystal and are trapped at normally empty trapping sites (e.g., impurities, dopants or defect levels). The resulting space charge field gives rise to a change in the material refractive index via the linear electro-optic effect through r_{ij}.

Since the electro-optic coefficient in a given crystal is essentially independent of minor dopant substitutions, save for possible changes in r_{ij} due to small alterations of the crystal phase transition temperature, the improvement in the photorefractive sensitivity and speed for a given crystal composition has to come from the magnitude and speed of the buildup of the space charge field, with the latter being controlled by the effective density of trapped space charge and by the rate of generation of photoionized charge carriers.

It is now well-established that doping ferroelectric crystals with specific impurities which are readily photoionizable by incident radiation greatly increases the susceptibility of these crystals to index changes. That such would be the case is not surprising, since many dopants provide strong optical absorption, especially in the visible spectrum and the near-IR in some cases, and can act as

a reservior of photoionizable electrons (or, holes) as well as energetically deep traps in their partially filled state. For example, Megumi et al.[47] were among the first investigators to show improved photorefractive sensitivity in SBN:60 crystals using Ce as a dopant. The Ce ion photoionizes by means of the reaction

$$Ce^{3+} + h\nu \rightarrow Ce^{4+} + e^-$$
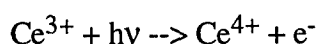
with Ce^{3+} being a filled neutral donor and Ce^{4+} its positively charged empty state. The ratio of Ce^{4+} to Ce^{3+} in a given region of a crystal is necessarily determined by the position of the quasi-Fermi level in the bandgap, and this in turn is controlled by the illumination intensity, the degree of compensation by deep-lying ionized acceptor levels, N_a^-, and the concentration of other, energetically shallow ionized donors (e.g., oxygen vacancies). The process is necessarily a dynamic one since it depends on the photon flux, the free-carrier mobility and diffusion rate, and the thermal emission rate of the trapped carriers into the conduction (or valence) band. The latter particularly impacts the selection of the proper dopants for a given crystal, since traps with energies less than ~0.8 eV from either the conduction or valence band will rapidly re-emit trapped carriers at room temperature, and thus substantially reduce the photorefractive sensitivity. The latter is amply demonstrated, for example, by thermally stimulated conductivity measurements in oxide crystals such as $SrTiO_3$.[48]

As pointed out by Yeh[49], the theoretical minimum response time ,τ_{min}, for a photorefractive crystal is proportional to the two-beam coupling constant, Γ, and inversely proportional to the illumination intensity, the absorption coefficient at the specific wavelength of interest, and the electro-optic coefficient, r_{ij}. Thus, with all other factors being equal, crystals with higher photorefractive gain (Γ) tend to have longer response times due to the fact that higher coupling requires the formation of higher space charge concentrations. This fact is reflected in Table 3.1 which shows that the relative photorefractive gain and response speed (i.e., τ^{-1}) among the various dopants investigated in this program are generally inversely proportional to each other.

The measured response time, which is typically longer than the theoretical minimum, can be reduced by simply increasing the illumination intensity. In cases where the incident intensity is fixed, this can be accomplished by focusing using standard optics.[50] Furthermore, applying an external electric field in the same direction as the original poling field can also reduce the response time and also substantially increase the two-beam coupling coefficient.[51-54] The application of an external electric field assists the movement of electrons in the conduction band to dark regions where they can be trapped, resulting in a larger space charge field and thus a higher index

16

modulation. Increases in coupling by upward of a factor of 3 can be realized at moderate field strengths on the order of 10 kV/cm. As pointed out by Sayano et al.[51], some of the zero-field limitiations on coupling with increased doping concentrations are substantially relaxed with externally applied fields, primarily because of an increase in the maximum permissible space charge field.

Table 3.1

Comparison of Photorefractive Speed and Coupling at 1W/cm^2

Dopant	Site Preference	Speed (ms)	Coupling (cm^{-1})
Ce^{3+}/Ce^{4+}			
Ce = 0.01 to 0.02%	12- fold	~ 20-60	~ 15
0.03 to 0.07%	12 - fold	100	> 45
Rh^{3+}/Rh^{4+}			
Rh = 0.01 to 0.03%	6 -fold	~ 30 -50	15 - 25
0.04 to 0.10%	6 - fold	100	40 - 65
Fe^{2+}/Fe^{3+}			
Fe = 0.01 to 0.03%	6 - fold	~ 20 -60	10 - 20
0.04 to 0.07%*	6 - fold	> 100	> 25
Cr^{3+}/Cr^{5+}			
Cr = 0.01 to 0.03%	6 -fold	10 - 20	5 - 6
0.04 to 0.07%*	6-fold	~ 20	6- 7

* Weak striations observed for high concentration Cr- and Fe-doped crystals.

3.2   Optical Properties of Doped Tungsten Bronze Crystals

In the bronze crystals studied here, the combination of inherently high electro-optic coefficients and high two-beam coupling with optimized dopants has resulted in photorefractive crystals with performance exceeding that in most other materials. The use of focused illumination and the application of external electric fields further enhances these properties, with measured coupling constants greater than 20 cm^{-1} and response times on the order of ten microseconds for SBN:60

doped with 0.02 wt% Ce^{3+}/Ce^{4+}.

The various dopants considered in this program are listed in Table 3.2 according to their expected valence states and site preferences in the tungsten bronze crystal lattice. These site preferences are based primarily on the ionic size of the individual dopant. The spectral response for these dopants is seen to lie in the range of 0.4 to 0.8 µm. However, Cr^{3+} and Co^{3+}-doped crystals have extended response out to 0.9 µm. Figure 3.1 summarizes the spectral response for these dopants in tungsten bronze crystals.

Table 3.2
Dopant Site Preferences in the Tungsten Bronze Structure

| Dopants | Valence States | Crystallographic Site | | | | Sp Response |
		15-	12-	9-	6-	(µm)
Cerium	Ce^{3+}, Ce^{4+}	Ce^{3+}	Ce^{3+}	Ce^{4+}	---	0.4 to 0.70
Neodymium	Nd^{3+}	Nd^{3+}	Nd^{3+}	---	---	0.4 to 0.70
Rhodium	Rh^{3+}, Rh^{4+}	---	---	---	Rh^{3+},Rh^{4+}	0.4 to 0.78
Iron	Fe^{2+},Fe^{3+}, Fe^{4+}	---	---	---	Fe^{2+},Fe^{3+}	0.4 to 0.78
Manganese	Mn^{2+},Mn^{3+}, Mn^{4+}	---	---	---	Mn^{2+},Mn^{3+}	0.4 to 0.70
Chromium	Cr^{3+},Cr^{4+},Cr^{5+}	---	---	---	Cr^{3+},Cr^{5+}	0.4 to 0.90
Cobalt	Co^{2+},Co^{3+}, Co^{4+}	---	---	---	Co^{2+},Co^{3+}	0.4 to 0.80
Molybdenum	Mo^{4+}, Mo^{6+}	---	---	---	Mo^{4+},Mo^{6+}	0.4 to 0.70

Types of Dopants   Site Preference   Spectral Response
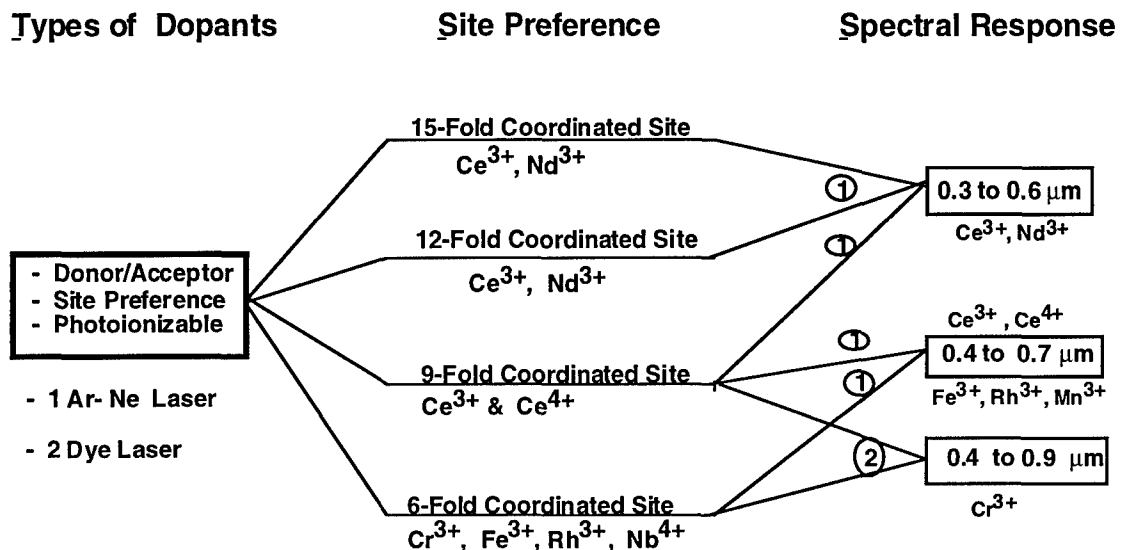
Figure 3.1 -- The effect of dopant site preference on spectral response. The circled numbers on the right refer to (1) Ar - Ne lasers, and (2) dye lasers.

3.3   Energy Levels of Dopants in the Tungsten Bronze Lattice

Undoped tungsten bronze crystals have n-type conductivity in all cases, as determined by oxidation/reduction and thermal-electric measurements. The dc conductivity above 100 °C may be described by the Arrhenius relation

$$\sigma = \sigma_0 \exp(-E_a/kT) \qquad (3.1)$$

where E_a is the thermal activation energy which describes the position of the equilibrium Fermi level. The σ_0 term does have some temperature dependence due to the $T^{3/2}$ temperature variation of the conduction band density of states and the variation of the electron mobility. The electron mobility is known in perovskite $SrTiO_3$ to decrease gradually with increasing temperature.[55] Since the tungsten bronzes may be thought of as distorted perovskite structures, it is not unreasonable to expect that the temperature dependence of the carrier mobility in the bronzes will be similar to that in $SrTiO_3$. Hence, we expect that the temperature dependence of the mobility will at least partially compensate for the density of states variation, so that for practical purposes one may reasonably take σ_0 to be independent of temperature. Because these crystals have a tetragonal structure, one expects the electron mobility to be anisotropic, and this is indeed the case with $\sigma_c/\sigma_a = 1.7 - 2.5$, with the spread in values due to slightly different temperature dependencies for the two mobilities.

In undoped crystals, $E_a = 1.56 - 1.62$ eV, essentially the middle of the ~3.2 eV band gap. We

take this to be the Nb^{4+}-V_{ox} donor complex; because of its position in the band gap, it is expected to act as both a donor and as a recombination level. This energy remains the same in both the partially filled (SBN) and filled (BSKNN) bronzes. Indeed, to date we have not observed any significant differences in the energy levels of defect sites or dopant ions in the two types of structures. The fact that the undoped crystals are strongly n-type, in spite of the mid-gap position of the Fermi level, indicates that the electron mobility is substantially greater than the hole mobility. This is consistent with results in perovskite crystals.[55] The equilibrium Fermi level can be raised closer to the conduction band by partial reduction above 450 °C. However, this can create space charge problems at the electrodes (depending on the degree of reduction), and the conductivity may not follow Eq. (3.1) in part because of the contribution of mobile oxygen vacancies to the total charge transport.

All of the primary dopants evaluated in this program (Ce, Rh, Fe, Cr and Mo) yield n-type conductivity in SBN and BSKNN crystals. Hence, these dopants contribute one or more donor levels to the crystal lattice, depending on the oxidation state of the crystal. The position of these donor levels in the band gap can be evaluated by measurement of the DC and/or AC crystal conductivity at elevated temperatures using Equation 3.1, since at moderate doping levels the dark
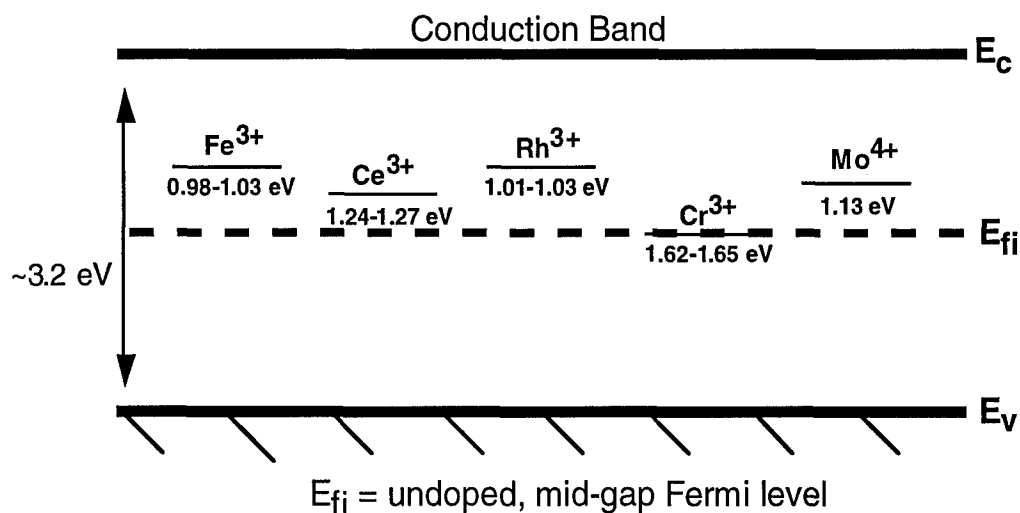
Figure 3.2 -- Donor energy levels for various dopants in the tungsten bronze band gap.

equilibrium Fermi level will be pinned within ~kT of the donor level energy, E_a. Such measurements have been conducted over a span of several years on numerous SBN and BSKNN crystals, and the position of the primary donor levels for these dopants in fully oxidized crystals are shown in Figure 3.2. A brief description of each dopant is given below.

Cerium (Ce^{3+}/Ce^{4+})

Cerium enters the crystal lattice as Ce^{3+}/Ce^{4+}. It is generally expected to reside at the 15- and 12-fold coordinated lattice sites. As a donor ion, it is filled in the 3+ state, and is an ionized electron trap in the empty 4+ state. Measurements on numerous crystals show a thermal activation energy for $Ce^{3+/4+}$ of 1.24 - 1.27 eV. Recent calculations using an interatomic potential model for Ce show good agreement with this activation energy for Ce at the 12-fold coordinated lattice site, substituting for the Sr^{2+} ion.[56] This is the highest lying cerium level in the band gap, with other possible levels tending to be closer to the valence band. Because it lies deep in the bandgap, Ce is expected to be an effective photorefractive dopant with a relatively long lifetime for trapped electrons. Optical measurements have shown Ce-doped SBN and BSKNN crystals to have very strong two-beam coupling, with a maximum value to date of 55 cm^{-1} in SBN crystals.

Iron (Fe^{3+}/Fe^{4+})

Measurements on fully oxidized Fe-doped SBN crystals show an activation energy of 0.98 - 1.03 eV for $Fe^{3+/4+}$. Partial reduction results in Fermi level pinning at 0.84 eV below the conduction band; although this may be another Fe donor, this level has been observed in other crystals not deliberately doped with Fe, and thus may be associated with crystal defects. Because of ionic size considerations, we expect Fe to prefer only the 6-fold coordinated Nb site in the bronze crystal lattice, as do other similarly sized ions such as $Ti^{3+/4+}$.

Chromium (Cr^{3+}/Cr^{4+})

Chromium is somewhat unique in that it may have up to three valence states: 3+, 4+ and 5+. Since Cr has strong preference for 6-fold coordinated sites, it is expected that Cr will enter only at the 6-fold coordinated Nb^{5+} site. Theoretical considerations of several Nb-substituting ions indicate that their ionization energies may reside above the conduction band edge, therefore making them optically and electrically inactive.[56] Nevertheless, ionic size considerations suggest that Cr would prefer this lattice site.

Chromium is highly unusual in that it does not significantly alter the Fermi level position compared to that for undoped bronze crystals, with $E_a = 1.62-1.65$ eV in fully oxidized crystals. Because it acts as a donor, this is undoubtedly $Cr^{3+/4+}$. Partial reduction at 500 °C moves the Fermi level to 1.02 eV below the conduction band; this may be the same Cr donor at an intersitial

21

lattice site, or a Cr^{3+}-V_{ox} donor complex. In the fully oxidized crystals, it is expected that Cr-doped bronzes should have the longest trapped-carrier lifetime of any of the studied dopants due to the mid-gap postion of the Cr^{4+} trap, assuming no significant hole recombination at this site.

Rhodium (Rh^{3+}/Rh^{4+})

Rhodium enters the crystal lattice as $Rh^{3+/4+}$; because of its small ionic size, it is expected to reside only at the Nb^{5+} sites. The measured thermal activation energy for $Rh^{3+/4+}$ is 1.01 - 1.03 eV below the conduction band, similar to the energy for Fe. Theoretical models for this ion have not been established to date. It is noteworthy that doping in the range of 0.07 to 0.1 wt% $Rh^{3+/4+}$ has achieved the highest two-beam coupling coefficient (65 cm^{-1}) in SBN:60 crystals among all of the dopants examined.

Molybdenum (Mo^{4+}/Mo^{6+})

Molybdenum is the newest dopant we have examined for potential use in photorefractive crystals. Because it has an ionic size similar to Nb^{5+}, it is expected that it will enter the crystal lattice only at the Nb^{5+} sites. Mo-doped crystals show this donor to have a 1.13 eV activation energy; presumably this is Mo^{4+}. Preliminary optical measurements indicate large photorefractive coupling in the range of 10 - 20 cm^{-1}.

3.4 Photorefractive Properties of SBN and BSKNN

Figure 3.3 shows SBN:60 single crystals doped with various dopants as indicated. Photorefractive measurements on doped SBN:60 and BSKNN-2 using the above dopants were made at various laboratories, including the University of Arkansas, NVESD, the Army Research Laboratory, Caltech, UCSD and Rockwell, and the results of their findings are comparable to one another. Dopant concentrations were kept in the range of 0.01 to 0.10 wt.%, with the photorefractive gain and speed saturating above this level. Among these dopants, Cr^{3+} in SBN:60 or BSKNN-2 produces fast response in the range of 1 to 10 ms, but coupling in these crystals is < 8 cm^{-1}. On the other hand, the coupling is in excess of 15 cm^{-1} in the other doped crystals listed in Table 3.2 and increases with higher doping concentrations. As shown in Figure 3.4, a two-beam coupling of 65 cm^{-1} was achieved with Rh^{3+}-doped SBN:60 (concentrations in the range of 0.07 to 0.1wt%), with photorefractive response times in the range of 10 to 60 ms.

**Figure 3.3 -- SBN:60 single crystals doped with various dopants.**

Ce^{3+} and Rh^{3+}-doped SBN:60 or BSKNN-2 crystals exhibit excellent optical quality for all concentrations and this allowed very precise photorefractive measurements. However, weak striations were observed for highly Cr^{3+} and Fe^{3+}-doped SBN:60 crystals (> 0.08 wt.%) in spite of excellent control over the crystal growth.
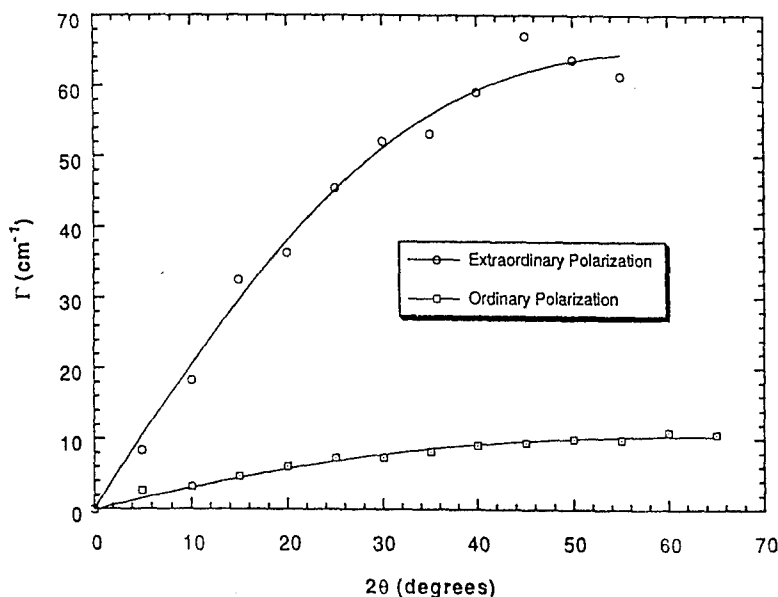

Figure 3.4 -- Coupling as a function of Rh^{3+} concentration.

Experiments were performed on these doped crystals using an external electric field as a means to speed up the response time. Figure 3.5 shows an order of magnitude improvement in the speed of response for Ce-doped SBN:60, and this improvement is typical for other doped tungsten

bronze crystals. Increased coupling is illustrated in Figure 3.6, where it approaches the theoretical limit of 90 cm^{-1}. This strong influence of applied electric field is found only in tungsten bronze crystals; this effect is much weaker in $LiNbO_3$ and $BaTiO_3$.
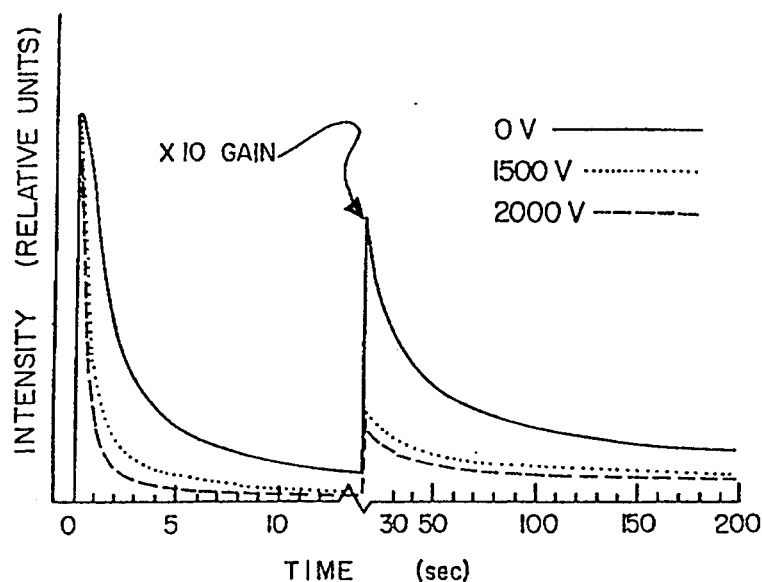

Figure 3.5 -- Photorefractive speed of response as a function of electric field.
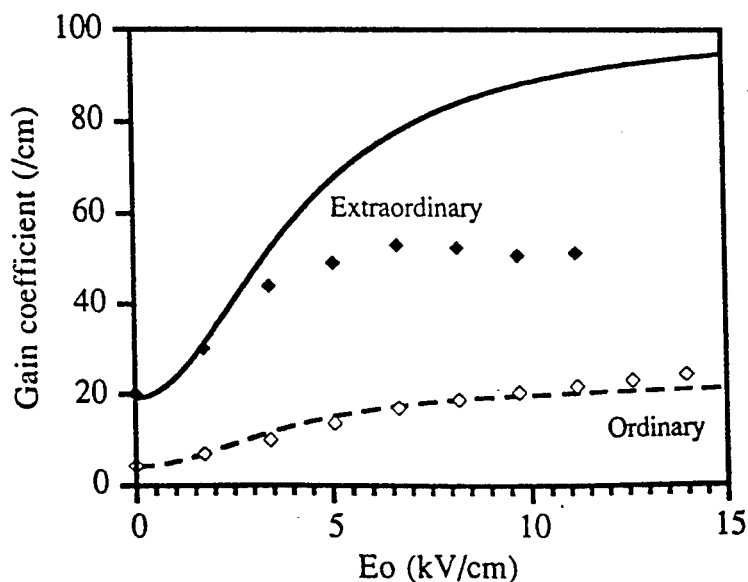
Figure 3.6 -- Photorefractive coupling as a function of electric field.

24

A dramatic increase in speed of response was obtained in these crystals by focusing the incoming laser light (1 W/cm^2) to higher intensities. Measurements at the University of Arkansas and ARL show a 2 to 3 order of magnitude improvement in speed. This indicates that protection systems employing a focusing step can achieve response times in the microsecond range. Prototype limiters have been constructed at the University of Arkansas (Fig. 3.7) using these enhancements to realize a 10 μs response time to 1 W/cm^2 incoming laser light. This result was obtained using a Ce-doped (0.02 wt%) SBN:60 crystal cube having dimensions of 6 x 6 x 6 mm with a 3 kV/cm electric field applied along the c -axis.
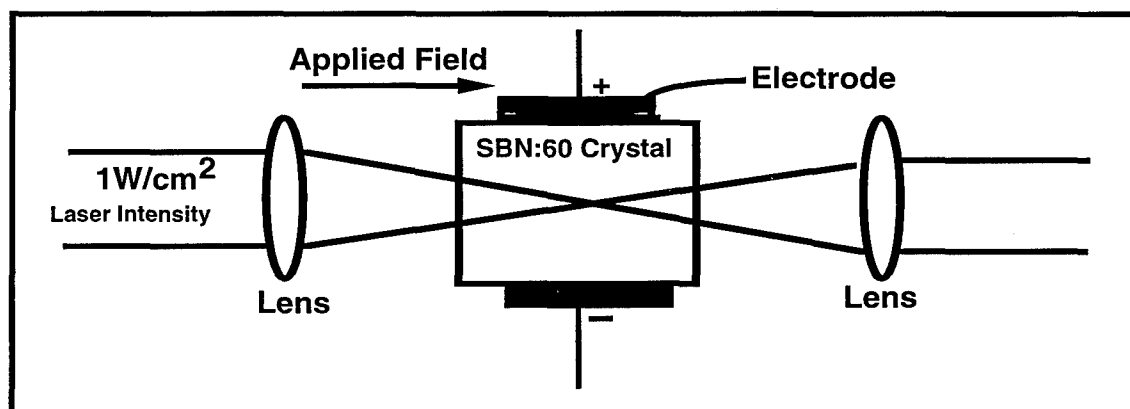
Figure 3.7 -- Prototype optical limiter fabricated using tungsten bronze crystals.

3.5   Double-Doping Schemes in Tungsten Bronze Crystals

Compared with the general observations of photorefractive speed and coupling with these dopants (Table 3.1), it may be said that the highest speed is achieved with the energetically deeper dopant ions, and the highest coupling with the shallower ions. From the standpoint of photorefractive efficiency, it must be kept in mind that this depends upon the local trapped charge density in the crystal, which in turn generates an electric field which is directly relatable to the position of the local quasi-Fermi level. For singly-doped crystals, the donor level also acts as a trap, with the number of occupied donor sites and the ionized empty trap sites being controlled by the dopant concentration and the concentration of compensating charged acceptors, N_a^-, which lie in the lower half of the bandgap. The problem here is that the trap/donor ratio is very difficult to

control in these crystals because they are partially self-compensating at growth.

Double-doping can be a viable alternative to obtain more control over the photorefractive performance. What is desirable is to utilize two dopants, one being a shallower trap which is nearly empty of electrons in dark equilibrium, and a deeper lying donor level which is nearly full, thus placing the Fermi level somewhere between the two levels, but preferably closer to the deep donor. These levels should be separated in energy by at least several kT (~ 0.2 eV), but the shallowest lying level should not be so close to the conduction band that it simply thermally re-emits any trapped carriers. In this regard, (Fe, Rh, Mo) are all acceptable co-dopants with Cr, and (Fe, Rh) with Ce. Ce may also be an effective co-dopant with Cr for the same reason. However, a perhaps more important consideration is the overall donor/acceptor ratio, N_d/N_a. In these n-type photorefractive crystals, the effective charge density is given by,
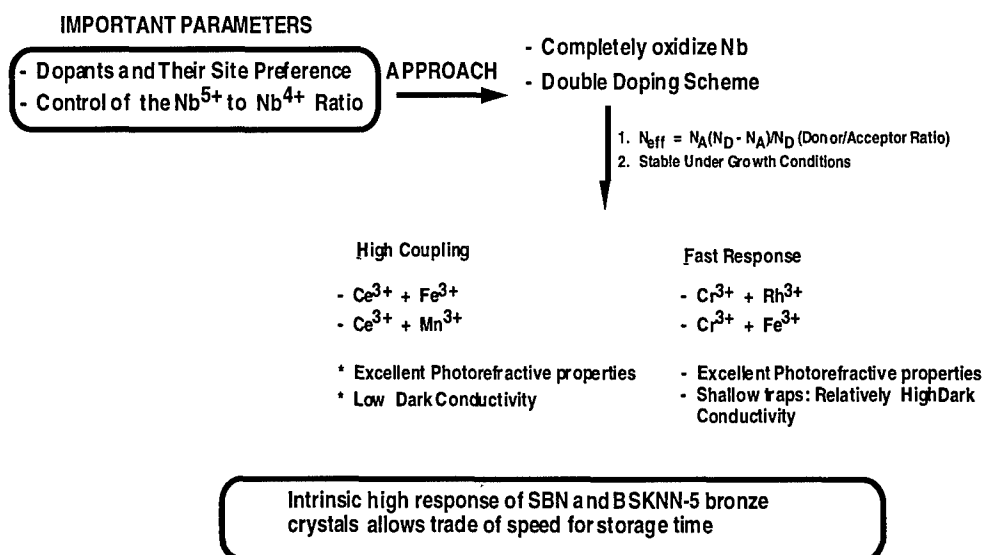
$$N_{eff} = N_a(N_d - N_a) / N_d \qquad (3.2)$$

with N_{eff} attaining a maximum value of $0.25N_d$ for $N_a = 0.5N_d$. Hence, control over N_d/N_a is a critical factor for optimizing N_{eff}, and thus, the photorefractive coupling. The dopant ions examined here all create donor/trap sites in the upper half of the band gap. However, in the evaluation of these dopant ions, it must be kept in mind that many, if not all, can have multiple valence states and energy levels in the band gap. Iron is probably a classic example of this, since it is well-known that Fe is an effective photorefractive dopant in $BaTiO_3$ in which it acts as an acceptor level in the lower half of the band gap in this p-type crystal. Indeed, early work by Morin and Oliver[48] on Fe-doped $SrTiO_3$ has shown the presence of several Fe levels, including a $Fe-V_{ox}$-Ti donor complex, covering nearly the full extent of the band gap in this perovskite. It is undoubtedly true that the same situation can be found in the tungsten bronzes, with perhaps even greater complexity due to the larger number of available lattice sites and potential site defect complexes. Hence, lacking a truly acceptor-type dopant, the donor/acceptor ratio in these crystals remains largely a matter of the extent of self-compensation by the individual dopant ions.

In our work on co-doped crystals, we have put emphasis on $Cr^{3+}+Mo^{4+}$-doped SBN:60 crystals having the highest energy separation between the two donor levels. In a (0.015 + 0.015 wt.%) $Cr^{3+}+Mo^{4+}$-doped SBN:60 crystal in a fully oxidized condition, the equilibrium (dark) Fermi level is located at 1.27 eV above 200 °C; this is slightly below the Mo^{4+} trap, indicating that it is nearly empty of electrons, whereas the Cr^{3+} donor level is full. This is not the full picture at room temperature, however, since an extrapolation of the high temperature conductivity using Eq. (1) predicts a conductivity of 3×10^{-20} Ω^{-1}-cm^{-1} at 23 °C, whereas the measured dark conductivity

is $\sim 5 \times 10^{-16}$. The reason for this is the presence of shallow donor levels, typically charge-compensating oxygen vacancies, which necessarily cause the Fermi level to rise closer to the conduction band at room temperature. This reflects upon the importance of minimizing the presence of unwanted shallow donor impurities or defects (vacancies) in these crystals in order to maximize the density of available deeper-lying empty trap sites which can retain trapped charge.

Optical results on $Cr^{3+}+Mo^{4+}$-doped SBN:60 crystals show very good photorefractive performance with coupling in the range of 10-15 cm^{-1} and response times of 1 to 10 milliseconds at 1 W/cm^2 intensity. We expect that it is possible to attain the desired speed of response ($<$ 1ms at 1 W/cm^2) and coupling (> 25 cm^{-1}) in these crystals with optimized Cr/Mo ratios. Work on other dopant combinations, such as $Ce^{3+}+ Mn^{3+}$, $Cr^{3+} + Rh^{3+}$, $Cr^{3+} + Fe^{3+}$, and $Ce^{3+} + Fe^{3+}$, has been initiated and the results are promising. The preliminary results for these investigations are summarized in Figure 3.8. Further information can be found in Section 4.0. We found that the first two dopant combinations are particularly promising to enhance the speed of response in these crystals, and further efforts on these doped crystals are essential. Our initial experiments indicate that using two independent dopant species, it is possible to better control the space charge density in these crystals. We expect that with further understanding of donor and acceptor species, it should be possible control the photorefractive properties in these materials.

IMPORTANT PARAMETERS

- Dopants and Their Site Preference   APPROACH
- Control of the Nb^{5+} to Nb^{4+} Ratio

- Completely oxidize Nb
- Double Doping Scheme

1. $N_{eff} = N_A(N_D - N_A)/N_D$ (Donor/Acceptor Ratio)
2. Stable Under Growth Conditions

High Coupling

- $Ce^{3+} + Fe^{3+}$
- $Ce^{3+} + Mn^{3+}$

* Excellent Photorefractive properties
* Low Dark Conductivity

Fast Response

- $Cr^{3+} + Rh^{3+}$
- $Cr^{3+} + Fe^{3+}$

- Excellent Photorefractive properties
- Shallow traps: Relatively High Dark Conductivity

Intrinsic high response of SBN and BSKNN-5 bronze crystals allows trade of speed for storage time

Figure 3.8 -- Double doping schemes in tungsten bronze crystals

In our evaluation of dopants in SBN and BSKNN crystals, it should be emphasized that the

energy level assignments for these dopants are necessarily confined to the donor/trap levels in the upper half of the band gap, since all of these crystals are n-type. This does not imply, however, that other energy levels -- particularly compensating ionized acceptor levels in the lower half of the band gap -- are not present. Indeed, such compensating levels must be presumed to exist in these crystals lacking any further evidence to the contrary. This is particularly evident in view of the very low dark (equilibrium) conductivities found in these crystals in spite of doping concentrations which approach 10^{+19} cm^{-3}. Hopefully one or more acceptor dopants can be found in the future which will move the equilibrium Fermi level into the lower half of the band gap and thus permit the full exploration of these important levels.

4.0   DOPANT STUDY

This section covers the modification of the current work assignment to cover the role of dopants, specifically as they affect the photorefractive speed and coupling, in tungsten bronze SBN:60 and BSKNN-2 single crystals. This work covers the progress for the period October, 1, 1992 to May 31, 1994 and includes single dopants and double-doping schemes in SBN:60 crystals.

Since October, 1, 1992, it was decided in consultation with Mr. Byong Ahn and Professor Greg Salamo that attention would be focused on a particular doping scheme in SBN:60 in order to determine the conditions under which a response time of 1 μs at 1 W/cm^2 can be achieved. Based on our earlier work, we selected Cr^{3+} + Mo^{4+} as the main dopants with Cr^{3+}+ Fe^{3+}, Ni^{2+} + Mo^{4+}, Rh^{3+} as back ups. These dopants were studied individually and in combination with other dopant ions. Table 4.1 summarizes the double doping schemes studied for SBN:60.

4.1   Growth of Doped SBN:60 Crystals

During this period, small doped SBN:60 crystal boules, typically producing 2 to 3 cut cubes (6 x 6 x 6 mm), were grown from a fresh melt in each case. This represents a change in our growth procedure which formerly made use of material left over from previous growth experiments. The growth conditions for these new SBN:60 crystals were as described in the earlier sections of this report. The cut, polished and poled crystal cubes and plates were supplied to NVESD (Mr. Byong Ahn) and the University of Arkansas (Professor G. J. Salamo) for photorefractive evaluation.

Beam fanning response times at 1 W/cm^2 were measured at the University of Arkansas for all the crystal samples and summarized in Table 4.1. The best response was 0.22 sec obtained for Mo^{4+}-doped SBN:60 with concentration of 0.015 wt% Mo^{4+}. Both higher and lower concentrations of Mo^{4+} show slower response, indicating that a concentration of 0.015 wt% is near optimum for this dopant. A similar behavior has been observed for Cr^{3+} - doped samples with an optimum response of 0.39 sec occurring at 0.015 wt% of Cr^{3+}.

The purpose of our double doping experiments was to maintain a fast response times and increase the coupling coefficient for SBN:60 and BSKNN-2. In the double doping schemes, we combined Cr^{3+} with other promising dopants, namely, Mo^{4+}, Fe^{3+} and Ce^{3+}. The best beam fanning response was achieved when Fe^{3+} was combined with Cr^{3+}, with a the response time

off 0.5 sec. We expect that a faster response can be obtained in this system by altering the $Cr^{3+}{:}Fe^{3+}$ concentration ratio. The coupling coefficient is significantly higher ($> 12\ cm^{-1}$) for this combination as compared to singly doped Cr^{3+} ($< 6\ cm^{-1}$). The $Cr^{3+} + Mo^{4+}$ combination shows similar results; however, the combination of $Cr^{3+} + Ce^{3+}$ shows much slower response and lowe coupling.

Table 4.1

Photorefractive Dopants in SBN:60 Crystals

Dopant	Beam Fan Response at $1W/cm^2$	Remarks
Chromium (Cr) Cr = 0.005% Cr = 0.010% Cr = 0.015% Cr = 0.025%	 2.6 sec 2.6 sec 0.390 sec 0.515 sec	 Promising result
Molybdenum (Mo) Mo = 0.005% Mo = 0.010% Mo = 0.015% Mo = 0.025%	 1.2 sec 4.0 sec 0.22 sec 1.09 sec	 Inconclusive result Promising result
$Cr^{3+} + Mo^{4+}$ Cr+Mo = 0.010% Cr+Mo = 0.015% Cr+Mo = 0.030% Cr+Mo = 0.040%	 0.70 sec 1.68 sec ----- -----	 Promising result Need more work
$Cr^{3+} + Fe^{3+}$ Cr+Fe = 0.015% Cr+Fe = 0.020%	 0.55 sec 0.50 sec	 Highly promising Highly promising
$Cr^{3+} + Ce^{3+}$ Cr+Ce = 0.015% Cr+Ce = 0.020%	 1.55 sec 0.90 sec	 Slow response

Based on this work, it appears that both high coupling and fast beam fanning response can be

achieved utilizing double doping schemes. However, further work is required to establish the effects of site preference and concentration. In the case of $Cr^{3+} + Mo^{4+}$ and $Cr^{3+} + Fe^{3+}$, both ions prefer the 6-fold coordinated sites in the tungsten bronze structure, while Ce^{3+} prefers the 12-fold coordination. This is a likely cause for the inferior performance of $Cr^{3+} + Ce^{3+}$ doped SBN:60, because energy transfer may not be efficient.

We have only just begun to explore the potential for double doping in tungsten bronze materials, and already we have demonstrated improved coupling with fast response. We therefore strongly recommend that a full scale investigation of these schemes be undertaken to optimize the performance of these materials for sensor protection.

5.0   CONCLUSIONS AND RECOMMENDATIONS

This program was awarded to Rockwell for the development of high performance photorefractive tungsten bronze materials for optical limiter applications (sensor protection). The success of this program is in part a product of the systematic study of the structure-property relationships within the tungsten bronze materials and the introduction of novel approaches to optical limiting. The best hosts for these applications were found to be SBN:60 and BSKNN-2, and our optimization of dopants concentrated on these crystals. The resulting photorefractive characteristics include a speed of response in the range of 10 μs and coupling >25 cm^{-1}. These photorefractive characteristics are sufficient to allow the fabrication of practical optical limiters for 1 W/cm^2 intensity laser light.

Using these high performance tungsten bronze materials, the University of Arkansas and NVESD formulated optical limiter concepts and constructed prototypes. Demonstrations using these prototypes showed the feasibility of their concepts for sensor protection when tungsten bronze materials were employed. To achieve the 10 μs response time, these prototypes used external electrical fields applied to the photorefractive crystals and optical systems to focus the incoming light onto the crystals.

Both the photorefractive materials and the limiter concepts are capable of substantial further improvement. Specifically, we need to further explore the performance-controlling features such as host-dopant relationships, oxidation/reduction to control dopant valence states, and the elimination of scattering defects for high intensity light. Our recommendations are as follows:

5.1   New Tungsten Bronze Hosts

We recently established the basic properties of two new tungsten bronze crystal systems exhibiting optical figures-of-merit significantly higher than SBN:60. These crystals are based on the $(Ba,Sr)_3TiNb_4O_{15}$ (BSTN) and $(Pb,Ba)_2(K,Na)Nb_5O_{15}$ (PBKNN) systems. Although the optical quality of these crystals needs to be improved, the speed of response in Ce-doped BSTN crystals is at least 20 times faster than in comparably doped SBN:60 with coupling >15 cm^{-1} .[57] We expect that the overall performance of these crystals will significantly improve with the use of appropriate doping schemes and a further improvement in crystal quality. It is expected that the incorporation of such high-performance crystals in optical limiters will reduce the time of response to 1 μs or less. As such, both BSTN and PBKNN crystals are potentially important

32

candidates for sensor protection applications in the future.

Our initial experiments on the growth of Pb^{2+} - containing tungsten bronze showed that the Czochralski technique was feasible, but control over Pb^{2+} losses is difficult due to volatilization. For this reason, further development of Pb^{2+} - containing tungsten bronzes was terminated under this program. In order to grow homogeneous crystals of decent size, a technique such as Bridgman growth should be employed.

5.2   Role of Dopants

To control photorefractive properties, i.e. the speed of response and coupling, one needs a specific donor/acceptor ratio which we found very difficult to control using a single dopant species. For this reason, we introduced the double-doping concept in this program, and as discussed in Section 4.5, it showed considerable promise in terms of maintaining fast response and sufficiently high coupling using Cr^{3+} and Mo^{4+}. We expect that the desired photorefractive properties can be achieved with a suitable donor/acceptor combination at optimum concentrations. Double-doping schemes should be considered in high performance crystal hosts such as BSTN or PBKNN which could show response times in the range of 1 μs or better.

At present, our knowledge of the energy levels for multivalence dopants remains largely incomplete. Measurements such as electron paramagnetic resonance (EPR), thermally stimulated conductivity (TSC) and photo-induced transient spectroscopy (PITS) could be of great value in further identifying these energy levels and their associated valence states in the crystal lattice.

5.3   Oxidation/Reduction States Of Dopants

Because the valence states of both the crystal host ions (e.g., Nb^{5+} / Nb^{4+}) and dopant ions are key factors controlling the photorefractive properties, it is important to maintain a uniform state of oxidation in all samples. Post-growth annealing of crystal samples ($\sim$ 500-650°C) can be used to ensure a uniform initial state of oxidation; however, subsequent repoling or processing at temperatures above 300°C can alter the oxidation states and thereby the photorefractive properties. For this reason, we recommend that careful control of sample preparation and processing be maintained.

5.4   Test Device Concepts

The prototype optical limiters fabricated using tungsten bronze SBN:60 crystal samples at the University of Arkansas show great promise for Army sensor protection applications. To follow up on this development, it is necessary to undertake a detailed evaluation of these prototypes in Army Research Laboratory test beds. Based on results from such studies, the optimal parameters for specific applications can jointly be worked out, and any required changes in limiter designs can be established. A collaboration among Army engineers, Professor Greg Salamo and the Ferroelectric and Optical Materials Department at Rockwell should pursue such an effort.

6.0   CRYSTAL SAMPLES SUPPLIED

From the beginning of this program in 1988, Rockwell has been growing boules of photorefractive tungsten bronze crystals specifically for optical limiter studies, and supplying crystal products (cubes, plates and wedges) for optical evaluation at NVESD and the University of Arkansas. Based on these evaluations, modifications in host composition and dopants were made and new crystals samples were supplied each time. In order to keep the cost of materials low, Rockwell and NVESD agreed to limit crystal boule sizes to produce 2 or 3 cubes per crystal and reuse the scrap material left from these boules in subsequent growths of identical compositions including the same dopant. In our initial experiments, the appropriate amount of dopants for each case was determined based on how many grams of crystal were pulled from the melt, and this proportion was used in all subsequent growth experiments. This procedure worked without any problems; however, after September, 1993, a fresh melt was used for each doped crystal.

Initially, crystal samples were sent to Mary J. Miller (contract monitor) and Edward J. Sharp of NVESD. At the end of 1992, Mr. Byong Ahn became the contract monitor for this program, and subsequent crystal samples were sent to him. In this latter period, crystal samples were also sent separately to Professor Greg Salamo of the University of Arkansas for optical studies. A complete list of crystal samples supplied since 1988, all of which were optically polished and poled prior to delivery, is given below:

6.1   Samples Supplied to Ms. Mary Miller and Dr. Ed Sharp

Feb 22, 1988

Fe - doped SBN:60 (#187), Fe = 0.01 wt%, 5 x 5 x 5 mm cube

June 24, 1988

Cr - doped SBN:60 (# 348), Cr = 0.015 wt%, 6 x 6 x 6 mm cube

October 28, 1988

Cr - doped SBN:75 (# 375), Cr = 0.02 wt%, 6 x 6 x 6 mm cube

Dec 23, 1988

Fe - doped SBN:60 (# 197), Fe = 0.015 wt%, 5 x 5 x 5 mm cube

Ce - doped SBN:60, Ce = 0.02 wt%, 5 x 5 x 3 mm cube
March 1, 1989

Cr - doped SBN:75 (# 371), Cr= 0.015 wt%, 6 x 6 x 6 mm cube

Rh - doped SBN:60 (# 353), Rh = 0.02 wt%, 6 x 6 x 6 mm cube

La + Ce - doped SBN:60 (# 363), Ce = 0.02 wt%, 6 x 6 x 6 mm cube

April 19, 1989

Cr - doped BSKNN-2, Cr = 0.02 wt%, 6 x 6 x 6 mm cube

Fe - doped SBN:60 (# 372), Fe = 0.015 wt%, 5 x 5 x 3 mm cube

Undoped BSKNN-2, 5 x 3 x 1 mm wedge

Febuary 10, 1990

Rh - doped SBN:60 (# 390),   Rh = 0.025 wt%, 6 x 6 x 6 mm cube

Rh - doped SBN:60 (# 392), Rh = 0.035 wt%, 6 x 6 x 6 mm cube

Rh - doped SBN:60 (# 396), Rh = 0.045 wt%, 6 x 6 x 6 mm cube

Rh - doped SBN:60 (# 397), Rh = 0.07 wt%, 6 x 6 x 6 mm cube

Fe - doped SBN:60 (# 372), Fe = 0.012 wt %, 6 x 6 x 6 mm cube

May 4, 1990

Cr - doped SBN:60 (# 399), Cr = 0.06 wt%, 6 x 6 x 6 mm cube

June 25, 1990

Undoped SBN:60 , 5 x 5 x 1 mm plates. Supplied 4 plates. Crystals were not grown
under this program.

July 10, 1990

Rh - doped SBN:60 (# 493), Rh = 0.100 wt%, 6 x 6 x 6 mm cube

August 8, 1990

Rh - doped BSTN-1, Rh = 0.015 wt % 3 x 5 x 5 mm cube (grown under Rockwell IR&D).

October 10, 1990

Rh - doped BSKNN-2, Rh = 0.015 wt%, 5 x 5 x 5 mm cube

January 4, 1991

Ce - doped SBN:60, Ce = 0.03 wt%, 1.3 x 1.3 x 0.7 mm cube
(Special cube for device testing)

Febuary 12, 1991

Co - doped BSKNN -2, Co = 0.015 wt%, 6 x 6 x 6 mm cube with [110] faces

Co - doped BSKNN-2, Co = 0.015 wt%, 1 x 1 x 6 mm cube with [110] faces

Co - doped BSKNN-2, Co = 0.015 wt%, 1 x 1 x 5 mm plate with [100] faces

March 15, 1991

Ce - doped SBN:60, Ce = 0.015 wt %, 1.4 x 1. x 1 cm cube
(Specifically fabricated for device testing)

April 19, 1991

Ce - doped SCNN: Ba, Ce = 0.015 wt%, 5 x 5 x 2 mm plate

Fe - doped SBN:60 (#ff 0220), Fe = 0.015 wt%, 5 x 5 x 5 mm cube

July 30, 1991

Rh - doped SBN:50, Rh = 0.01 wt%, 5 x 5 x 5 mm cube (grown under Rockwell IR&D).

Cr + Fe - doped SBN:60 (#ff 0222), 5 x 5 x 5 mm cube

Ce - doped BSCNN, (# 134), Ce = 0.02 wt%, 4 x 4 x 3 mm cube

November 26, 1991

Cr + Mo - doped SBN:60, Cr + Mo = 0.02 wt%, 6 x 6 x 6 mm cubes:
  - One oxidized sample
  - One reduced sample

Rh - doped BSTN-8 (#9), Rh = 0.015 wt %, 4 x 4 x 3 mm cube
(Crystal sample on loan)

December 6, 1992

Ce - doped BSKNN-2, Ce = 0.015 wt%, 6 x 6 x 5 mm special 45° cut cube

Ce - doped BSKNN-2, Ce = 0.015 wt%, 1 x 1 x 5 mm plate

6.2   Samples Supplied to Mr. Byong Ahn

December 8, 1992

Cr + Mo - doped SBN:60 (ff 1212), Cr + Mo = 0.01 wt%, 6 x 6 x 6 x cube

An additional cube was supplied on December 12, 1992

December 23, 1992

Cr + Mo - doped SBN:60, Cr + Mo = 0.015 wt%, , 6 x 6 x 6 mm cube

January 20, 1993

As per the request of Mr. Byong Ahn, the following four crystal samples were sent to NVESD for display purposes:

Rh - doped SBN:60, Rh = 0.02 wt%, 6 x 6 x 6 mm cube

Cr - doped SBN:60, Cr = 0.015 wt%, 6 x 6 x 6 mm cube

Undoped SBN:60, 2 cm diameter disk

Undoped SBN:60, 25 x 15 x 1 mm plate

February 5, 1993

Cr + Mo - doped SBN:60, Cr + Mo = 0.02 wt%,   6 x 6 x 6 mm cube

Cr + Mo - doped SBN:60, Cr + Mo = 0.02 wt%,   6 x 6 x 1 mm plate

March 22, 1993

Cr + Fe - doped SBN:60, Cr + Fe = 0.015 wt%, 6 x 6 x 6 mm cube

Cr + Fe - doped SBN:60, Cr + Fe = 0.015 wt%, 6 x 6 x 1 mm plate

Cr + Fe - doped SBN:60, Cr + Fe = 0.02 wt%, 6 x 6 x 6 mm cube

June 9, 1993

Cr + Fe - doped SBN:60, Cr + Fe = 0.03 wt%, 6 x 6 x 6 mm cube

Ni + Mo - doped SBN:60, Ni + Mo = 0.015 wt%, 6 x 6 x 6 mm cube

Ni + Mo - doped SBN:60, Ni + Mo = 0.015 wt%, 6 x 6 x 1 mm plate

July 7, 1993

Cr + Mo - doped SBN:60, Cr = 0.01 wt%, Mo = 0.005 wt%, 6 x 6 x 6 mm cube

August 8, 1993

Cr + Mo - doped SBN:60, Cr = 0.005 wt%, Mo = 0.01 wt%, 6 x 6 x 6 mm cube

Cr + Mo - doped SBN:60, Cr = 0.005 wt%, Mo = 0.01 wt%, 6 x 6 x 1 mm plate

September 2, 1993

Cr + Mo - doped SBN:60, Cr = 0.015 wt%, Mo = 0.015 wt%, 6 x 6 x 6 mm cube

Cr + Mo - doped SBN:60, Cr = 0.015 wt%, Mo = 0.015 wt%, 6 x 6 x 1 mm plate

November 27, 1993

Cr + Fe - doped SBN:60, Cr = 0.015 wt%, Fe = 0.001 wt%, 6 x 6 x 6 mm cube

December 14, 1993

Cr - doped SBN:60, Cr = 0.005 wt%, 6 x 6 x 6 mm cube

December 23, 1993

Cr - doped SBN:60, Cr = 0.025 wt%, 6 x 6 x 6 mm cube

February 26, 1994

Mo - doped SBN:60, Mo = 0.015 wt%, 6 x 6 x 6 mm cube

Mo - doped SBN:60, Mo = 0.025 wt%, 6 x 6 x 6 mm cube

July 23, 1994

Mo - doped SBN:60, Mo = 0.005 wt%, 6 x 6 x 6 mm cube

Mo - doped SBN:60, Mo = 0.005 wt%, 6 x 6 x 1 mm plate

Mo - doped SBN:60, Mo = 0.010 wt%, 6 x 6 x 6 mm cube

Mo - doped SBN:60, Mo = 0.01 wt%, 6 x 6 x 2 mm plate

Cr - doped SBN:60, Cr = 0.005 wt%, 6 x 6 x 2 mm plate

Cr - doped SBN:60, Cr = 0.005 wt%, 6 x 6 x 6 mm cube

Cr - doped SBN:60, Cr = 0.005 wt%, 6 x 6 x 6 mm cube

Cr + Mo - doped SBN:60, Cr = 0.010 wt%, Mo = 0.005 wt%, 6 x 6 x 6 mm cube

November 23, 1994

Rh - doped SBN:60, 1.3 cm diameter x 4 cm length crystal boule. For display.

6.3 Samples Supplied to Greg Salamo, The University of Arkansas

December 8, 1992

Cr + Mo - doped SBN:60 (#ff 1212), Cr + Mo = 0.01 wt%, 6 x 6 x 6 cube

December 23, 1992

Cr + Mo - doped SBN:60, Cr + Mo = 0.015 wt%, 6 x 6 x 6 mm cube

February 5, 1993

Cr + Mo - doped SBN:60, Cr + Mo = 0.02 wt%, 6 x 6 x 6 mm cube

March 22, 1993

Cr + Fe - doped SBN:60, Cr + Fe = 0.015 wt%, 6 x 6 x 6 mm cube

Cr + Fe - doped SBN:60, Cr + Fe = 0.020 wt%, 6 x 6 x 6 mm cube

June 9, 1993

Cr + Fe - doped SBN:60, Cr + Fe = 0.030 wt%, 6 x 6 x 6 mm cube

Ni + Mo - doped SBN:60, Ni + Mo = 0.015 wt%, 6 x 6 x 6 mm cube

July 7, 1993

Cr + Mo - doped SBN:60, Cr = 0.010 wt%, Mo = 0.005 wt%, 6 x 6 x 6 mm cube

August 8, 1993

Cr + Mo - doped SBN:60, Cr = 0.005 wt%, Mo = 0.010 wt%, 6 x 6 x 6 mm cube

September 2, 1993

Cr + Mo - doped SBN:60, Cr = 0.015 wt%, Mo = 0.015 wt%, 6 x 6 x 6 mm cube

September 17, 1993

Cr + Mo - doped BSKNN-2, Cr = 0.0075 wt%, Mo = 0.0075 wt%, 6 x 6 x 6 mm cube

November 27, 1993

Cr + Fe - doped SBN:60, Cr = 0.015 wt%, Fe = 0.010 wt%, 6 x 6 x 6 mm cube

December, 14, 1993

Cr + Fe - doped SBN:60, Cr = 0.005 wt%, 6 x 6 x 6 mm cube

December 23, 1993

Cr + Fe - doped SBN:60, Cr = 0.025 wt%, 6 x 6 x 6 mm cube

February 26, 1994

Cr + Fe - doped SBN:60, Mo = 0.015 wt%, 6 x 6 x 6 mm cube

Cr + Fe - doped SBN:60, Mo = 0.025 wt%, 6 x 6 x 6 mm cube

Cr + Fe - doped SBN:60, Mo = 0.010 wt%, 6 x 6 x 6 mm cube

Cr - doped SBN:60, Cr = 0.005 wt%, 6 x 6 x 6 mm cube

Cr - doped SBN:60, Cr = 0.005 wt%, 6 x 6 x 6 mm cube

Cr + Mo - doped SBN:60, Cr = 0.010 wt%, Mo = 0.005 wt%, 6 x 6 x 6 mm cube

7.0 REFERENCES

1. R.B. Maciolek and S.T. Liu, J. Electron. Mater. **2**, 191 (1973).

2. R.B.Maciolek T.L. Schuller and S.T. Liu, J. Electron. Mater. **5**, 415 (1976).

3. S. Kuroda and K. Kubota, J. Phys. Chem. Solids **44**, 527 (1983).

4. E.G. Spencer, P.V. Lenzo, and A.A. Ballman, Proc. IIIE **52**, 2074 (1967).

5. A. M. Glass, J. Appl. Phys. **40**, 4699 (1969).

6. P.V. Lenzo, E.G. Spencer and A.A. Ballman, Appl. Phys. Lett. **11**, 23 (1967).

7. R.L. Townsend and J.T. LaMacchia, J. Appl. Phys. **51**, 88 (1970).

8. J.J. Amodei, D.L. Staebler and A.W. Stephens, Appl. Phys. Lett. **18**, 507 (1971).

9. J.B. Thaxter, Appl. Phys. Lett. **15**, 210 (1969).

10. W.W. Ho, W.F. Hall, R.R. Neurgaonkar, R.E. DeWames and T.C. Lim, Ferroelectrics **38**, 63 (1981).

11. G. Rakuljic, A. Yariv and R.R. Neurgaonkar, J. Opt. Eng. **25**, 1212 (1986).

12. O. Eknoyan, C.H. Bulmer, H.F. Taylor, W.K. Burns, A.S. Greenblatt, L.A. Beach and R.R. Neurgaonkar, Appl. Phys. Lett. **48**, 13 (1986).

13. M.D. Ewbank, R.R. Neurgaonkar, W.K. Cory and J. Feinberg, Appl. Phys. Lett. **62**(2), 373 (1987).

14. B. Bobbs, M. Matloubian, H.R. Fetterman, R.R. Neurgaonkar and W.K. Cory, Appl. Phys. Lett. **48**, 1642 (1986).

15. E.J. Sharp, M.J. Miller, G.L. Wood, W.W. Clark III, G. Salamo and R.R. Neurgaonkar, Appl. Phys. Lett. **52**, 765 (1987).

16. G.L. Wood, W.W. Clark III, M.J. Miller, E.J. Sharp, G. Salamo and R.R. Neurgaonkar, J. Quantum Electronics **23**(12), 2126 (1987).

17. J.F. Jelsma, R.R. Neurgaonkar and W.K. Cory, Proc. SPIE **832**, 198 (1987).

18. G.J. Salamo, M.J. Miller, W.W. Clark III, G.L. Wood, E.J. Sharp and R.R. Neurgaonkar, Appl. Optics **27**(21), 4356 (1988).

19. E.J. Sharp, M.J. Miller, G.J. Salamo, W.W. Clark III, G.L. Wood, and R.R. Neurgaonkar, Ferroelectrics **87**, 335 (1988).

20. K. Sayano, G.A. Rakuljic, A. Agranat, A. Yariv and R.R. Neurgaonkar, Optics. Lett. **14**(9), 459 (1989).

21. G. Wood, B. P. Ketechel and R. R. Neurgaonkar, " Photorefractive properties of Cr/Mo doped SBN:60", Submitted to Appl. Phys. lett. (1995).

22. J. Ford, Y. Taketomi, S. Lee, D. Bize, S. Feinman and R.R. Neurgaonkar, Proc. SPIE **1148**, 12 (1989).

23. R.R. Neurgaonkar, W.K. Cory, J.R. Oliver, E.J. Sharp, G.L. Wood, M.S. Miller, W.W. Clark III and G. Salamo, Mat. Res. Bull. **23**, 1459 (1988).

24. R.R. Neurgaonkar, J.G. Nelson, J.R. Oliver and L.E. Cross, Mat. Res. Bull. **25**, 959 (1990).

25. R.R. Neurgaonkar, J.R. Oliver and J.G. Nelson, private communication.

26. R.R. Neurgaonkar, M.H. Kalisher, T.C. Lim, E.J. Staples and K.L. Keester, Mat. Res. Bull. **15**, 1305 (1980).

27. R.R. Neurgaonkar, W.K. Cory, W.W. Ho, W.F. Hall, and L.E. Cross, Ferroelectrics **38**, 857 (1981).

28. R.R. Neurgaonkar, W.K. Cory, Ferroelectrics **35**, 301 (1983).

29. R.R. Neurgaonkar, W.W. Ho, W.K. Cory, W.F. Hall, and L.E. Cross, Ferroelectrics **51**, 185 (1984).

30. R.R. Neurgaonkar, Proc. SPIE **465**, 97 (1984).

31. R.R. Neurgaonkar and L.E. Cross, Mat. Res. Bull. **21**, 893 (1986).

32. R.R. Neurgaonkar and W.K. Cory, J. Opt. Soc. Am. 3(B), 276 (1986).

33. R.R. Neurgaonkar, W.K. Cory, J.R. Oliver and L.E. Cross, Proc. SPIE **567**, 11 (1985).

34. R.R. Neurgaonkar, W.K. Cory, J.R. Oliver and L.E. Cross, Mat. Res. Bull. **24**, 1025 (1989).

35. R.R. Neurgaonkar, W.K. Cory, J.R. Oliver, M.J. Miller, W.W. Clark III, G.L. Wood, and E.J. Sharp, J. Cryst. Growth **84**, 629 (1987).

36. R.R. Neurgaonkar, W.K. Cory and J.R. Oliver, Proc. SPIE **739**, 91 (1987).

37. R.R. Neurgaonkar, W.K. Cory, J.R. Oliver, M.D. Ewbank and W.F. Hall, J. Opt. Eng. **26**(5), 392 (1987).

38. M.H. Francombe and B. Lewis, Acta Cryst. **11**, 696 (1958).

39. L.G. Van Uitert, H.J. Levinstein, J.J. Rubin, C.D. Capio, E.F. Dearborn and W.A. Bonner, Mat. Res. Bull. **3**, 47 (1968).

40. P.B. Jamieson, S.C. Abrahams, J.L. Bernstein, J. Chem. Phys. 48, 5048 (1968).

41. T. Fukuda, Jap. J. Appl. Phys. **9**, 599 (1970).

42. T.V. Tiaou, N.N. Krainnik, I.H. Ismailzade, V.A. Isupov, and F.A. Ageve, Izv. Acad. Nauk. SSSR, Ser. Phys. **35**, 1825 (1971).

43. M.H. Framcombe, Acta Cryst. **13**, 131 (1960).

44. V.A. Isupov and V.I. Kosiakov, Zh. Tekh. Fiz. **28**, 2175 (1958).

45. J.R. Oilver, R.R. Neurgaonkar and L.E. Cross, J. Appl. Phys. **64**, 37 (1998).

46. W.L. Warren, D. Dimos and B.A. Tuttle, J. Am. Ceramic Soc. **77**, 2753 (1994).

47. K. Megumi, N. Nagatsuma, K. Kashiwada and Y. Furuhata, Mater. Sci. **11**, 1583 (1976).

48. F.J. Morin and J.R. Oliver, Phys. Rev. **B8**, 5847 (1973).

49. P. Yeh, Appl. Optics **26**, 602 (1987).

50. G.J. Salamo, B.D. Monson, W.W. Clark III, G.L. Wood, and R.R. Neurgaonkar, Appl. Optics **30**, 1847 (1991).

51. K. Sayano, A. Yariv and R.R. Neurgaonkar, Proc. SPIE **1148**, 7 (1989).

52. W.W. Clark III, G.L. Wood, M.J. Miller, E.J. Sharp, G.J. Salamo, B.D. Monson and R.R. Neurgaonkar, Appl. Optics **29**, 1249 (1990).

53. K. Sayano, A. Yariv and R.R. Neurgaonkar, Optics Lett. **15**, 9 (1990).

54. K. Sayano, A. Yariv and R.R. Neurgaonkar, J. Appl. Phys. **67**, 1594 (1990).

55. M. Fleischer and H. Meixner, J. Am. Ceramic Soc. **75**, 1666 (1992).

56. R.C. Baetzold, Phys. Rev. B**48**, 5789 (1993).

57. G.L. Wood and R.R. Neurgaonkar, Opt. Lett. **17**, 94 (1992).

8.0   APPENDIX

GROWTH AND OPTICAL PROPERTIES OF FERROELECTRIC TUNGSTEN BRONZE CRYSTALS

R. R. NEURGAONKAR, W. K. CORY and J. R. OLIVER

Rockwell International Science Center, Thousand Oaks, CA 91360 USA

and

E. J. SHARP, G. L. WOOD and G. J. SALAMO

Center for Night Vision and Electro-Optic, Fort Belvoir, VA 22060-5677 USA

The state of the art in the Czochralski growth of various optical-quality ferroelectric tungsten bronze single crystals is reviewed with respect to crystal structure, phase transitions and cationic make-up. Based on our growth of over 25 single crystal bronzes, we have classified these bronzes into four categories having distinctly different ferroelectric and optical characteristics. With the use of this classification, optimal bronzes can be chosen for specific electro-optic and photorefractive applications.

INTRODUCTION

Tungsten bronze (T.B.) ferroelectrics are very useful for electro-optic, piezoelectric, pyroelectric and millimeter wave applications, and more recently for photorefractive applications.[1-21] Considerable work has been published on the development of this family of materials; however, initially these materials did not find widespread application due to the lack of availability of crystals of adequate size and quality. At the Rockwell International Science Center, we have systematically studied the major growth problems, crystal habits and classification of these materials based on their ferroelectric and optical properties.[22-37] In this paper, we report our major findings on the growth of these crystals, their classification and potential applications.

BACKGROUND: FUNDAMENTAL PROPERTIES

A number of ferroelectrics of present or potential commercial importance have the tungsten bronze structure. This structure is typified by oxygen octahedra linked at the corners in a complex way to yield three types of openings, two of which normally contain the A_1 and A_2 cations as shown in Figure 1. The B cations, typically niobium (Nb^{5+}) or tantalum (Ta^{5+}), are inside the oxygen octahedra. The tungsten bronze compositions are characterized by the chemical formulae $(A_1)_4(A_2)_2C_4B_{10}O_{30}$ or $(A_1)_4(A_2)_2B_{10}O_{30}$, in which the A_1 cations are in the 15-
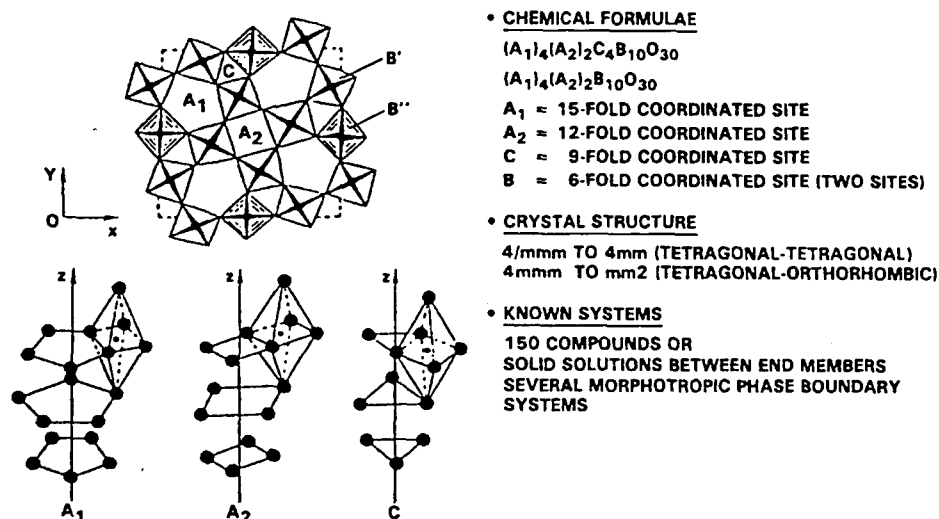
- CHEMICAL FORMULAE

  $(A_1)_4(A_2)_2C_4B_{10}O_{30}$

  $(A_1)_4(A_2)_2B_{10}O_{30}$

  A_1 = 15-FOLD COORDINATED SITE
  A_2 = 12-FOLD COORDINATED SITE
  C = 9-FOLD COORDINATED SITE
  B = 6-FOLD COORDINATED SITE (TWO SITES)

- CRYSTAL STRUCTURE

  4/mmm TO 4mm (TETRAGONAL-TETRAGONAL)
  4mmm TO mm2 (TETRAGONAL-ORTHORHOMBIC)

- KNOWN SYSTEMS

  150 COMPOUNDS OR
  SOLID SOLUTIONS BETWEEN END MEMBERS
  SEVERAL MORPHOTROPIC PHASE BOUNDARY
  SYSTEMS

FIGURE 1   Projection of tungsten bronze structure parallel to (001).

fold coordinated site, the A_2 cations are in the 12-fold coordinated site, the C cations are in the 9-fold coordinated site and the B cations are in two different 6-fold coordinated sites. Detailed descriptions of this structure have been given in several articles.[38-40] Only two compositions, $K_3Li_2Nb_5O_{15}$ and $K_3Li_2Ta_5O_{15}$, can be represented by the first chemical formula where all five crystallographic sites are filled.[41-42] For this reason, these compositions are known as "stuffed" bronzes. All other tungsten bronzes are called either "filled" or "unfilled" bronzes with the 9-fold coordinated site vacant and the 15- and 12-fold coordinated sites either fully or partially occupied. For example, lead metaniobate and strontium barium niobate have unfilled unit cells containing $Pb_5Nb_{10}O_{30}$ and $(Sr, Ba)_5Nb_{10}O_{30}$ (usually simplified to $PbNb_2O_6$ and $(Sr, Ba)Nb_2O_6$) where the A sites are only 5/6 filled. Although the presumption is that the distribution among the 15- and 12-fold coordinated A sites is random, more likely in SBN, Ba^{2+} predominantly occupies the 15-fold coordinated site since Ba^{2+} (1.74 Å) is substantially larger than Sr^{2+} (1.54 Å).

Like the ferroelectric perovskite family, the bronze family embraces more than 150 compounds and solid solutions including several morphotropic phase boundary systems.[43-44] Because of the structural complexity which accommodates a wide range of cationic substitutions, often the ferroelectric transition can be achieved in the desired temperature range with suitable ferroelectric and optical properties.

POLARIZATION STATES IN TUNGSTEN BRONZES

Bronze crystals are in the prototypic point group 4/mmm. Customarily the 4-fold symmetry axis is oriented along the (3), or z axis.
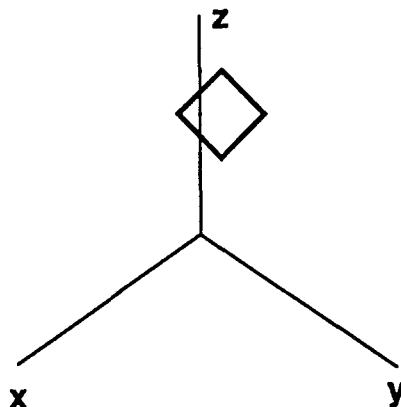
In the Aizo/Shuvalov classification, permitted ferroelectric species for 4/mmm in descending order of symmetry are:

1. 4/mmm (1) D 4 F 4 mm
2. 4/mmm (2) D 2 F mm2
3. 4/mmm (4) A 2 F m
4. 4/mmm (4) A 4 F m
5. 4/mmm (8) A 1 F 1

Only solutions (1) and (2) have been found so far in the macrosymmetry of any known bronze (Figure 2a). For these two states:

1. $P_z^2 \neq 0$, $Ps = \pm P_z(s)$

    Two domain states oriented along the 4-fold axis.

2. $P_x^2 = P_y^2 \neq 0$, $P_z^2 = 0$

    $\langle 110 \rangle + Ps$: $+ Ps$: 0

    $\langle 110 \rangle - Ps$: $+ Ps$: 0

    $\langle 110 \rangle - Ps$: $- Ps$: 0

    $\langle 110 \rangle + Ps$: $- Ps$: 0

    Four states oriented along the $\langle 110 \rangle$ family, i.e., along the 2-fold axes.

For the point group 4/mmm, the permitted ferroelastic states are:

1. 4/mmm (2) D 2 F mmm
2. 4/mmm (4) A 2 F 2/m
3. 4/mmm (4) A 2 F 2/m
4. 4/mmm (8) A 1 F 1

Of these states, only (1) has been observed in any known bronze macrosymmetry. In mmm the square cross section of the section normal to 4 experiences a sheer $\pm X_{12}$.

(b)

(a)

FIGURE 2   Ferroelectric/ferroelastic phase transitions and polar directions in tungsten bronze crystals.

+ X$_{12}$

Possible Ferroelastic Twin Wall
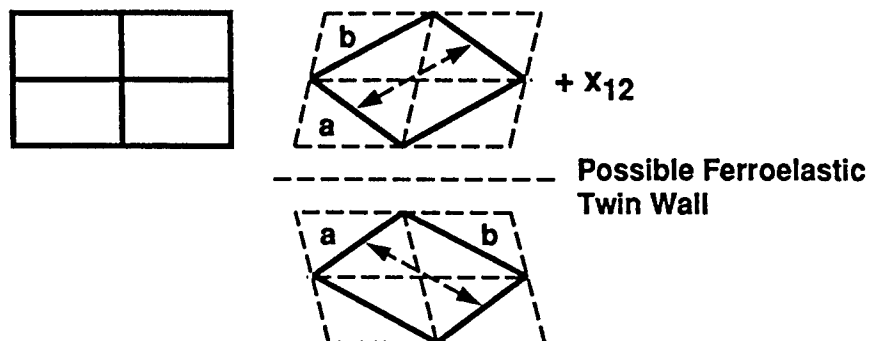
It is possible for the ferroelectric 4/mmm (1) DF 4 mm state to occur first on cooling, then the ferroelastic 4 mm (2) D 2 F mm2. This is depicted in Figure 2b. Note that the polar axis is $\pm P_z$ as in the original tetragonal term.

CRYSTAL DEVELOPMENT

Table I lists a number of tungsten bronze single crystals grown in our work and their associated growth conditions. The Czochralski pulling technique was used for

TABLE I
Ferroelectric tungsten bronze crystals grown at Rockwell

Composition	Growth Temp (°C)	Pull Rate (mm/hr)	Sym	Diameter (cm)	T_c (°C)	Phase Transitions
$Sr_{0.75}Ba_{0.25}N_2O_6$ (SBN:75)	1480	4-5	4mm	4.0	56	One
$Sr_{0.6}Ba_{0.4}Nb_2O_6$ (SBN:60)	1485	5-7	4mm	5.0	78	One
$Sr_{0.5}Ba_{0.5}Nb_2O_6$ (SBN:50)	1485	5-6	4mm	4.0	128	One
$Sr_{0.4}Ba_{0.6}Nb_2O_6$ (SBN:40)	1500	3-4	4mm	2.0	190	One ·
$Ba_{1.5}Sr_{0.5}K_{0.5}Na_{0.5}Nb_5O_{15}$	1470	3-4	4mm	1.5	209	One
$BaSrK_{0.75}Na_{0.25}Nb_5O_{15}$	1475	3-4	4mm	1.5	178	One
$Ba_{0.5}Sr_{1.5}K_{0.75}Na_{0.25}Nb_5O_{15}$	1475	4-5	mm2	2.0	172	Two?
$Sr_{1.9}Ca_{0.1}NaNb_5O_{15}$	1500	2-3	mm2	1.0	270	Two
$Sr_{1.8}Sr_{0.2}NaNb_5O_{15}$	1500	2-3	mm2	1.0	270	Two
$K_3Li_2Nb_5O_{15}$	1100	1-2	4mm	1.0	370	One
$K_3LiNaNb_5O_{15}$	1100	1-2	4mm	1.0	340	One
$Sr_2KNb_5O_{15}$	1450	3-4	4mm	1.5	157	One
$Pb_{0.6}Ba_{0.4}Nb_2O_6$ (PBN:60)	1350	1-2	4mm	1.5	320	One
$Pb_2KNb_5O_{15}$	1340	2-3	mm2	2.0	360	One
$K_2BiNb_5O_{15}$	1200	3-4	mm2	2.0	420	?
$Ba_2LiNb_5O_{15}$	1400	1-2	mm2	1.0	560	Two
$Ba_4Sr_2Ti_2Nb_8O_{30}$	1480	3-4	4mm	1.5	168	One
$Ba_3Sr_3Ti_2Nb_8O_{30}$	1480	2-3	4mm	1.5	140	One
$Ba_{2.5}Sr_{3.5}Ti_2Nb_8O_{30}$	1490	1-2	4mm	1.8	110	One
$Sr_4Ca_2Ti_2Nb_8O_{30}$	1500	2-3	mm2	1.0	200	Two
$Ba_4Ca_2Ti_2Nb_8O_{30}$	1460	1-2	mm2	1.0	175	Two

Sym = Symmetry.

these growths, with the crystals pulled from 5×5 cm platinum crucibles in an oxygen atmosphere to minimize the reduction of Nb^{5+} to Nb^{4+}. All of the crystals listed in Table I were grown along the $\langle 001 \rangle$ direction, except for the $K_3Li_2Nb_5O_{15}$ crystals where the best growth direction was found to be along the $\langle 110 \rangle$ direction. Crystal cracking during cool-down through the paraelectric/ferroelectric phase transition was initially a problem for most of these crystals, but this problem has now been minimized, particularly for SBN, BSKNN and BSTN.

Based on ferroelectric and optical studies of both tetragonal and orthorhombic bronze crystals, we have classified this family into four different groups shown in Figure 3.

1. Crystals exhibiting strong transverse effects with 4 mm symmetry (e.g. SBN. $Sr_2KNb_5O_{15}$, $Ba_6Ti_2Nb_8O_{30}$): $\langle 001 \rangle$ polar axis.
2. Crystal exhibiting strong longitudinal effects with 4 mm symmetry (e.g. BSKNN, $K_3Li_2Nb_5O_{15}$): $\langle 001 \rangle$ polar axis.
3. Crystal exhibiting strong transverse and longitudinal effects with mm2 symmetry (e.g. $Sr_{2-x}Ca_xNaNb_5O_{15}$): $\langle 001 \rangle$ polar axis.
4. Crystals exhibiting strong longitudinal effects with mm2 symmetry (e.g. $Pb_2KNb_5O_{15}$, $Pb_{1-x}Ba_xNb_2O_{15}$): $\langle 100 \rangle$ or $\langle 010 \rangle$ polar axis.

Over 25 different bronze crystal compositions have been grown (as listed in Table I) and in some cases they have been modified to meet the requirements for electro-optic, photorefractive and piezoelectric applications. All of these crystals have been grown by the Czochralski technique.[23-35]

Tungsten bronze crystals are relatively easy to grow compared to most ferroelectric crystals based on perovskite, layered structure $Bi_4Ti_3O_{12}$, and lead germanates, phosphates and vanadates. This is due in part because the bronzes have simple phase transitions and are usually free of 90° and 180° twins which occur in perovskite single crystals. Among the growth problems associated with these crystals, we have found major contributors toward poor crystal quality, as shown in Figure 4:

1. Multicomponent solid solution systems make if difficult to control crystal homogeneity.
2. Exchange among crystallographic sites, specifically of the 15- and 12-fold coordinated ions such as Ba^{2+}, Sr^{2+}, K^+, La^{3+}, causing severe striation problems.
3. High temperature growths (up to 1500°C) cause volatilization and oxidation-reduction (Nb^{5+} to Nb^{4+}) problems.
4. Cracking of crystals when thermally cycling through phase transitions. This is often aggravated by crystal imperfections.

Nevertheless, several bronze compositions have been grown as large size, defect-free crystals, including SBN (>4 cm diameter) and $Ba_{2-x}Sr_xK_{1-y}Na_yNb_5O_{15}$ (>1.5 cm diameter) which have excellent optical quality.

Crystals Exhibiting Strong Transverse Properties (4 mm)

The $Sr_{1-x}Ba_xNb_2O_6$ (SBN) solid solution is the best example of a bronze system with strong transverse properties, including the dielectric constant (ε_{33}) and the
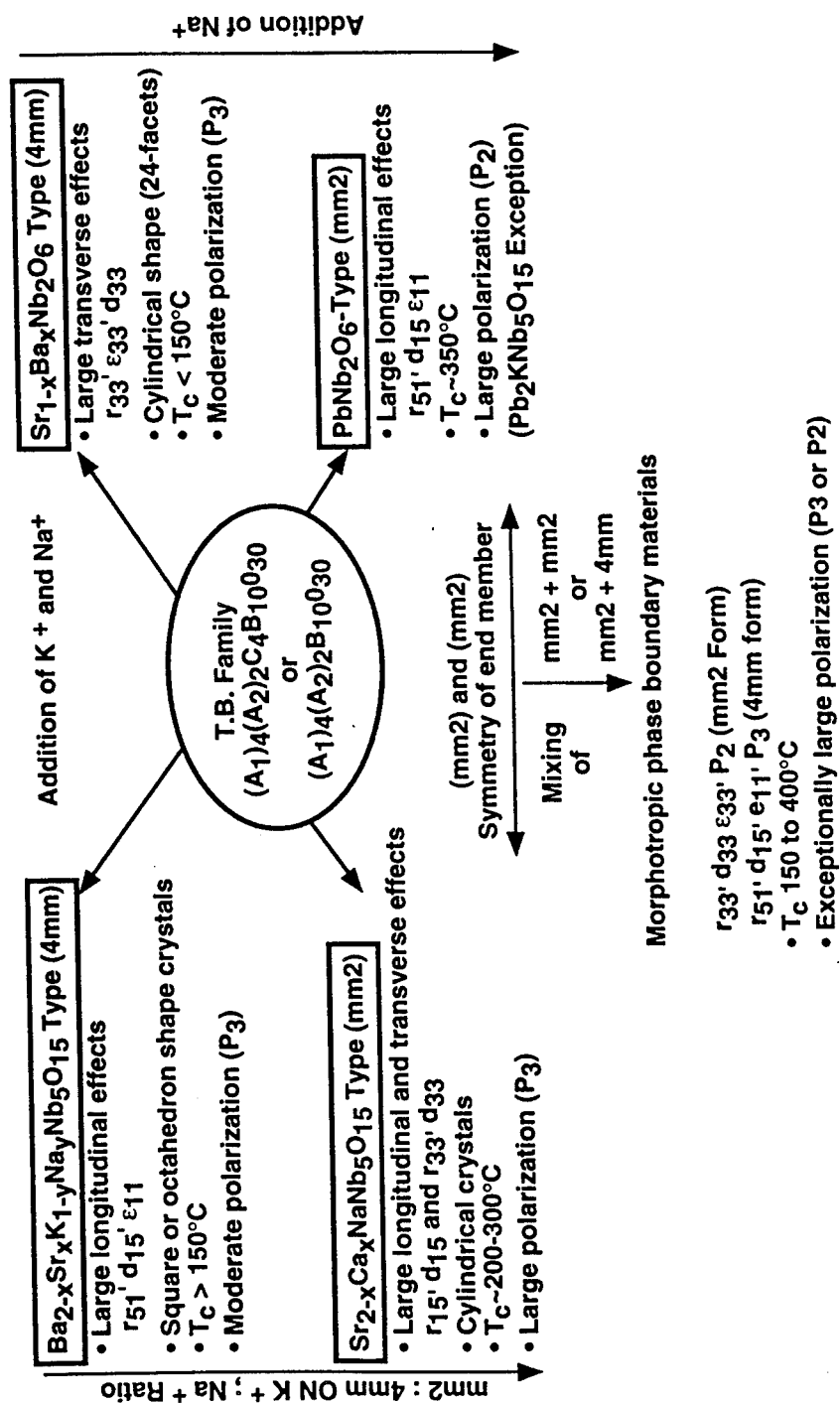
Addition of Na$^+$

Sr$_{1-x}$Ba$_x$Nb$_2$O$_6$ Type (4mm)
- Large transverse effects
  r$_{33}$, ε_{33}, d$_{33}$
- Cylindrical shape (24-facets)
- T$_c$ < 150°C
- Moderate polarization (P$_3$)

PbNb$_2$O$_6$-Type (mm2)
- Large longitudinal effects
  r$_{51}$, d$_{15}$, ε_{11}
- T$_c$ ~350°C
- Large polarization (P$_2$)
  (Pb$_2$KNb$_5$O$_{15}$ Exception)

Addition of K$^+$ and Na$^+$

T.B. Family
(A$_1$)$_4$(A$_2$)$_2$C$_4$B$_{10}$O$_{30}$
or
(A$_1$)$_4$(A$_2$)$_2$B$_{10}$O$_{30}$

(mm2) and (mm2)
Symmetry of end member

Mixing
of

mm2 + mm2
or
mm2 + 4mm

Morphotropic phase boundary materials

r$_{33}$, d$_{33}$ ε_{33}, P$_2$ (mm2 Form)
r$_{51}$, d$_{15}$, ε_{11}, P$_3$ (4mm form)
- T$_c$ 150 to 400°C
- Exceptionally large polarization (P3 or P2)

Ba$_{2-x}$Sr$_x$K$_{1-y}$Na$_y$Nb$_5$O$_{15}$ Type (4mm)
- Large longitudinal effects
  r$_{51}$, d$_{15}$, ε_{11}
- Square or octahedron shape crystals
- T$_c$ > 150°C
- Moderate polarization (P$_3$)

Sr$_{2-x}$Ca$_x$NaNb$_5$O$_{15}$ Type (mm2)
- Large longitudinal and transverse effects
  r$_{15}$, d$_{15}$ and r$_{33}$, d$_{33}$
- Cylindrical crystals
- T$_c$ ~200-300°C
- Large polarization (P$_3$)

mm2 : 4mm ON K$^+$; Na$^+$ Ratio

FIGURE 3   Classification of tungsten bronze family crystals.
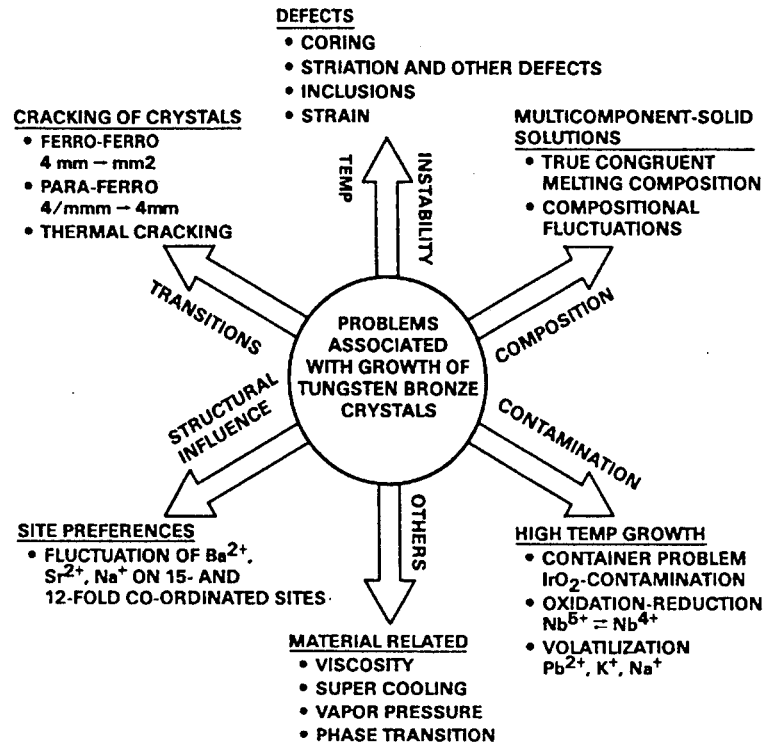
FIGURE 4 Problems associated with the growth of tungsten bronze crystals.

electro-optic (r_{33}) and piezoelectric (d_{33}) coefficients, with the polar axis along $\langle 001 \rangle$. SBN crystal growth has been studied extensively,[36-48] and for optical device applications, both large crystal size and high optical quality are needed. We have been able to grow 4 cm diameter optical-quality SBN crystals (Figure 5) for electro-optic, photorefractive and piezoelectric applications (10–21). The growth of such large crystals requires establishing of the details of the temperature-composition relationship and precise control of the growth conditions.

SBN crystals have a distinct cylindrical growth habit with 24 well-defined facets, each facet corresponding to a definite crystallographic orientation. For this reason, precise orientation and cutting of these crystals is a greatly simplified task. Although SBN crystals are relaxor (frequency-dependent) ferroelectrics with second-order phase transitions,[74] the relaxor behavior becomes even more pronounced as La^{3+} is added (Figure 6). Also of interest is that La^{3+}-doped SBN:60 crystals become square in cross section with increasing La^{3+} concentration up to 1.0 wt%. Optical-quality SBN:50, SBN:60 and SBN:75 crystals have excellent electro-optic, photorefractive and piezoelectric properties and they are currently being used in a number of laboratories for various device studies.

Other examples of bronze ferroelectrics with strong transverse optical properties are $Sr_2KNb_5O_{15}$, $Ba_2KNb_5O_{15}$ and $(Ba, Sr)_6Ti_2Nb_8O_{30}$ (BSTN). We have grown several tetragonal BSTN compositions within the $Ba_6Ti_2Nb_8O_{30}$-$Sr_6Ti_2Nb_8O_{30}$ system which exhibit optical and piezoelectric figures-of-merit about two times

Wafer
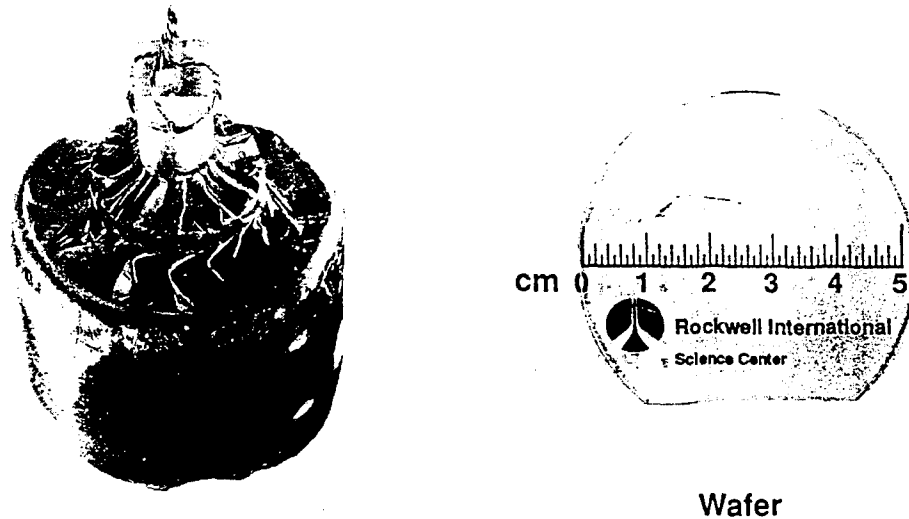
AS grown crystal

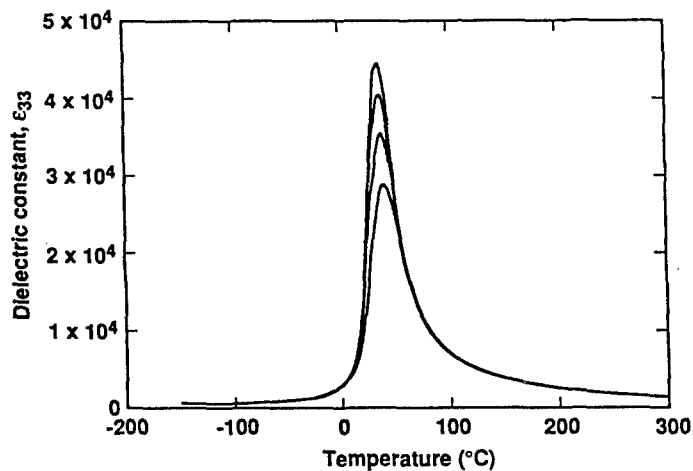FIGURE 5 Large size tungsten bronze SBN single crystal boule grown along ⟨001⟩ by the Czochralski method.

FIGURE 6 Temperature dependence of the polar axis dielectric constant for La^{3+}-doped SBN:60 at 0.1 kHz (upper), 1 kHz, 10 kHz, and 100 kHz (lower).

better than SBN:60. Figure 7 shows a typical BSTN crystal; growth up to 4 cm diameter is currently being attempted.

Crystals Exhibiting Strong Longitudinal Properties (4 mm)

A prototypical member of this class is the $Ba_{2-x}Sr_xK_{1-y}Na_yNb_5O_{15}$ (BSKNN) solid solution, which has large longitudinal properties for K^+-rich compositions. As

- **Crystal diameter:** 1.2 cm

- **Crystal symmetry:** 4 mm

- **Large (r_{33}):**   400 x 10^{-12} m/V

- **Polarization:**   > 34 µC/cm^2

FIGURE 7   Tungsten bronze BSTN crystal boule grown along the (001) direction.

BSKNN-1   **15 x 15 x 8mm**   **BSKNN-2**
                          Cube
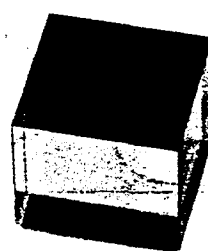
FIGURE 8   Large size tungsten bronze BSKNN single crystal grown along (001).

shown in Figure 8, 1.5 cm diameter BSKNN crystals have been grown in optical quality.[35] The striking differences between BSKNN and SBN crystals are in their growth habits and ferroelectric properties. BSKNN single crystals grow either with a square or octahedral cross section depending on the unit cell dimensions, with the

Longitudinal Effect

BSKNN-2

BSKNN-1

Large longitudinal effects

- Square (4 facet) or octohedron (8 facets) shape
- Large ε_{11}, r_{51}, P_3, d_{15}
- Relaxor
- Low temp T_c expected (4 mm to mm2)
  e.g. BSKNN, KLN, KLNN
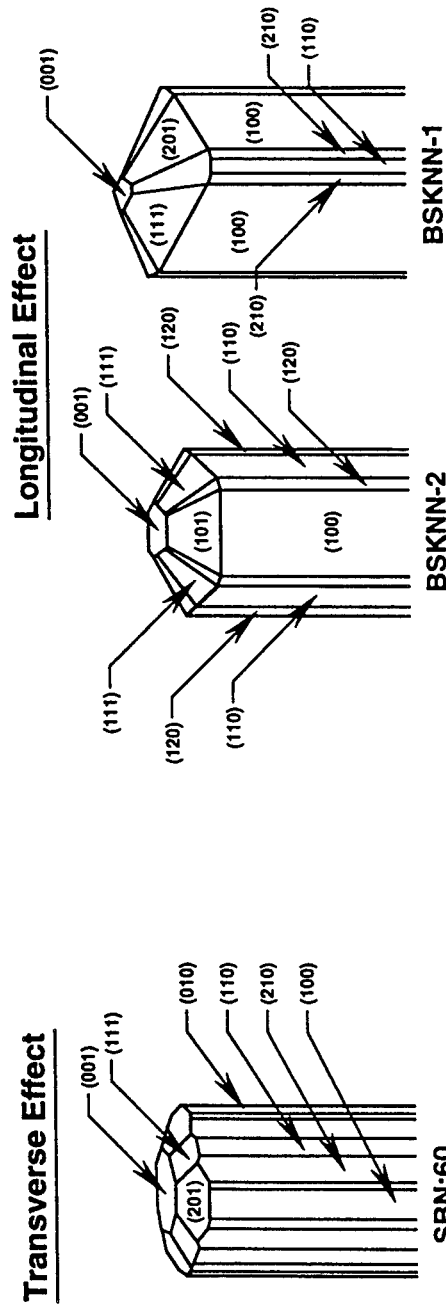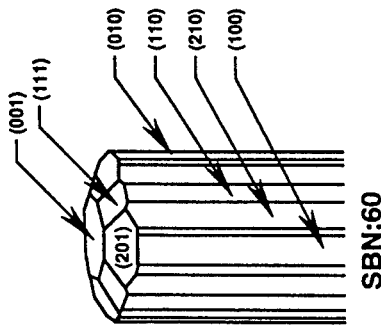
Transverse Effect

SBN:60

Large transverse effects

- Cylindrical shape and 24 facets
- Large ε_3, r_{33}, P_3, d_{33}
- Relaxor
- No low temp transition
  e.g. SBN, SKN, BTN

FIGURE 9   Growth habits for tetragonal tungsten bronze crystals.
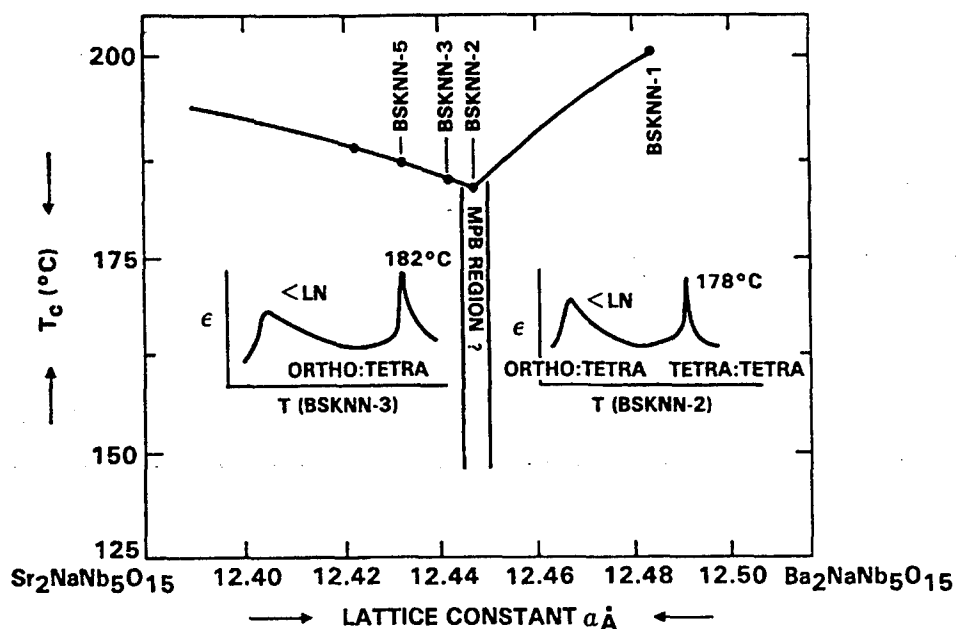
FIGURE 10 The ferroelectric $Sr_2NaNb_5O_{15}$-$Ba_2NaNb_5O_{15}$ system.

bigger unit cell BSKNN crystals ($a > 12.500$ Å, $c > 3.955$ Å) being square in shape. Figure 9 shows the differences among BSKNN-1, BSKNN-2 and SBN-type crystals. We anticipate the presence of a 4 mm to mm2 phase transition in BSKNN-1 (K^+-rich) single crystals, similar to $Ba_2NaNb_5O_{15}$, but this transition would occur below 100K. Xu et al.[49] have claimed such transition and it needs to be verified. The BSKNN compositions that are Na^+-rich (e.g. BSKNN-3, BSKNN-4) appear to be weakly orthorhombic at room temperature. As shown in Figure 10, a morphotropic phase boundary region seems to exist between BSKNN-2 and BSKNN-3, with transverse effects being larger in BSKNN-3.[50] Recently, we have successfully grown BSKNN-3 and BSKNN-5 crystals in excess of 1.5 cm diameter; and we believe we should be able to grow these crystals larger than 3 cm in diameter.

BSKNN crystals have a second-order phase transition with a much less pronounced relaxor character than in SBN. BSKNN crystals resemble $BaTiO_3$ in many of their ferroelectric characteristics, and for this reason we expect that they will replace this well-known material in many electro-optic and photorefractive applications. A particular advantage of BSKNN over $BaTiO_3$ is the absence of twins which makes growth to large sizes (>2 cm diameter) and crystal poling much easier. Other examples of bronzes with strong longitudinal properties are $K_3Li_2Nb_5O_{15}$ and $K_3(Na, Li)_2Nb_5O_{15}$.

Crystal Exhibiting Strong Transverse and Longitudinal Properties

Three types of orthorhombic tungsten bronzes are found in this category (Figure 11): (1) orthorhombic bronzes with the polar axis along $\langle 001 \rangle$ having two phase transitions; (2) bronzes with the polar axis along $\langle 001 \rangle$, but with only one phase
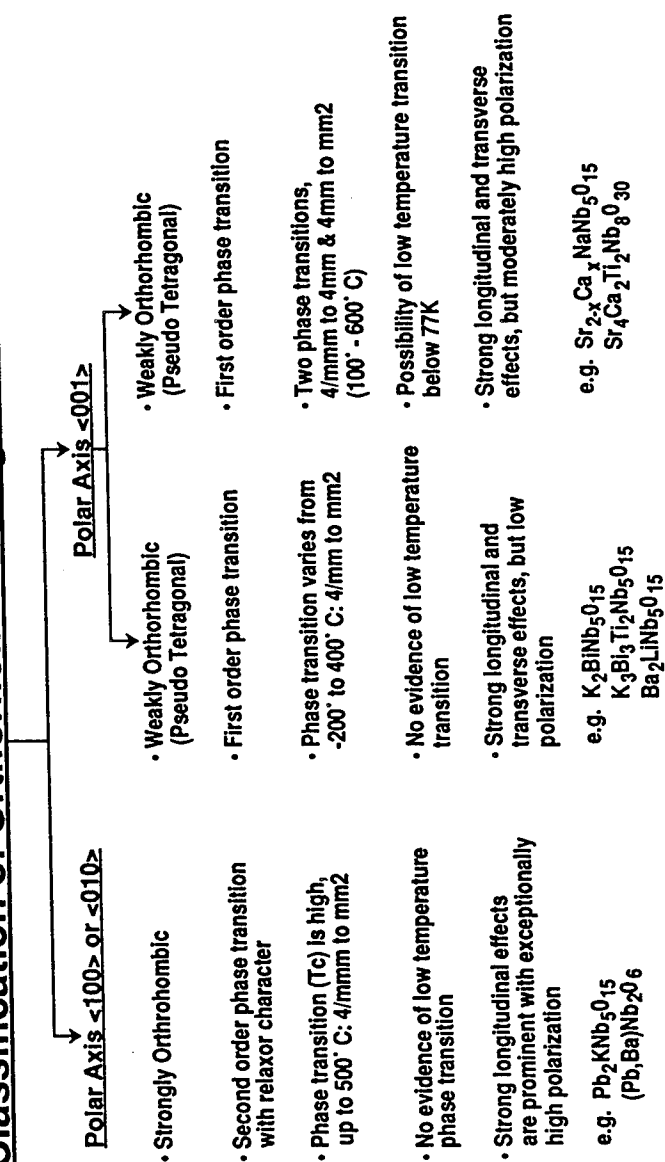
Classification of Orthorhombic Tungsten Bronze Materials

Polar Axis <100> or <010>

- Strongly Orthorhombic

- Second order phase transition with relaxor character

- Phase transition (Tc) is high, up to 500° C: 4/mmm to mm2

- No evidence of low temperature phase transition

- Strong longitudinal effects are prominent with exceptionally high polarization

e.g. $Pb_2KNb_5O_{15}$
$(Pb,Ba)Nb_2O_6$

Polar Axis <001>

- Weakly Orthorhombic (Pseudo Tetragonal)

- First order phase transition

- Phase transition varies from -200° to 400° C: 4/mm to mm2

- No evidence of low temperature transition

- Strong longitudinal and transverse effects, but low polarization

e.g. $K_2BiNb_5O_{15}$
$K_3Bi_3Ti_2Nb_5O_{15}$
$Ba_2LiNb_5O_{15}$

- Weakly Orthorhombic (Pseudo Tetragonal)

- First order phase transition

- Two phase transitions, 4/mmm to 4mm & 4mm to mm2 (100° - 600° C)

- Possibility of low temperature transition below 77K

- Strong longitudinal and transverse effects, but moderately high polarization

e.g. $Sr_{2-x}Ca_x NaNb_5O_{15}$
$Sr_4Ca_2Ti_2Nb_8O_{30}$

FIGURE 11   Classification of orthorhombic tungsten bronze crystals.

transition; and (3) bronzes with the polar axis along $\langle 010 \rangle$ or $\langle 100 \rangle$ and only one phase transition. The latter will be discussed in the next section.

Typical examples of the first type of orthorhombic bronzes are found in the $Sr_{2-x}Ca_xNaNb_5O_{15}$ (SCNN) solid solution system. SCNN crystals have two phase transitions above room temperature,[23] one paraelectric (4/mmm) to ferroelectric (4 mm), and the other ferroelectric (4 mm) to ferroelastic (mm2). As shown in Figure 12, the dielectric constant along $\langle 100 \rangle$ increases with decreasing temperature, resulting in large transverse and longitudinal dielectric and optical properties at room temperature or below. SCNN has a reasonably high spontaneous polarization at room temperature (34 $\mu C/cm^2$) with electro-optic coefficients r_{33} and r_{51} comparable to SBN:75 ($r_{33} = 1400 \times 10^{-12}$ m/V). For this reason, SCNN is being considered for photorefractive applications such as double phase conjugation and optical computing. Other interesting examples of orthorhombic bronzes in this category are $Ba_2NaNb_5O_{15}$ (BNN), $Sr_2NaNb_5O_{15}$ (SNN) and $Sr_2(Na, Li)Nb_5O_{15}$ (SNLN).

$K_2BiNb_5O_{15}$ (KBN) is another crystal in which both longitudinal and transverse ferroelectric properties are large; however, this crystal has only one phase transition (4/mmm to mm2) with no ferroelastic contribution. Crystal growth of KBN is relatively easy compared to SCNN; as shown in Figure 13, approximately 2 cm diameter crystals can be grown with excellent optical quality. $Sr_2(K, Li)Nb_5O_{15}$ (SKLN) is also reported to possess only one phase transition from 4/mmm to mm2.[51] Based on our work on various bronze systems discussed earlier, we believe that this ferroelectric should possess two phase transitions above room temperature, similar to SCNN and BNN. A detailed investigation of SKLN single crystals is still needed to firmly establish the correct structure and transition sequences.

All of these tungsten bronzes are orthorhombic at room temperature and have first-order ferroelectric phase transitions with no relaxor character. BNN single crystals have been studied extensively and they possess excellent acoustical and nonlinear optical properties.[52-57] However, they have not been widely accepted
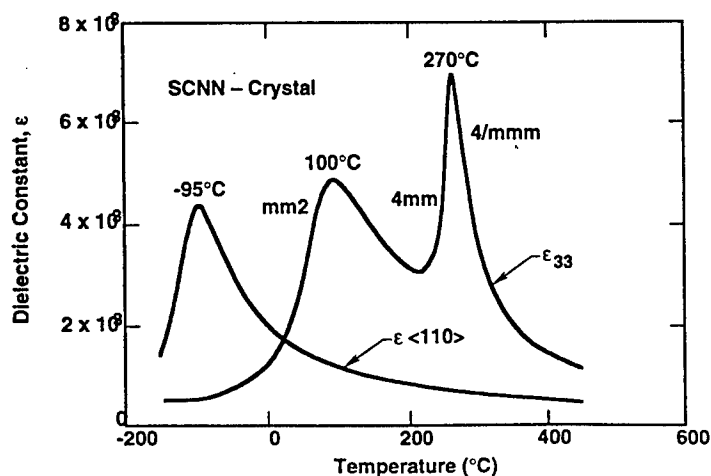

FIGURE 12   Polar and nonpolar $\langle 110 \rangle$ dielectric constants for SCNN at 10 kHz. Low temperature peak along $\langle 110 \rangle$ is due to the freezeout of the polarizability in this direction.

CRYSTAL DIMENSIONS
DIAMETER: 1.5 CM
HEIGHT: 5 CM
QUALITY: EXCELLENT

FIGURE 13 Tungsten bronze orthorhombic $K_2BiNb_5O_{15}$ crystal grown along $\langle 001 \rangle$.

for practical applications due to the difficulties in the growth of large size, adequate quality crystals. At Rockwell, we have also investigated other Bi^{3+}-containing compositions having potentially large r_{33} and r_{51} with photorefractive spectral responses extending into the near-IR (up to 1.0 μm). However, these compositions, except for KBN, are difficult to grow due to the formation of two-phase liquids at the growth temperature.

Pb^{2+}-Containing Bronzes

As summarized in Table II, many of the Pb^{2+} and Ta^{5+}-containing bronze compositions are strongly orthorhombic at room temperature. These materials have only one phase transition from 4/mmm to mm2, with the polar axis oriented along $\langle 100 \rangle$ or $\langle 010 \rangle$. The compositions most studied in this category are $PbNb_2O_6$ (PN), $(Pb, Ba)Nb_2O_6$ (PBN) and $Pb_2KNb_5O_{15}$ (PKN) for surface acoustic wave (SAW) and piezoelectric applications[58-59] because of their excellent electromechanical coupling and piezoelectric properties. The polarization in these materials can exceed 40 μC/cm^2, and their optical figures-of-merit are estimated to be better than the current best-known ferroelectrics such as SBN and $BaTiO_3$. Because of these properties, single crystal and thin film growths of PBN and PKN compositions have been actively pursued in our laboratory and at Penn State University.[60-61] However, bulk crystal growth is extremely difficult due to cracking when passing through the paraelectric/ferroelectric phase transition as a result of the large strain developed in the plane orthogonal to the $\langle 001 \rangle$ growth direction. Another problem with bulk crystal growth is the volatilization of Pb^{2+} at the growth temperature which causes severe compositional inhomogeneity. Hence, the sputtered or sol-gel growth

TABLE II

Symmetry and T_c trends in Nb^{5+} and Ta^{5+}-containing bronzes

Tetragonal bronzes 4/mmm to 4 mm	Orthorhombic bronzes 4/mmm to mm2
• $Pb_2KTa_5O_{15}$ (T_c = -41°C)	• $Pb_2KNb_5O_{15}$ (T_c = 460°C)
• $Pb_2NaTa_5O_{15}$ (T_c = 20°C)	• $Pb_2NaNb_5O_{15}$ (T_c = 560°C)
	• $PbNb_2O_6$ (T_c = 560°C)
• $Sr_2NaTa_5O_{15}$ (T_c = 153°C)	• $Sr_2NaNb_5O_{15}$ (T_c = 270°C)
• $Ba_2NaTa_5O_{15}$ (T_c = 120°C)	• $Ba_2NaNb_5O_{15}$ (T_c = 560°C)
	• $PbTa_2O_6$ (T_c = 265°C)
• $Ba_2KNb_5O_{15}$ (T_c = 373°C)	• $Ba_2KTa_5O_{15}$ (T_c = 10°C)
• $Sr_2KNb_5O_{15}$ (T_c = 156°C)	• $Sr_2KTa_5O_{15}$ (T_c = 110°C)
• $K_3Li_2Nb_5O_{15}$ (T_c = 450°C)	• $K_3Li_2Ta_5O_{15}$ (T_c = -266°C)

of epitaxial thin films appears to be the best growth method for these ferroelectrics, especially for electronic memory and optical applications.

Table II shows that when Pb^{2+} is combined with Nb^{5+}, the compounds crystallize with an orthorhombic symmetry; however, a tetragonal (4 mm) structure can be stabilized when Pb^{2+} is combined with Ta^{5+}, with the exception of $PbTa_2O_6$ (PT) which is orthorhombic at room temperature with a Curie point of 260°C. The situation is reversed for non-Pb^{2+}-containing bronzes, however. For example, when Ba^{2+} and Sr^{2+} are combined with K^+ and Nb^{5+}, the phases are tetragonal, and when they are combined with K^+ and Ta^{5+}, the phases are orthorhombic. Since only a few of the Ta^{5+}-containing bronzes are ferroelectric above room temperature, and these compositions melt at very high temperatures (>1600°C), very few Ta^{5+}-containing bronze crystals have been grown to date. As a result, the Ta^{5+}-containing bronzes are not yet well understood.

Photorefractive Applications of T. B. Crystals

We are exploring tungsten bronze family materials in single crystal and thin film forms for various applications, including photorefractive, electro-optic, piezoelectric, pyroelectric devices. The unusually strong linear and nonlinear effects in these materials make them excellent candidates for such applications. Photorefractive applications are of current great interest, and we have grown several optical-quality bronzes that possess high photorefractive figures-of-merit. Table III lists some of the photorefractive bronze crystals with their key optical figures of merit.

The improved sensitivity and photorefractive response time exhibited in large-size, high optical quality single crystals of SBN and BSKNN have made possible the demonstration of a number of applications. Beam fanning[62] is a well-known photorefractive phenomenon in which scattered light from a laser beam is asymmetrically amplified as it passes through high-gain crystals such as SBN and BSKNN. Beam fanning gives rise to a number of possible applications and plays an auxiliary

TABLE III

Electro-optic coefficients and figures of merit for tungsten bronzes

Crystal	Electro-Optic Coeff. ($r_{ij} \times 10^{-12}$ m/V)	ε_{ij}	$n^3 r_{ij}/\varepsilon$	Crystal Size (cm.)
SBN:60	$r_{33} = 240$	$\varepsilon_{33} = 1000$	5.01	> 5.0
BSTN	$r_{33} = 200$	$\varepsilon_{33} = 345$	8.05	> 1.5
BSKNN-2	$r_{51} = 380$	$\varepsilon_{11} = 800$	6.2	> 1.8
BSKNN-3	$r_{51} = 420$	$\varepsilon_{11} = 800$	6.4	> 1.5
SCNN	$r_{33} = 1200$	$\varepsilon_{33} = 1740$	8.63	~ 1.0
	$r_{51} = 1150$	$\varepsilon_{11} = 1700$	8.32	

role in the formation of self-pumped phase conjugators[63] and double phase conjugators.[64] In particular, the photorefractive processes of beam-fanning, self-pumped phase conjugation and double phase conjugation have been used to demonstrate several important beam control and image processing applications. For example, techniques for using tungsten bronze materials to perform optical limiting,[65,66] imaging restoration (beam clean-up),[67] incoherent-to-coherent conversion,[68] real-time volume storage of color images,[69] addition/subtraction,[70] and correlation-convolution operations[71] have been developed. We also recently demonstrated that beam fanning, self-pumped phase conjugation and double phase conjugation can be performed in color (i.e., using many mutually incoherent laser wavelengths), thereby expanding the range and variety of applications possible in these crystals.[69,71]

In addition to high gain and fast response, a photorefractive crystal must have good optical quality (free of index variations), and in many cases, must be of a large size to be used successfully. For example, when two-wave mixing is used to amplify images, severe phase aberrations may be introduced by the photorefractive gain medium unless the medium is free from all index variations and the surfaces are prepared very carefully. High optical quality crystals will allow image amplification without having to resort to phase conjugation to clean-up the images.

We recently demonstrated the principle of incoherent-to-coherent conversion using a self-pumped phase conjugator based on SBN:60 crystals.[68] The self-pumped phase conjugator[63] used in these experiments required only one input wave. In this geometry the incident input wave is reflected from self-generated gratings in the crystal to form the pumping beams. The experimental set up is shown in Figure 14 where an extraordinary polarized beam at 514 nm from an argon-ion laser was used to generate a phase conjugate replica of the input wave. A counterpropagating beam, consisting of a white light source, was passed through a binary transparency and imaged into the crystal to form image-modulated volume phase gratings. The selective erasure of the self-organized gratings written by the self-pumping beam encoded the amplitude information from the incoherent beam onto the phase conjugate signal. The inverted-contrast coherent output image is compared with the input image in Figure 15. The resolution for this set of images is 28 lines/mm.
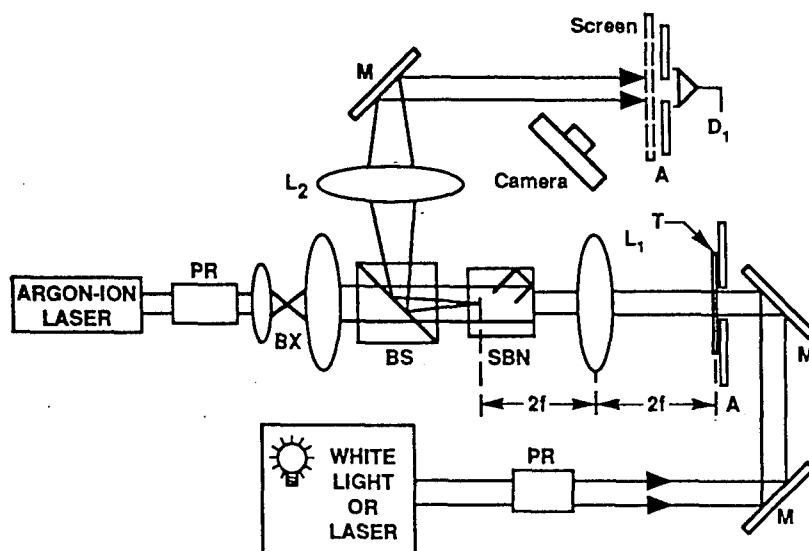
FIGURE 14 Experimental arrangement used to demonstrate the principles of incoherent-to-coherent conversion in a self-pumped phase conjugator.

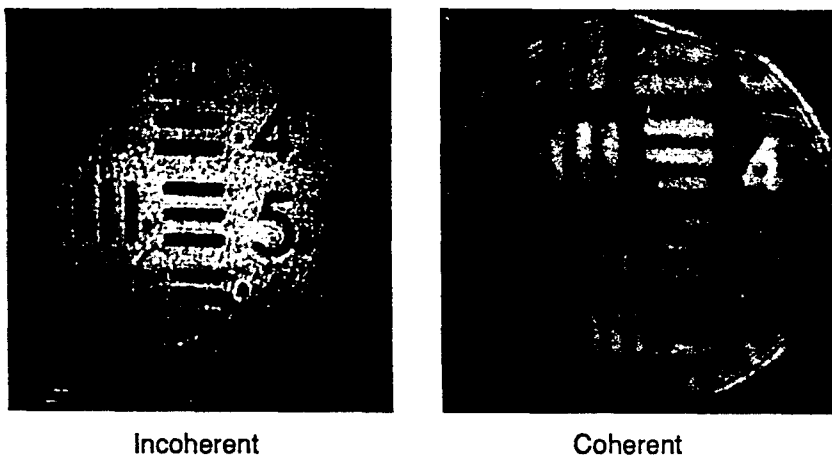Incoherent   Coherent

FIGURE 15 Comparison of the reversed contrast incoherent input image and the coherent output image.

We note that, since any aberration introduced on the writing beam by the crystal would also be transferred to the signal beam, this high resolution is due in part to the high optical quality of the crystal used.

A recent development in phase conjugation techniques has been the double phase conjugate mirror (DPCM),[64,70,73] where the photorefractive crystal acts as a simultaneous conjugate mirror for two incoming waves. When the output of two independent lasers with incident optical electromagnetic fields E_1 and E_2 are directed into a photorefractive medium, a phase conjugate replica of each beam appears under appropriate conditions. Both beams are required for either conjugate
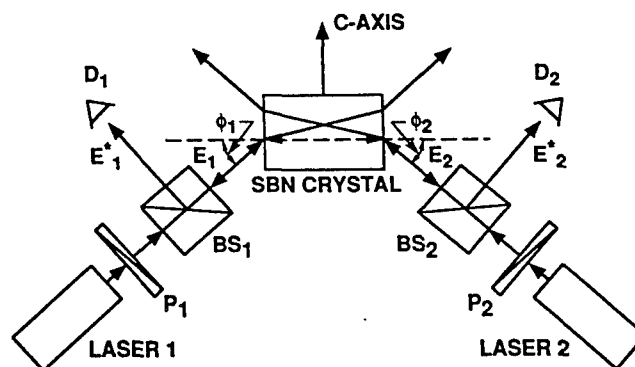
FIGURE 16   Experimental apparatus used to observe the phase conjugate signals from a double phase conjugate mirror based on a single crystal of SBN:60.

beam (E_1^* or E_2^*) to exist, and the energy for the conjugate of one beam is supplied by the other beam. Although DCPMs have many different configurations, significant benefits can be derived from specific geometric arrangements. For example, both the time response and magnitude of the conjugate signal will vary significantly depending on which geometry is employed for a particular crystal. Recently, we reported[70] on a new method for double phase conjugation which is particularly suited to tungsten bronze SBN, although the method has also been applied to $BaTiO_3$ and BSKNN. This new arrangement is highly insensitive to the alignment of the incident beams, quick to form a conjugate image with high reflectivity and fidelity, and free from instabilities due to frequency shifts or competition with self-pumping. The geometry for this new DPCM is depicted in Figure 16 where the two input beams have "fanned" into one another to form the coupling region observed in the crystal after the conjugate waves appear. Since the two beams bridge to overlap in the crystal without reflecting off a crystal face, this arrangement is called the "bridge conjugator." The bridge conjugator shown in Figure 16 was used to demonstrate image addition/subtraction[70] and more recently correlation-convolution.[71]

When the output of a linearly polarized argon-ion laser oscillating at eight discrete lines simultaneously is directed onto an SBN or BSKNN crystal at an angle Θ with the normal to the entrance crystal face, a broad fan of linearly polarized light appears on the negative c-axis side of the transmitted beam. This fan appears independent of whether Θ is positive or negative as defined by the c direction. For negative Θ values, however, an intense multicolored ring or rainbow pattern also appears.[72] Examination of the rainbow pattern using a spectrometer indicates that all eight lines are present, although only four or five of them are discernible to the eye. In fact, reflection of the multicolored ring back into the crystal using a curved mirror produced the phase conjugate of all eight lines in a time very near to the crystal beam-fanning response time.[69] In this sense, the crystal acts as a broadband "self-pumping" device.[74] Tungsten bronze crystals are particularly suited for broadband applications because their open crystal structure makes possible multi-dopant concepts which broaden the photorefractive absorption spectrum without degrading the optical quality. We have used the effect of multicolor beam fanning to overcome

the earlier difficulty of erasure between colors when a multi-wavelength source is used to demonstrate real-time volume storage of color images.

In addition to those applications discussed here, other important image processing applications will continue to be improved and developed as the quality of photorefractive crystals continues to improve.

CONCLUSIONS AND REMARKS

A variety of ferroelectric tungsten bronze crystals have been successfully grown, and using their ferroelectric and electro-optic properties, this family of materials can be classified into four different groups. The doped tungsten bronze crystals specifically SBN and BSKNN, exhibit interesting photorefractive properties and have a wide range of applications in incoherent-to-coherent conversion, double phase conjugate mirrors, image processing, data storage and optical computing.

ACKNOWLEDGEMENTS

REFERENCES

1. R. B. Maciolek and S. T. Liu, *J. Electron. Mater.*, **2**, 191 (1973).
2. R. B. Maciolek, T. L. Schuller and S. T. Liu, *J. Electron. Mater.*, **5**, 415 (1976).
3. S. Kuroda and K. Kubota, *J. Phys. Chem. Solids*, **44**, 527 (1983).
4. E. G. Spencer, P. V. Lenzo, and A. A. Ballman, *Proc. IIIE*, **52**, 2074 (1967).
5. A. M. Glass, *J. Appl. Phys.*, **40**, 4699 (1969).
6. P. V. Lenzo, E. G. Spencer and A. A. Ballman, *Appl. Phys. Lett.*, **11**, 23 (1967).
7. R. L. Townsend and J. T. LaMacchia, *J. Appl. Phys.*, **51**, 88 (1970).
8. J. J. Amodei, D. L. Staebler and A. W. Stephens, *Appl. Phys. Lett.*, **18**, 507 (1971).
9. J. B. Thaxter, *Appl. Phys. Lett.*, **15**, 210 (1969).
10. W. W. Ho, W. F. Hall, R. R. Neurgaonkar, R. E. DeWames and T. C. Lim, *Ferroelectrics*, **38**, 63 (1981).
11. G. Rakuljic, A. Yariv and R. R. Neurgaonkar, *J. Opt. Eng.*, **25**, 1212 (1986).
12. O. Eknoyan, C. H. Bulmer, H. F. Taylor, W. K. Burns, A. S. Greenblatt, L. A. Beach and R. R. Neurgaonkar, *Appl. Phys. Lett.*, **48**, 13 (1986).
13. M. D. Ewbank, R. R. Neurgaonkar, W. K. Cory and J. Feinberg, *Appl. Phys. Lett.*, **62**(2), 373 (1987).
14. B. Bobbs, M. Matloubian, H. R. Fetterman, R. R. Neurgaonkar and W. K. Cory, *Appl. Phys. Lett.*, **48**, 1642 (1986).
15. E. J. Sharp, M. J. Miller, G. L. Wood, W. W. Clark III, G. Salamo and R. R. Neurgaonkar, *Appl. Phys. Lett.*, **52**, 765 (1987).
16. G. L. Wood, W. W. Clark III, M. J. Miller, E. J. Sharp, G. Salamo and R. R. Neurgaonkar, *J. Quantum Electronics*, **23**(12), 2126 (1987).
17. J. F. Jelsma, R. R. Neurgaonkar and W. K. Cory, *Proc. SPIE*, **832**, 198 (1987).
18. G. J. Salamo, M. J. Miller, W. W. Clark III, G. L. Wood, E. J. Sharp and R. R. Neurgaonkar, *Appl. Optics*, **27**(21), 4356 (1988).
19. E. J. Sharp, M. J. Miller, G. J. Salamo, W. W. Clark III, G. L. Wood and R. R. Neurgaonkar, *Ferroelectrics*, **87**, 335 (1988).

20. K. Sayano, G. A. Rakuljic, A. Agranat, A. Yariv and R. R. Neurgaonkar, *Optics. Lett.*, **14**(9), 459 (1989).
22. J. Ford, Y. Taketomi, S. Lee, D. Bize, S. Feinman and R. R. Neurgaonkar, *Proc. SPIE*, **1148**, 12 (1989).
23. R. R. Neurgeonkar, W. K. Cory, J. R. Oliver, E. J. Sharp, G. L. Wood, M. S. Miller, W. W. Clark III and G. Salamo. *Mat. Res. Bull.*, **23**, 1459 (1988).
24. R. R. Neurgaonkar, J. G. Nelson, J. R. Oliver and L. E. Cross, *Mat. Res. Bull.*, **25**, 959 (1990).
25. R. R. Neurgaonkar, J. R. Oliver and J. G. Nelson, private communication.
26. R. R. Neurgaonkar, M. H. Kalisher, T. C. Lim, E. J. Staples and K. L. Keester, *Mat. Res. Bull.*, **15**, 1305 (1980).
27. R. R. Neurgaonkar, W. K. Cory, W. W. Ho, W. F. Hall and L. E. Cross, *Ferroelectrics*, **38**, 857 (1981).
28. R. R. Neurgaonkar and W. K. Cory, *Ferroelectrics*, **35**, 301 (1983).
29. R. R. Neurgaonkar, W. W. Ho, W. K. Cory, W. F. Hall and L. E. Cross, *Ferroelectrics*, **51**, 185 (1984).
30. R. R. Neurgaonkar, *Proc. SPIE*, **465**, 97 (1984).
31. R. R. Neurgaonkar and L. E. Cross, *Mat. Res. Bull.*, **21**, 893 (1986).
32. R. R. Neurgaonkar and W. K. Cory, *J. Opt. Soc. Am.*, **3**(B), 276 (1986).
33. R. R. Neurgaonkar, W. K. Cory, J. R. Oliver and L. E. Cross, *Proc. SPIE*, **567**, 11 (1985).
34. R. R. Neurgaonkar, W. K. Cory, J. R. Oliver and L. E. Cross, *Mat. Res. Bull.*, **24**, 1025 (1989).
35. R. R. Neurgaonkar, W. K. Cory, J. R. Oliver, M. J. Miller, W. W. Clark III, G. L. Wood and E. J. Sharp, *J. Cryst. Growth*, **84**, 629 (1987).
36. R. R. Neurgaonkar, W. K. Cory and J. R. Oliver, *Proc. SPIE*, **739**, 91 (1987).
37. R. R. Neurgaonkar, W. K. Cory, J. R. Oliver, M. D. Ewbank and W. F. Hall, *J. Opt. Eng.*, **26**(5), 392 (1987).
38. M. H. Francombe and B. Lewis, *Acta Cryst.*, **11**, 696 (1958).
39. L. G. Van Uitert, H. J. Levinstein, J. J. Rubin, C. D. Capio, E. F. Dearborn and W. A. Bonner, *Mat. Res. Bull.*, **3**, 47 (1968).
40. P. B. Jamieson, S. C. Abrahams and J. L. Bernstein, *J. Chem. Phys.*, **48**, 5048 (1968).
41. T. Fukuda, *Jap. J. Appl. Phys.*, **9**, 599 (1970).
42. T. V. Tiaou, N. N. Krainnik, I. H. Ismailzade, V. A. Isupov and F. A. Ageve, Izv. Acad. Nauk. SSSR, *Ser. Phys.*, **35**, 1825 (1971).
43. M. H. Framcombe, *Acta Cryst.*, **13**, 131 (1960).
44. V. A. Isupov and V. I. Kosiakov, *Zh. Tekh. Fiz.*, **28**, 2175 (1958).
45. J. R. Oliver, R. R. Neurgaonkar and L. E. Cross, *J. Am. Ceram. Soc.*, **72**, 202 (1989).
46. A. A. Ballman, S. K. Kurtz and H. Brown, *J. Cryst. Growth*, **10**, 185 (1971).
47. A. A. Ballman and H. Brown, *J. Cryst. Growth*, **1**, 311 (1967).
48. K. Megumi, N. Nagatsuma, K. Kashiwada and Y. Furuhata, *Mater. Sci.* **11**, 1583 (1976).
49. H. C. Chen and Y. Xu, *J. of Chinese Silicate Soc.*, **10**, 406 (1982).
50. R. R. Neurgaonkar, W. K. Cory, J. R. Oliver, M. Khoshnevisan and E. J. Sharp, *Ferroelectrics*, **102**, 3 (1990).
51. I. Katahiro, T. Yano and A. Watanabe, *Jap. J. Appl. Phys.*, **54**, 2355 (1971).
52. J. E. Geusic, *Appl. Phys. Lett.*, **11**(9), 269 (1967).
53. J. E. Geusic, *Appl. Phys. Lett.*, **12**(9), 306 (1968).
54. R. R. Rice, *J. Electrochem. Soc.*, **116**(6), 839 (1969).
55. R. G. Smith, *Appl. Phys. Lett.*, **39**(8), 4030 (1968).
56. A. W. Warner, *Appl. Phys. Lett.*, **14**(1), 34 (1969).
57. B. Jaffe, W. R. Cook and H. Jaffe, *Piezoelectric Ceramics*, (Academic, New York), 1971.
58. M. Yokosuka, *Jap. J. Appl. Phys.*, **16**, 379 (1977).
59. K. Nagata and K. Okazaki, *Jap. J. Appl. Phys.*, **24**, 812 (1985).
60. T. R. Shrout, H. Chen and L. E. Cross, *Ferroelectrics*, **56**, 45 (1983).
61. T. R. Shrout, L. E. Cross and D. A. Hukin, *Ferroelectrics Lett.*, **44**, 325 (1983).
62. J. Feinberg, *J. Opt. Soc. Am.*, **72**, 46 (1982).
63. J. Feinberg, *Opt. Lett.*, **7**, 486 (1982).
64. S. Weiss, S. Sternkler and B. Fischer, *Opt. Lett.*, **12**, 114 (1987).
65. G. L. Wood, W. W. Clark III, M. J. Miller, G. J. Salamo and E. J. Sharp, Mat. For Opt. Switches, Isolators and Limiters, M. J. Soileau, ed., *SPIE*, **1105**, 154 (1989).
66. G. L. Wood, W. W. Clark III, G. J. Salamo, A. Mott and E. J. Sharp, *J. Appl. Phys.*, **71**, 37 (1992).
67. E. J. Sharp, M. J. Miller, G. J. Salamo, W. W. Clark III, G. L. Wood and R. R. Neurgaonkar, *Ferroelectrics*, **87**, 335 (1988).
68. E. J. Sharp, G. L. Wood, W. W. Clark III, G. J. Salamo and R. R. Neurgaonkar, *Opt. Lett.*, **17**, 207 (1992).

69. S. G. Rabbani, J. L. Shultz, G. J. Salamo, E. J. Sharp, W. W. Clark III, M. J. Miller, G. L. Wood and R. R. Neurgaonkar, *Appl. Phys.*, **B53**, 323 (1991).
70. E. J. Sharp, W. W. Clark III, M. J. Miller, G. L. Wood, B. Monson, G. J. Salamo and R. R. Neurgaonkar, *Appl. Opt.*, **29**, 743 (1990).
71. R. J. Anderson, E. J. Sharp, G. L. Wood, W. W. Clark III, G. J. Salamo and R. R. Neurgaonkar, Paper ThC2, 1992 Annual OSA Meeting, Sept. 24, 1992.
72. G. J. Salamo, M. J. Miller, W. W. Clark III, G. L. Wood, E. J. Sharp and R. R. Neurgaonkar, *Appl. Opt.*, **27**, 4356 (1988).
73. P. Yeh, T. Y. Chang and M. D. Ewbank, *J. Opt. Soc. Am*, **B5**, 1743 (1988).
74. M. Cronin-Golamb, S. Kwong and A. Yariv, *Appl. Phys. Lett.*, **44**, 727 (1984).

Cr^{3+}-$Sr_{0.6}Ba_{0.4}Nb_2O_6$ SINGLE CRYSTALS FOR
PHOTOREFRACTIVE APPLICATIONS

R.R. Neurgaonkar, W.K. Cory and J.R. Oliver
Rockwell International Science Center
1049 Camino Dos Rios
Thousand Oaks, CA 91360

and

E.J. Sharp, M.J. Miller, W.W. Clark, III, G.L. Wood and G.J. Salamo
Center for Night Vision and Electro-Optics
Fort Belvoir, VA 22060-5677

ABSTRACT: Optical quality Cr^{3+}-doped $Sr_{0.6}Ba_{0.4}Nb_2O_6$ (SBN:60) single crystals
have been grown by the Czochralski technique with boules as large as
2 cm in diameter and 5 cm long being grown. The doping of 0.01 wt%
Cr^{3+} on the 6-fold coordinated Nb^{5+} site increases the dielectric
constant approximately 15% and reduces the phase transition tem-
perature from 75° to 72°C. Photorefractive fanning measurements
show a response time of 0.9 s at 40 mW/cm², a value nearly three
times faster than found in Ce^{3+}-doped SBN:60 crystals.

MATERIALS INDEX: tungsten, bronze, strontium, barium,
chromium, niobates

INTRODUCTION

The photorefractive properties of ferroelectric single crystals such as $BaTiO_3$
and tungsten bronze SBN:60 are of great interest because of their potential for applica-

tions in optical computing, image processing, phase conjugation and laser hardening. Recent studies indicate that Ce^{3+}-doped SBN:60 has a photorefractive gain and time of response comparable to $BaTiO_3$ (1-8). In our recent work, we have measured gains as high as 45 cm^{-1} and response times as fast as 10-40 ms, depending upon the laser intensity, for Ce^{3+}-doped SBN:60 single crystals. Further improvements, specifically in the speed of response, are still desirable in most applications, and for this reason we have recently undertaken the study of other dopants such as Fe^{2+}/Fe^{3+}, Cr^{3+} and $Cr^{3+} + Ce^{3+}$ in SBN:60. This paper reports the growth of Cr^{3+}-doped SBN:60 single crystals and their major ferroelectric and photorefractive properties.

EXPERIMENTAL

The selected $Sr_{0.6}Ba_{0.4}Nb_2O_6$ (SBN:60) composition exists on the $SrNb_2O_6$-$BaNb_2O_6$ system in which a complete solid solution has been reported between these two end members (10). However, the ferroelectric tungsten bronze (4mm) solid solution, $Sr_{1-x}Ba_xNb_2O_6$, occurs for $0.25 \le x \le 0.75$, with SBN:60 being the congruent melting composition (11). For this reason, we selected this composition for this work, with crystals being grown using ultrapure $BaCO_3$, $SrCO_3$, Nb_2O_5 and Cr_2O_3 starting materials. These materials were batched in the appropriate ratios and thoroughly mixed before sintering at 1350°C. The sintered powders were then melted in a platinum crucible (2 in. in both diameter and height) supported by a fibrous alumina insulating jacket. The Czochralski furnace was rf induction-heated at 370 KHz, and utilized automatic crystal diameter control. All crystals were cooled through their paraelectric/ferroelectric phase transition in an after-heater furnace. Further information on SBN crystal growths can be found in earlier papers (1,2,12-14).

A variety of techniques were used to evaluate the ferroelectric and optical properties of these crystals. Prior to measurement, the crystals were poled by a field-cooling method (T_c to room temperature) under a dc field of 5-10 kV/cm along the polar (001) axis using either Au or Pt electrodes. The completeness of poling was checked by measuring the dielectric cunsant before and after poling.

RESULTS AND DISCUSSION

SBN:60 single crystals were doped with chromium at concentrations of 0.011 and 0.016 wt%. For these additions, we did not notice any major changes in the growth conditions adopted for undoped SBN:60 single crystals (12,13). The growth of Cr^{3+}-doped crystals proceeded without undue difficulties under the following conditions:

1. Melting Temperature: 1485°C
2. Pulling Direction: (001) axis
3. Crystal Rotation Rate: 10-25 rpm
4. Crystal Pulling Rate: 6-10 mm/h
5. Growth Atmosphere: Oxygen

Initially, undoped SBN:60 crystal seeds of optical quality were used for these growths. As Cr^{3+}-doped crystal seeds became available, they were used in subsequent experiments to maintain a uniform Cr^{3+} concentration in both the crystals and the melt. As shown in Fig. 1, crystals as large as 2 cm diameter and 5 cm long have now

FIG. 1 Cr^{3+}-doped $Sr_{0.6}Ba_{0.4}Nb_2O_6$ (SBN:60) crystal.

been grown along the (001) direction. Growths along other orientations, e.g., (100) and (110), were also attempted, but these did not yield crystals of sufficient size or quality. For this reason, all succeeding growths were performed only along the (001) direction (3,4).

        Cr^{3+}-doped SBN:60 single crystal boules show a yellowish-green color with 24 well-defined facets, a unique feature of these solid solution crystals (1,2,15). The color becomes more greenish as the Cr^{3+} concentration is increased. SBN solid solution crystals are represented by the chemical formula $(A_1)_4(A_2)_2B_{10}O_{30}$, where A_1, A_2 and B are in 15-, 12- and 6-fold coordinated lattice sites, respectively. Cr^{3+} occupies the 6-fold coordinated Nb^{5+} site. Based on work on ceramic samples, we have found that Cr solid solubility is surprisingly high (15 mole% or more) even though the charge difference between Nb^{5+} and Cr^{3+} is not balanced.

        The quality of these Cr-doped crystals is generally excellent for photorefractive applications. Prior to this work, we also investigated the growth of SBN:60 single crystals doped with Fe^{3+}, with crystals as large as 2 cm diameter being grown without any problems (1,2). The Fe^{2+}/Fe^{3+} ions are known to be active photorefractive species in other ferroelectric hosts such as $BaTiO_3$, $KNbO_3$, $LiNbO_3$ and $Ba_2NaNb_5O_{15}$ (16-19); however, the addition of Fe^{3+} in SBN:60 resulted in degraded optical quality due to severe striations. Since both Cr^{3+} and Fe^{3+} have similar ionic size, valence states and site occupancy in the tungsten bronze structure, one would expect to achieve similar results in crystal optical quality for these two dopants. Efforts are underway to distinguish the differences arising from these ions, so that the origin of striations in Fe-doped crystals can be better understood.

        Cr^{3+}-doped SBN:60 single crystals possess ferroelectric properties similar to undoped crystals, but with slightly lower phase transition (Curie) temperature. A reduction in T_c of approximately 3°C has been observed for a 0.011 wt% addition of Cr^{3+}. A similar trend has also been observed for Fe^{3+}, Ti^{4+} and $(Ti^{4+} + W^{6+})$-doped SBN:60 compositions. All of these dopants prefer the 6-fold coordinated Nb^{5+} site in the bronze structure. However, their effects on photorefractive properties depend upon

the electronic structure of each dopant. Since the addition of $(Ti^{4+} + W^{6+})$ in orthorhombic tungsten bronze $PbNb_2O_6$ raises T_c and increases the piezoelectric coefficients, we had expected that T_c would rise for Ti^{4+}-doped SBN:60, something which was not observed. A more detailed investigation on this dopant is in progress and will be discussed in a future publications.

The room temperature c-axis dielectric constant of Cr-doped SBN:60 is around 1100. This is 10-15% higher than in undoped SBN:60 crystals and is due to a slight drop in T_c and a somewhat shallower slope of the dielectric constant below T_c. In contrast, the a-axis dielectric constant of 485 is virtually unchanged from that found in undoped SBN:60. The spontaneous polarization, P_s, was determined using P vs E hysteresis loop measurements and integrated pyroelectric current measurements as a function of temperature. Both methods yielded a value of P_s = 29 ± 0.5 coul/cm² at 20°C, comparable to that found in undoped crystals. The static coercive (switching) field is 2.1 kV/cm; this value can be expected to increase at nonzero frequencies due to the long time constant for domain reversal (approximately 1 min) at this applied field.

The room-temperature dielectric losses in poled Cr^{3+}-doped SBN:60 crystals are tan $\delta \leq 0.01$ from 100 Hz - 100 KHz, with vanishingly low dc conductivities of 10^{-14} Ω^{-1}-cm^{-1} or less. At high temperatures ($\geq 350°C$), the dc conductivity has a thermal activation energy of approximately 1.6 eV, indicating that the equilibrium Fermi level is pinned near mid-gap as in the case of undoped SBN:60. The similarity in the dc conductivities of undoped and Cr^{3+}-doped SBN:60 suggests that electron donor levels introduced by doping are closely compensated by additional acceptor levels, so that the overall donor/acceptor ratio, N_D/N_A, remains essentially unchanged.

We have carried out preliminary experiments on the photorefractive behavior of an optically polished Cr^{3+}-doped SBN:60 crystal. The transmission spectrum of this crystal, along with that of Ce^{3+}-doped SBN:60 crystals, is given in Fig. 2. As can be seen from the transmission spectra, Cr^{3+}-doped SBN:60 has an increased red response compared to either the undoped or Ce^{3+}-doped crystals. Based on this difference in spectral behavior, Cr^{3+}-doped SBN:60 thus has potential for use as a photorefractive material at laser diode wavelengths. In general, the photorefractive response of these materials shifts toward the near infrared as the coordination site of the dopant is lowered from the 12-fold site. For example, the spectrum of the Ce^{3+}-doped sample in Fig. 2 is typically observed when Ce^{3+} occupies the 12-fold coordinated site. When Ce^{3+} is placed in the 9-fold coordinated site, the spectral response extends to longer wavelengths (3,20), as in the case here for 6-fold coordinated Cr^{3+}.

We have measured the e^{-1} response time for beam fanning (21) using a HeCd laser operating at 440 nm with a beam diameter of 1.4 mm. These results are given in Table 1 along with a summary of the ferroelectric properties for undoped, Ce^{3+}-doped, and Cr^{3+}-doped SBN:60. For similar dopant concentrations, the Cr^{3+}-doped SBN:60 crystal was substantially faster than either the undoped or the Ce^{3+}-doped crystals. In addition, the Cr^{3+}-doped crystal was also found to be faster than a $BaTiO_3$ crystal measured under the same experimental conditions. However, neither the dopant species nor concentration was known for the $BaTiO_3$ sample, although it displayed a behavior typical to reports in the literature.

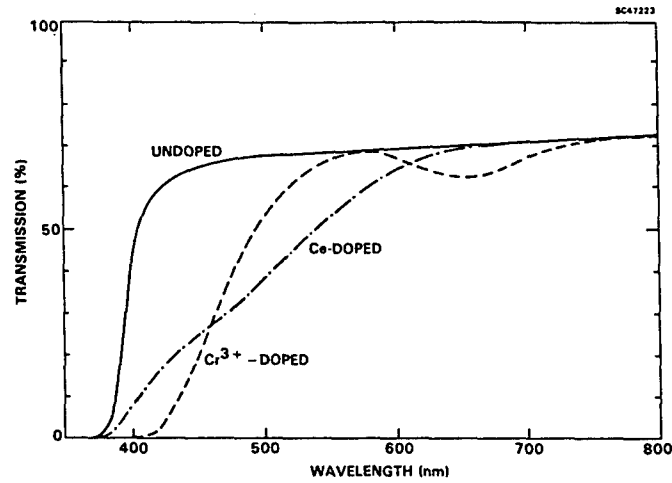FIG. 2 Transmission spectra for undoped and doped SBN:60 crystals.

TABLE 1
Ferroelectric and Optical Properties of SBN:60 Crystals

Property	Undoped SBN:60	Ce^{3+}-Doped (0.013 wt%)	Cr^{3+}-Doped (0.011 wt%)
Crystal Size (Diameter)	3 cm	2.5 cm	2 cm
Crystal Color	Pale Cream	Pink	Yellowish-Green
Crystal Quality	Optical	Optical	Optical
Dielectric Constant	$\epsilon_{33} = 920$ $\epsilon_{11} = 485$	$\epsilon_{33} = 950$ $\epsilon_{11} = 480$	$\epsilon_{33} = 1100$ $\epsilon_{11} = 485$
Phase Transition Temp.	75°C	74°C	72°C
Electro-Optic Coeff., r_{33} ($\times 10^{-12}$ m/V)	465	470	560*
Polarization ($\mu coul/cm^2$)	28.5	28	29
Beam Fanning Response:			
At 40 mW/cm²	——	2.5 s	0.90 s
At 0.2 W/cm²	——	0.6 s	0.30 s
At 2.0 W/cm²	——	0.05 s	0.018 s
Spectral Response (μm)	0.35 to 0.6	0.4 to 0.6	0.4 to 0.8**

* Estimated value using $r_{33} = 2g_{33}P_3\epsilon_{33}\epsilon_0$, g = 0.10 m⁴/c².

** Based on absorption spectra.

CONCLUSIONS

Our initial studies indicate that Cr^{3+}-doped SBN:60 has the potential to be a new photorefractive material that is competitive with, or superior to, both Ce^{3+}-doped SBN:60 and $BaTiO_3$. Further experiments are needed, however, to determine the photorefractive coupling coefficient and the crystal behavior as a self-pumped phase conjugator (22).

ACKNOWLEDGEMENT

REFERENCES

1.   Neurgaonkar, R.R., and Cory, W.K., J. Opt. Soc. Am. 3(B), 276 (1986).
2.   Neurgaonkar, R.R., Cory, W.K., Oliver, J.R., Ewbank, M.D., and Hall, W.F., J. Opt. Eng. 26(5), 392 (1987).
3.   Ewbank, M.D., Neurgaonkar, R.R., Cory, W.K., and Feinberg, J., J. Appl. Phys. 62(2), 374 (1987).
4.   Rakuljic, G.A., Yariv, A., and Neurgaonkar, R.R., J. Opt. Eng. 25, 1212 (1986).
5.   Rakuljic, G.A., Sayano, K., Yariv, A., and Neurgaonkar, R.R., Appl. Phys. Lett. 50(1), 10 (1987).
6.   Wood, G.L., Clark, III, W.W., Miller, M.J., Sharp, E.J., Salamo, G.J., and Neurgaonkar, R.R., IEEE J. Quant. Electron. QE-23, 2126 (1987).
7.   Miller, M.J., Sharp, E.J., Wood, G.L., Clark, III, W.W., Salamo, G.J., and Neurgaonkar, R.R., Opt. Lett. 12, 340 (1987).
8.   Megumi, K., Kozuka, H., Kobayashi, M. and Furuhata, Y., Appl. Phys. Lett. 30, 631 (1977).
9.   Ewbank, M.D., and Neurgaonkar, R.R., private communication.
10.   Ballman, A.A., and Brown, H., J. Cryst. Growth 1, 311 (1967).
11.   Megumi, K., Nagatsuma, N., Kashiwada, K., and Furuhata, Y., Mater. Sci. 11, 1583 (1976).
12.   Neurgaonkar, R.R., Cory, W.K., and Oliver, J.R., Ferroelectrics 15, 3 (1983).
13.   Neurgaonkar, R.R., Kalisher, M.H., Lim, T.C., Staples, E.J., and Keester, K.L., Mat. Res. Bull. 15, 1305 (1980).
14.   Neurgaonkar, R.R., Cory, W.K., Oliver, J.R., Miller, M.J., Clark, III, W.W., Wood, G.L. and Sharp, E.J., J. Cryst. Growth 84, 629 (1987).
15.   Dudnik, O.F., Gromov, A.K., Kravchenko, V.B., Kopylov, Yu. L., and Kunzetsov, G.F., Soviet Phys. Crystallgr. 15, 330 (1980).
16.   Gunter, P., Fluckiger, U., Huignard, J.P., and Micheron, F., Ferroelectrics 13, 297 (1976).
17.   Gunter, P.N., Opt. Lett. 7, 10 (1982); Phys. Rev. 93, 199 (1982).
18.   Amodei, J.J., Staebler, D.L., and Stephens, A.W., Appl. Phys. Lett. 18, 507 (1971).
19.   Ashykin, A., Tell, B., and Dziedzic, J. IEEE J. Quant. Electron. QE-3, 400 (1967).
20.   Montgomery, S.R., Yarrison-Rice, J., Pederson, D.O., Salamo, G.J., Miller, M.J., Clark, III, W.W., Wood, G.L., Sharp, E.J., and Neurgaonkar, R.R., to appear in J. Opt. Soc. Am. B.
21.   Feinberg, J., Opt. Lett. 7, 486 (1982).
22.   Feinberg, J., J. Opt. Soc. Am. 72, 46 (1981).

GROWTH AND FERROELECTRIC PROPERTIES OF TUNGSTEN BRONZE
$Sr_{2-x}Ca_xNaNb_5O_{15}$ SINGLE CRYSTALS

R.R. Neurgaonkar, W.K. Cory and J.R. Oliver
Rockwell International Science Center
Thousand Oaks, CA 91360

and

E.J. Sharp, G.L. Wood, M.J. Miller, W.W. Clark, III and G.J. Salamo
Center for Night Vision and Electro-Optics
Fort Belvoir, VA 22060-5677

ABSTRACT

The growth of ferroelectric $Sr_{2-x}Ca_xNaNb_5O_{15}$, $x = 0.1$ or 0.2, solid solution crystals by the Czochralski technique has been successful. The orthorhombic crystals exhibit large and almost equal transverse and longitudinal effects. Two phase transitions are observed, one paraelectric/ferroelectric ($T_c \approx$ 270°C), and the other ferroelectric/ferroelastic ($T_c \sim$ 95°C). The spontaneous polarization and pyroelectric coefficient are found to be large at 40 μcoul/cm² and 9.2×10^{-2} μcoul/ cm²-°C, respectively. The electro-optic coefficients, r_{33} and r_{51}, are estimated to be 1325×10^{-12} m/V and 1100×10^{-12} cm/V with optical figures of merit substantially larger than the current leading tetragonal bronze crystals such as SBN, BSKNN and SKN. Ce^{3+}- doped SCNN crystals also show strong fanning in the visible, indicating potential utility in photorefractive applications.

MATERIAL INDEX: tungsten, bronze

Introduction

Orthorhombic ferroelectric tungsten bronze single crystals have not yet received serious attention primarily due to problems in their growth as compared to tetragonal (4mm) bronzes such as $Sr_{1-x}Ba_xNb_2O_6$ (SBN), $Ba_{2-x}Sr_xK_{1-y}Na_yNb_5O_{15}$ (BSKNN), $K_3Li_2Nb_5O_{15}$ (KLN) and $Sr_2KNb_5O_{15}$ (SKN).[1-8] However, some of the orthorhombic candidates are potentially superior for electro-optic, nonlinear optic and SAW applications.   As a result, efforts were made in the early 1970's to grow $Pb_2KNb_5O_{15}$, $Ba_2NaNb_5O_{15}$, $Ba_2Ag_{0.5}Nb_5O_{15}$, $Sr_2NaNb_5O_{15}$, $K_2BiNb_5O_{15}$, $K_3Li_2Ta_{1-x}Nb_xO_{15}$, etc.   Two systems of greatest interest were $Pb_2KNb_5O_{15}$ and $Ba_2NaNb_5O_{15}$. $Pb_2KNb_5O_{15}$ shows outstanding piezoelectric and electromechanical coupling constants,[9-18] but its inherent growth problems (Pb^{2+} losses during growth and crystal cracking) prevented widespread application. $Ba_2NaNb_5O_{15}$ crystals were also grown in relatively large sizes (~ 1.5 cm in diameter) and proved to be slightly superior to $LiNbO_3$ in electro-optic and nonlinear optical characteristics.[14-17]

1459

Recently, we have been investigating orthorhombic systems which do not contain Pb^{2+}, such as $Ba_2NaNb_5O_{15}$-$Sr_2NaNb_5O_{15}$, $Sr_2NaNb_5O_{15}$-$Ca_2NaNb_5O_{15}$ and $Ba_2NaNb_5O_{15}$-$Ca_2NaNb_5O_{15}$,[18-21] with the intent of obtaining morphotropic phase boundary (MPB) regions at which electro-optical and other ferroelectric properties can be exceptionally large.[18] In the course of this study, we have found that the $Sr_2NaNb_5O_{15}$-$Ca_2NaNb_5O_{15}$ system, although not morphotropic, shows transverse and longitudinal effects which are nearly equal and exceptionally large, thus presenting an opportunity to develop new optical device concepts including optical computing, three-dimensional storage and display, image processing, etc. This paper reports the current results of our study in this system in terms of crystal growth and ferroelectric and optical properties.

Experimental

The $Sr_{2-x}Ca_xNaNb_5O_{15}$ (SCNN) solid solution system was initially studied using reagent grade chemicals, specifically $CaCO_3$, $SrCO_3$, Na_2CO_3 and Nb_2O_5. The appropriate weighed materials were thoroughly mixed and calcined at 900°C and then sintered between 1250-1380°C. The structure identification and the solubility of Ca^{2+} in the orthorhombic structure were checked using x-ray diffraction measurements. The compositions $Sr_{1.9}Ca_{0.1}NaNb_5O_{15}$ (SCNN-1) and $Sr_{1.8}Ca_{0.2}NaNb_5O_{15}$ (SCNN-2) were then studied in more detail using DTA techniques to ascertain melting temperatures and supercooling behavior.

For single crystal growth experiments, high-purity starting materials (Johnson Matthey, Ltd.) were used. To maintain a high degree of homogeneity in the crystals, the starting materials were thoroughly ball-milled before melting in a Pt crucible. Chemical analysis did not show the presence of Al_2O_3 due to the alumina ball-milling process. The crucible was 2 in. in both diameter and height, and was supported in a fibrous alumina insulating jacket. The furnace was rf induction-heated at 370 kHz. All crystals were cooled through their paraelectric/ferroelectric and ferroelectric/ferroelastic phase transition in an after-heater furnace.

A variety of techniques were used to evaluate the ferroelectric, pyroelectric and optical properties of these crystals. Crystals belonging to the orthorhombic point group (mm2) have five piezoelectric and electro-optic coefficients and three dielectric constants, thus requiring various samples of differing orientations. Prior to most measurements, the crystals were poled by a field-cooling method (T_c to room temperature) under a dc field of 5-10 kV/cm along the polar (001) axis using either Au or Pt electrodes. The completeness of poling was checked by measuring the dielectric constant before and after poling.

Results and Discussion

The SCNN-1 and SCNN-2 compositions exist on the pseudo-binary $Sr_2NaNb_5O_{15}$-$Ca_2NaNb_5O_{15}$ system, as shown in Fig.1b. The maximum solid solubility of Ca^{2+} was found to be approximately 33 mole%; beyond this limit, two phases, tungsten bronze SCNN and $Ca_2NaNb_5O_{15}$, were identified. The work on Ca^{2+} substitution in the bronze structure is of great interest and based on our current survey of $Ba_{1-x}Ca_xNb_2O_6$, $Pb_{1-x}Ca_xNb_2O_6$, $Pb_{2-x}Ca_xNaNb_5O_{15}$ and $Ba_{2-x}Ca_xNaNb_5O_{15}$, Ca^{2+} is a somewhat small ion for the 15-fold coordinated site. It is presumed, based on its solid solubility limit of 33 mole%, that Ca^{2+} lies predominantly in the 12-fold coordinated site.
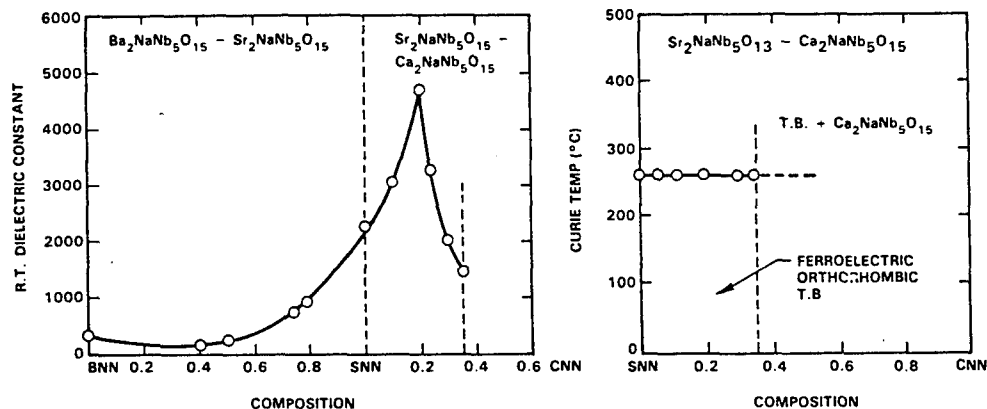
Fig. 1 The tungsten bronze $Sr_{2-x}Ca_xNaNb_5O_{15}$ system.

As shown in Fig. 1a and 1b, the substitution of smaller ions such as Sr^{2+} in $Ba_2NaNb_5O_{15}$ gradually increases the room-temperature dielectric constant of sintered ceramic materials. This increase continues as one adds Ca^{2+} in $Sr_2NaNb_5O_{15}$ up to 20% mole% Ca^{2+}, and then decreases for further additions. In the $Ba_2NaNb_5O_{15}$-$Sr_2NaNb_5O_{15}$ system, the ferroelectric phase transition temperature first decreased and then increased, indicating the possibility of a morphotropic phase boundary region. In the $Sr_2NaNb_5O_{15}$-$Ca_2NaNb_5O_{15}$ system, the phase transition temperature remains constant with the addition of Ca^{2+}. As shown in Fig. 1a, the highest room-temperature dielectric constant (5000) was observed for $Sr_{1.8}Ca_{0.2}NaNb_5O_{15}$; however, this value depends primarily on the influence of the ferroelectric/ferroelastic phase transition.

Both SCNN-1 and SCNN-2 crystals were grown using an automatic diameter-controlled Czochralski technique used for other tetragonal tungsten bronze crystals. Table 1 summarizes the growth conditions used for SCNN-1 and SCNN-2 single crystals. A major difficulty in the Czochralski growth of bulk single crystals from this bronze system is its orthorhombic structure (a = 17.481Å, b = 17.550Å and c = 3.899Å), and the resulting moderate lattice mismatch with tetragonal bronze seed material such as SBN:60 and SBN:75. However, as small single crystals of SCNN became available from early growths, SCNN seed crystals were used in subsequent growth experiments. Nevertheless, these crystal growths encountered considerable bulk fracture due to the following problems:

- Exchange of the crystallographic sites for Sr^{2+} and Na^+ between the 15- and 12-fold coordinated sites. This problem is less pronounced for Ca^{2+} since it prefers the 12-fold coordinate site.

- Crystal strain resulting from two phase transitions.

- Partial reduction of Nb^{5+} to Nb^{4+} during growth, resulting in crystal defects and severe crystal strain.

Despite these problems, evolutionary improvements in seed quality and crystal growth procedures have led to the Czochralski growth of crack-free SCNN (190/10) boules of up to 0.7 cm diameter; one such c-axis growth is shown in Fig. 2. Based on our previous work[19-21] on doped SBN and BSKNN crystals, Ce^{3+}-doped SCNN rystals were also

Table 1

Growth Conditions for the SCNN Single Crystals

Growth Composition	Pulling Rate Temp. (°C)	(mm/h)	Color	Size (cm)
SCNN-1	1465	6-7	Pale Cream	0.5 to 0.7
SCNN-1:Ce	1460	5-6	Pink	0.5
SCNN-2	1470	6-7	Pale Cream	0.7 to 0.8
SCNN-2:Ce	1467	5-6	Pink	0.5

All crystals were grown in oxygen along the (001) direction.
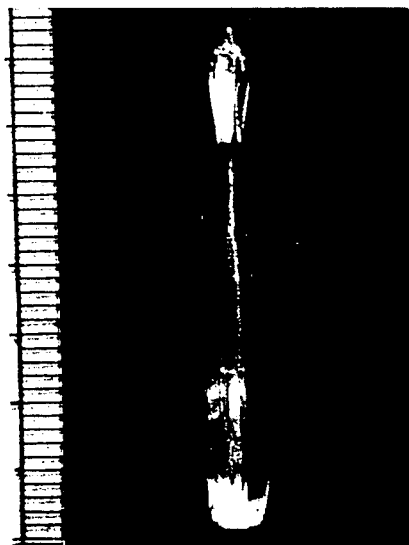Na loss due to volatilization was minimum for these crystals.

Fig. 2 Typical SCNN single crystal grown along the (001) direction.

grown because of the potential photorefractive properties they may exhibit. The addition of Ce^{3+} (0.05 wt%) did not significantly alter crystal growth parameters, and reasonable-size crystals (0.5 cm diameter) could be grown. However, both doped and, to some degree, undoped SCNN crystals tended to crack when sawn due to residual crystal strain. This cracking problem is felt to arise from 1) the orthorhombic structure and the presence of two-phase transitions below 300°C, 2) imperfect seed material, and 3) small changes in crystal composition during growth due to the mildly incongruent melting behavior of the material. The latter is a problem common to other bronze solid solutions such as tetragonal SBN:75 and BSKNN, and it requires patient refinement of the crystal growth procedures.

The successful growth of SCNN crystals permitted evaluation of their major ferroelectric and dielectric properties. Figure 3 shows the low-frequency dielectric constant vs temperature for two different orientations of SCNN (190/10). Along the c-
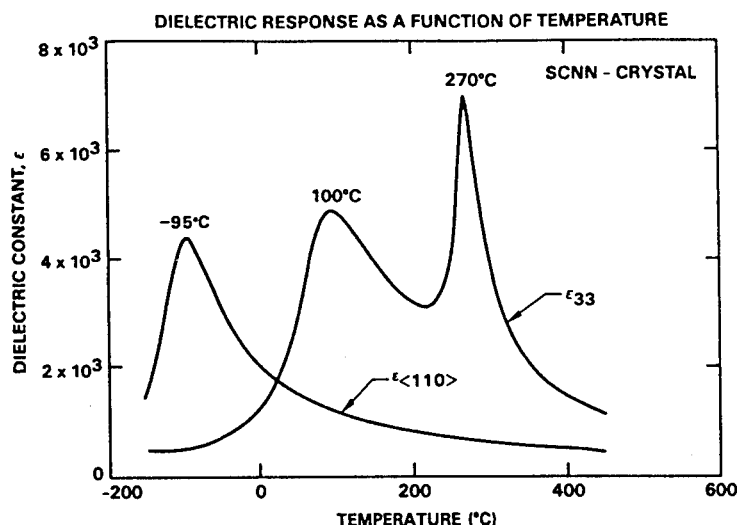
Fig. 3   Dielectric constant for single crystal SCNN (190/10) along <001> and <110> at 10 kHz. Dashed line is for <110> at 100 Hz.

axis, SCNN shows two prominent dielectric peaks, the largest being the strong first-order paraelectric/ferroelectric transition at $T_c = 270°C$, with a Curie-Weiss constant $C_c = 2.29 \times 10^5$ and a Curie temperature $\theta_3 = 240°C$. The substitution of Ca for Sr (up to the solubility limit) has little effect on the phase transition temperature. A broad second peak occurs between 30-100°C, depending on Ca content, and this is believed to be a ferroelastic transition. Below room temperature, the dielectric constant declines to an unusually large, nearly temperature-independent value of approximately 500.

The low-frequency dielectric constant along the c-axis is almost frequency-independent over the range of 100 Hz-100 kHz. The absence of frequency dispersion is unusual for tungsten bronze ferroelectrics, particularly near the phase transition temperature, and indicates a very narrow temperature distribution of θ_3 values. However, such is not the case for other orientations such as the <110> direction. In this direction, the two prominent peaks observed along the c-axis do not appear. Instead, the dielectric constant rises monotonically with decreasing temperature, and achieves a large, frequency-dependent maximum in the range of -88 to -100°C, as shown in Fig. 3. Such behavior may indicate a freeze-out of the dielectric polarizability effects in this orientation rather than the presence of another phase transition.

The room-temperature dielectric constants for both crystallographic directions are nearly equal (~ 1700), but dielectric anisotropy is evident over a wide temperature range above or below room temperature. Furthermore, the dielectric properties of the nonpolar directions such as <100>, <110>, etc., appear to be strongly affected by SCNN composition. This behavior is also observed for bronze BSKNN crystals of differing compositions.[6]

Typical c-axis polarization and pyroelectric behavior of SCNN (190/10) as a function of temperature are shown in Fig. 4. Because of the presence of the second transition near 100°C, SCNN shows a relatively wide-range temperature-independent pyroelectric coefficient, unlike other tungsten bronze ferroelectrics which have strongly decreasing coefficients below the ferroelectric phase transition temperature. Typical of a high Curie point ferroelectric, the room-temperature polarizability is large for this material at 40 μcoul/cm². This value is greater than that for other well-known
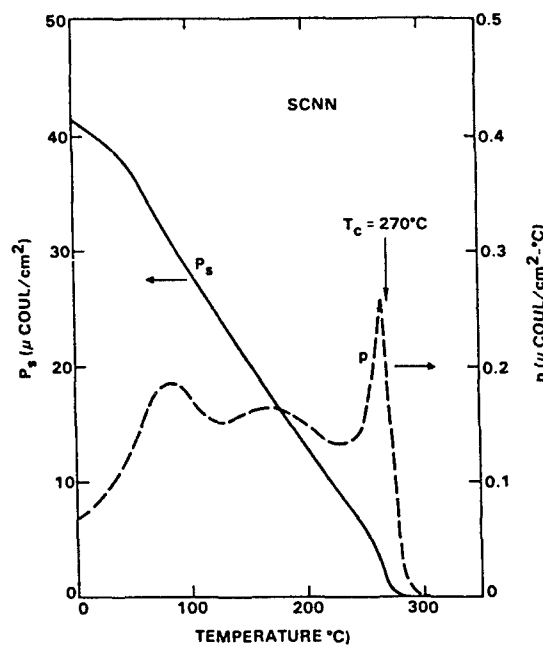
Fig. 4   Spontaneous polarization, P_s, and pyroelectric coefficient, p, as functions of temperature for an SCNN-1 c-axis crystal.

bronzes such as SBN, in part because of the added polarization arising from the second transition near 100°C. The high ferroelectric phase transition temperature necessitates poling in an oxygen atmosphere; however, poling at dc fields of 6-10 kV/cm while cooling through the phase transition does not cause excessive dc conductivity, overheating or breakdown problems.

The electro-optic coefficients r_{33} and r_{51} for SCNN-1 may be computed from the following relations:

$$r_{33} = 2g_{33}P_3\varepsilon_{33}\varepsilon_0$$

$$r_{51} = 2g_{44}P_3\varepsilon_{11}\varepsilon_0 \quad,$$

where g_{ij} is the quadratic electro-optic coefficient. For $g_{33} = 0.11$ m^4/C^2, r_{33} is estimated to be 1320×10^{-12} m/V. This value is close to the best known value for tetragonal bronze $Sr_{0.75}Ba_{0.25}Nb_2O_6$ (SBN:75), which exhibits an r_{33} value of approximately 1350×10^{-12} m/V. Similarly, using $g_{44} = 0.09$ m^4/C^2, r_{51} is estimated to be 1100×10^{-12} m/V for SCNN-1.

Table 2 summarizes the fundamental structural, ferroelectric and electro-optic properties of undoped SCNN-1, while Table 3 summarizes the optical figures of merit $n^3 r_{ij}/\varepsilon$ and r_{ij}/ε for SCNN, BSKNN, SBN and BaTiO$_3$. For photorefractive phase conjugation, image processing and optical computing applications, the relevant figure of merit can be taken as $n^3 r_{ij}/\varepsilon$, which is found to be substantially larger in SCNN crystals than for other materials of interest. This difference is due primarily to the high spontaneous polarization.

Table 2
Structural and Ferroelectric Properties of SCNN-1

Property	(001)	(110)
Dielectric Constant at 20°C (10 kHz)	1700	1740
Dielectric Loss Tangent at 20°C	0.003	0.004
Phase Transition Temperature	$T_{c1} = 270°C$ $T_{c2} = 95°C$	
Curie Temperature, θ	240°C	-18°C
Curie-Weiss Coefficient, C_c	2.29×10^5	1.85×10^5
Spontaneous Polarization at 20°C ($\mu coul/cm^2$)	39.8	
Pyroelectric Coefficient at 20°C ($\mu coul/cm^2$-°C)	9.2×10^{-2}	
Electro-Optic Coefficients ($\times 10^{-12}$ m/V)*	$r_{33} = 1325$	$r_{51} = 1100$

Lattice Constants (Å)   a = 17.469,   b = 17.522,   c = 3.904

* Estimated using ϵ and polarization values

Preliminary photorefractive beam-fanning experiments were carried out on a 1 mm x 2 mm x 3 mm SCNN crystal using a multiline argon-ion laser. Beam fanning was observed for the individual lines of the multiline laser after they were separated with an appropriate dispersing prism. With the laser oscillating simultaneously at all eight laser lines, we observed enhanced beam fanning or a photorefractive rainbow pattern. This behavior has also been reported in other bronze crystals.[25]

Attempts to achieve self-pumped phase conjugation in SCNN crystals have been inconclusive due to the relatively thin crystal samples available. A minimum interaction length, ℓ, is necessary for any particular coupling coefficient, γ, so that the coupling strength $\gamma\ell$ is sufficient to overcome losses in the material. Since the interaction length available in the present crystals is on the order of 1 mm or less, the coupling coefficient would have to be very large to obtain self-pumping. However, we have observed efficient self-pumping in other Ce-doped bronze crystals such as SBN:60, SBN:75, BSKNN-2 and BSKNN-3, and based on these results, we expect efficient self-pumping in SCNN as well. Currently, we are working to increase the size of SCNN crystals for this experiment. In general, SCNN crystals appear to be suitable not only for optical applications, but they could be of great interest in pyroelectric, SAW and piezoelectric applications.

Table 3
Electro-Optic Figure of Merit for Tungsten Bronze Crystals

Crystal	Dielectric Constant		r_{51}	Electro-Optic Coeff. (x 10^{-12} m/V)		
	ϵ_{11}	ϵ_{33}		r_{33}	r_{ij}/ϵ	$n^3 r_{ij}/\epsilon$
SBN:75	450	3000	42	1400	0.467	5.60
SBN:60	400	900	60	420	0.522	6.25
SCNN-1	1740	1700	1100	1325	0.75 (T)	8.90 (T)
					0.63 (L)	7.20 (L)
BSKNN-1	360	120	200	150	0.550	6.670
BSKNN-2	700	170	350	170	0.630	7.86
BSKNN-3	680	270	400	200	0.610	7.710
PBN:60	1900	500	2100	---	1.1	15.0
$BaTiO_3$	4100	1500	1600	80	0.390	4.01
$KNbO_3$	950	201	380	67	0.400	4.20

T = transverse electro-optic coefficient
L = longitudinal electro-optic coefficient

Acknowledgements

References

1.   R.R. Neurgaonkar, M.H. Kalisher, T.C. Lim, E.J. Staples and K.L. Keester, Mat. Res. Bull. 15, 1305 (1980).
2.   R.R. Neurgaonkar, W.K. Cory and J.R. Oliver, Ferroelectrics 35, 301 (1983).
3.   A.A. Ballman and H. Brown, J. Cryst. Growth. 1, 311 (1967).
4.   W.A. Bonner, J. Cryst. Growth 131 (1967).
5.   F.W. Ainger, J.A. Beswick, G.V. Smith and R. Clark, Ferroelectrics 3, 321 (1972).
6.   R.R. Neurgaonkar, W.K. Cory, J.R. Oliver, M.J. Miller, G.L. Wood, W.W. Clark, III and E.J. Sharp, J. Cryst. Growth. 84, 629 (1987).
7.   R.R. Neurgaonkar, W.W. Ho, W.K. Cory, W.F. Hall and L.E. Cross, Ferroelectrics 56, 230 (1984).
8.   R.B. Maciolek, T.L. Schuller and S.T. Liu, J. Electronic Mat. 2 (9), 415 (1976).
9.   R.L. Byer, S.E. Harris, D.J. Kuizenga and J.F. Young, J. Appl. Phys. 40, 444 (1969).
10.   L.G. Van Uitert, IEEE J. Quant. Electronics 4, 622 (1968).
11.   J.J. Amodei, Appl. Phys. Lett. 18, 507 (1971).
12.   T. Yamada, J. Appl. Phys. 46 (7), 2894 (1975).

13. J. Nakano and T. Yamada, J. Appl. Phys. 46, 2361 (1975).
14. P. Carr, Proc. IEEE Ultrasonics Symp. 74, 286 (1974).
15. T. Sugai and M. Wada, Jap.J. Appl. Phys. 13 (8), 2894 (1974).
16. T. Fukuda, H. Hirano and S. Koide, J. Cryst. Growth. 6, 293 (1970).
17. T. Fukuda, Jap. J. Appl. Phys. 9 (6), 599 (1970).
18. H. Hirano, H. Takai and S. Koide, Jap. J. Appl. Phys. 8, 972 (1969).
19. G. Salamo, M.J. Miller, W.W. Clark, III, G.L. Wood and E.J. Sharp, Opt. Comm. 59, 417 (1986).
20. M.J. Miller, E.J. Sharp, G.L. Wood, W.W. Clark, III, G.J. Salamo and R.R. Neurgaonkar, Opt. Lett. 12, 340 (1987).
21. J.R. Rodriguez, A. Siahmakoun, G.J. Salamo, M.J. Miller, W.W. Clark, III, G.L. Wood, E.J. Sharp and R.R. Neurgaonkar, Appl. Opt. 26, 1732 (1987).
22. G.L. Wood, W.W. Clark, III, M.J. Miller, E.J. Sharp, G.J. Salamo and R.R. Neurgaonkar, IEEE J. Quantum Electron. QE-23, 2126 (1987).
23. R.R. Neurgaonkar and W.K. Cory, J. Opt. Soc. Am. B3 (2), 274 (186).
24. R.R. Neurgaonkar, W.K. Cory, J.R. Oliver, M.D. Ewbank and W.F. Hall, Opt. Eng. 26 (5), 392 (1987).
25. G.J. Salamo, M.J. Miller, W.W. Clark, G.L. Wood, E.J. Sharp and R.R. Neurgaonkar, submitted to Opt. Lett.

Enhancing the response time for photorefractive beam fanning

John L. Shultz and Gregory J. Salamo

University of Arkansas
Physics Department
Fayetteville, Arkansas 72701

Edward J. Sharp and Gary L. Wood

CECOM Center for Night Vision and Electro-Optics
Fort Belvoir, Virginia 22060-5677

Richard J. Anderson

National Science Foundation
Washington, D.C.

and

Ratnakar R. Neurgaonkar

Rockwell International Science Center
Thousand Oaks, California 91360

ABSTRACT

Two types of optical limiting devices which have been demonstrated using photorefractive crystals are the "beam fanning" limiter and the "two-beam coupling" limiter. Experimental demonstrations of these two devices have revealed an interesting difference in behavior between those two limiter types. The two-beam coupling limiter is consistently faster than the beam fanning limiter for the same incident intensity. This is somewhat surprising since the beam fanning limiter is based on two-beam coupling phenomena. Our recent experiments show, however, that the relative speed of the two devices can be made more alike using a phase grating at the entrance face of the beam fanning limiter. While the phase grating scatters only about 1% to 5% of the incident light it apparently provides sufficient seeding to significantly enhance the beam fanning response time. Since the diffracted light is only about 1% the distortion to vision through the limiter due to dispersion is minimal. In the presentation we will present results from an experimental investigation of the effect of seeding on the "beam fanning" limiter response time. In particular, we have examined the response time dependence on the intensity and direction of the seed beam. Comparison with theory will also be presented.

INTRODUCTION

One of the more dramatic effects which can be observed using photorefractive crystals is the phenomenon of "beam fanning." A laser beam passes through a photorefractive crystal and in a short time the transmission through the crystal drops to near zero. Basically, the incident laser beam itself stimulates the crystal to reduce or limit its transmission. The observed reduction in transmission can be as high as three orders of magnitude. If the incident laser beam is suddenly re-directed through the crystal at a slightly different angle, different crystal position, or different laser wavelength, the transmission is revived only to again be limited as it falls to near zero. The photorefractive crystal clearly performs as an effective optical limiter.

BEAM FANNING

The physical explanation for beam fanning is quite simple. When the incident laser beam passes through the crystal, light is scattered by crystal imperfections in all directions. The scattered light, though weak in amplitude, crosses the incident beam and a weakly modulated grating is initiated. This weak grating causes energy to be exchanged or coupled from the strong incident beam into the weakly scattered light. The more intense scattered light now writes a more strongly modulated grating deeper into the crystal. This process bootstraps until most of the energy is exchanged from the incident beam into the scattered light in a fan-like pattern.

In this physical picture the basic mechanism behind beam fanning is the coupling or energy exchange that takes place between the incident beam and a scattered beam. This process is generally referred to as two-beam coupling.

In two-beam coupling two laser beams cross in a photorefractive material and write an index grating. The resulting grating is then responsible for the coupling between the two beams. In general energy is exchanged from one beam into the other. This effect can be nearly as dramatic as beam fanning itself, as nearly all of the energy in one beam can be observed to be depleted while the other beam receives nearly all of the lost energy.

Physically, therefore, beam fanning is thought to be a complicated summation of many two-beam coupling events. While this model is perfectly reasonable there is one noted difference. The speed of response for two-beam coupling is almost always observed to be considerably faster than the response time associated with beam fanning. This is true given all other conditions, such as laser intensity, crystal, incident angle, etc., are kept the same in order to make possible a fair comparison.

One possible reason for the difference observed is that the intensity for the scattered light, in the case of beam fanning, is so weak and in so many directions that some time is lost in establishing the first "seeding" of a grating before the bootstrap process officially kicks-in.

SEEDING THE FAN

In order to test the idea that the initial scattered light is weak and the cause of a slow start for the beam fanning phenomenon, we investigated the possibility of seeding the fanning with a more intense beam. Figure 1 depicts the seeding concept. A grating is placed in front of the photorefractive crystal. The incident laser beam now passes through the grating before entering the crystal. The incident beam on the grating is

diffracted into several beams which propagate through the crystal while overlapping each other. Because of the overlap, gratings are written and energy is exchanged. If the grating chosen diffracts more light than normally found scattered in the non-grating case, the crystal can be said to be seeded. The data shown in Figure 2a, b is for a series of gratings of 1% diffraction efficiency. The observed enhancement in speed is a modest factor of 3. On the other hand, with a diffraction efficiency of 5%, Figure 2c, d, the enhancement in speed is more like 8 or 9. That is, it appears that by providing the crystal with a seed beam of greater intensity than that normally found via scattering by crystal imperfections, the response time for the optical limiting behavior of the crystal is dramatically shortened and brought more in line with that observed for two-beam coupling experiments.

In order to investigate the seeding effect more thoroughly the apparatus of Figure 3 was employed. In particular, instead of using a series of gratings to provide the seed beam, a weak seed beam is intentionally crossed in the crystal with the incident beam. The intensity of the seed beam was then controlled using simple neutral density filters. The crossing angle was controlled by changing the arrangement slightly. As seen in Figure 4a, for an input seed intensity of 1% no significant enhancement was observed. On the other hand, for seed intensities of 5, 10, and 20% an increasing enhancement was noted as seen in Figure 4b, c, d. In addition to an enhancement in speed it is also interesting to note that the transmission was nearly always more limited with the seed beam than without (Figure 5).

DISCUSSION

Energy depletion from one beam into the other beam in two-beam coupling experiments is described for $I_{01} \gg I_{02}$ by the expressions

$$I_1(z) = \frac{I_1(0)(1+m)}{[1+m \exp(\Gamma z)]}$$

$$I_2(z) = \frac{I_2(0)(1+m)\exp(\Gamma z)}{[1+m \exp(\Gamma z)]} \tag{1}$$

where $I(0)$ is the incident intensity for beam 1 or 2, $I(z)$ is the intensity of beam 1 or 2 after propagation of a distance z in the crystal, Γ is the two-beam coupling gain coefficient, and m is the ratio

$$m = \frac{I_{02}}{I_{01}} \tag{2}$$

The gain coefficient for zero applied field is given by

$$\Gamma = \Gamma_0[1 - \exp(-t/\tau)] \tag{3}$$

where

$$\Gamma_0 = \frac{2\pi \, r_{eff} \, k_B \, T \, k_g \, \cos(2\theta)}{q \, \lambda \, n \, \cos\theta \left[1 + \frac{k_g^2}{k_0^2}\right]} \tag{4}$$

In this expression for Γ_0, q is the charge of the carrier, r_{eff} is the effective electro-optic coefficient, k_g is the grating wave vector, λ is the laser light wavelength, θ is the half-angle between the two crossing laser beams, and k_0 is the Debye screening wave vector given by

$$k_0^2 = \frac{q^2 N_{eff}}{k_B T \varepsilon} \tag{5}$$

In the expression for k_0^2, N_{eff} is the effective charge density, ε is the d.c. dielectric constant, and $k_B T$ is the thermal energy.

The response time for the formation of the two-beam coupling grating is given by the expression

$$\tau = \frac{1}{I_T}\left[\left(\frac{\varepsilon \hbar \omega}{\alpha q}\right)\left[1 + \frac{k_g^2}{k_0^2}\right]^{-1}\left(\frac{\gamma N_A}{\mu} + \frac{k_g^2 k_B T}{q}\right)\right] \tag{6}$$

where γ is the recombination rate coefficient, μ is the carrier mobility, N_A is the acceptor charge density, α is the absorption coefficient, and I_T is the total initial intensity.

As can be seen from expression (1) the change in intensity is dependent on the modulation index m. Since seeding can result in a higher modulation index than is normally present for beam fanning it can therefore produce a greater change in intensity via two beam coupling. This may explain the improved or higher depletion shown in Figure 5 when the beam fan is seeded.
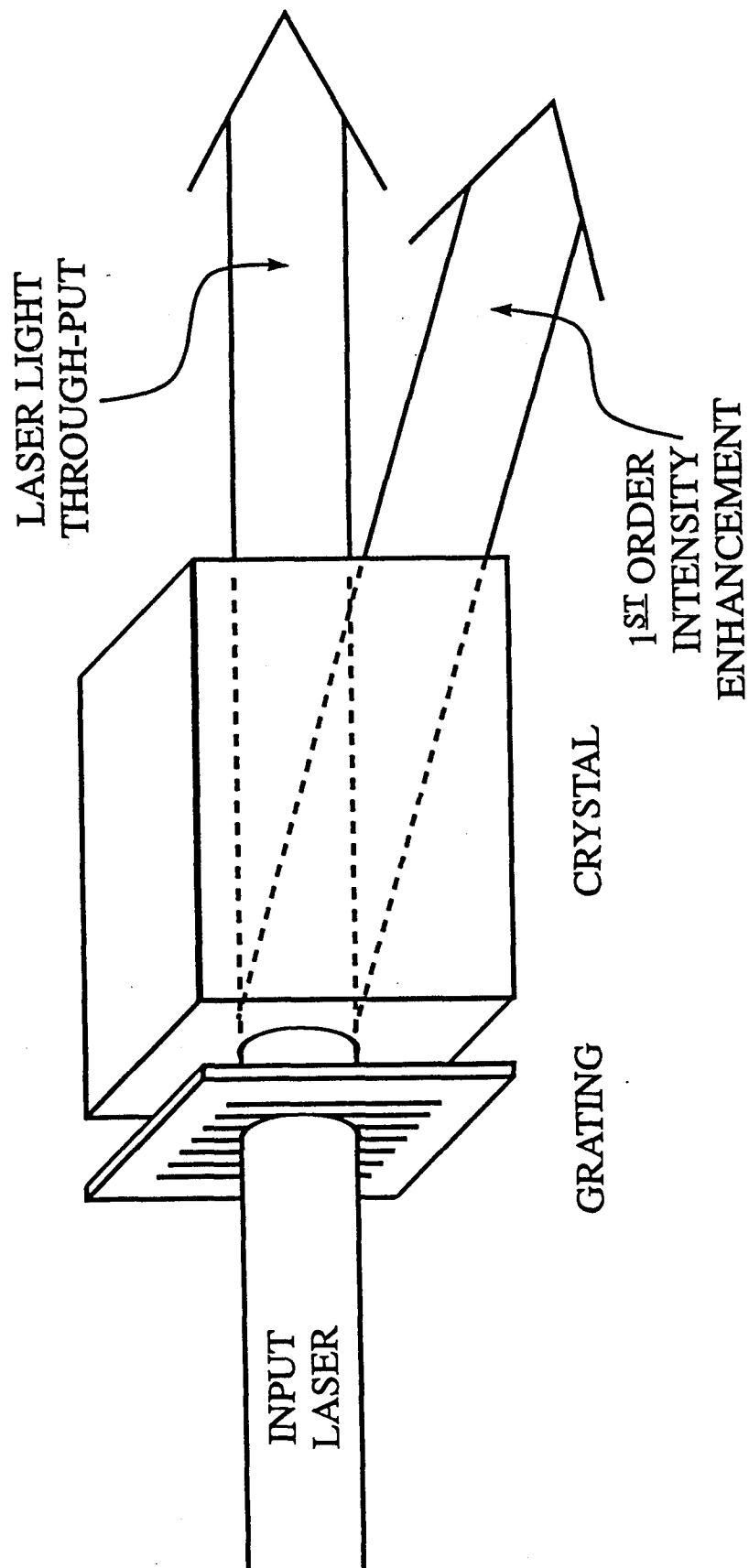
Expression (3) describes the time behavior of two-bean energy coupling. The characteristic response time is τ. As can be seen from expression (6), the response time has an intensity dependence which is inverse to the total intensity. Since seeding does not change the total intensity significantly a dramatic change in the beam fan time is not expected. For example, a 10% or 20% seed would not be expected to alter the response time by factors of 3 to 8. For this reason, the explanation for the improved response time most likely lies in the fact that the formation of the fan is thought to evolve from gratings which not only compete with each other but are also initially competing with the dark current. The addition of a seed beam of superior intensity perhaps encourages the energy exchange to take place more by the rules of two-beam coupling than by the more complex rules associated with beam fanning.
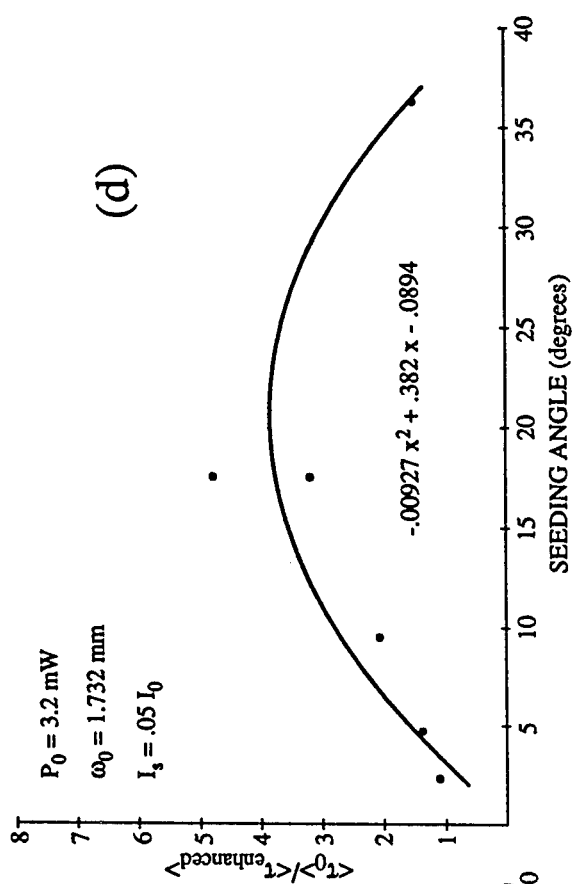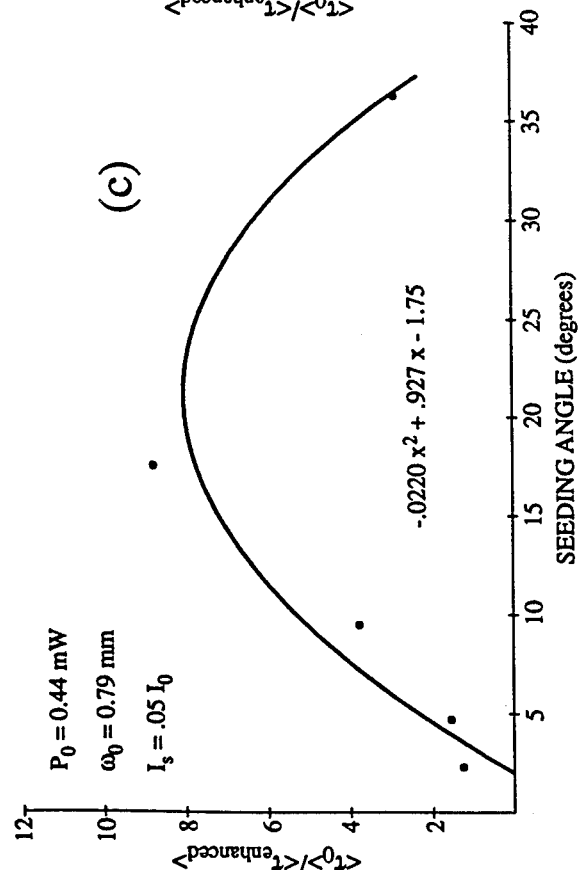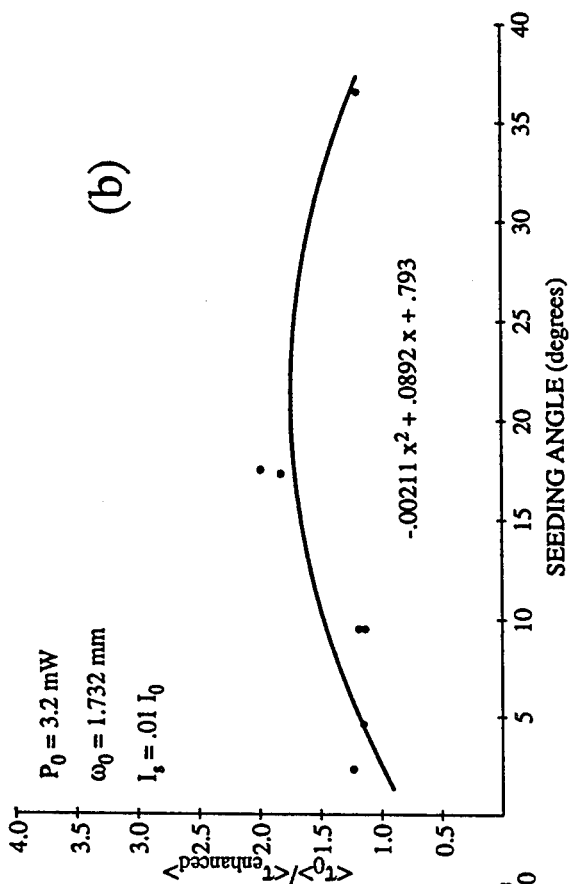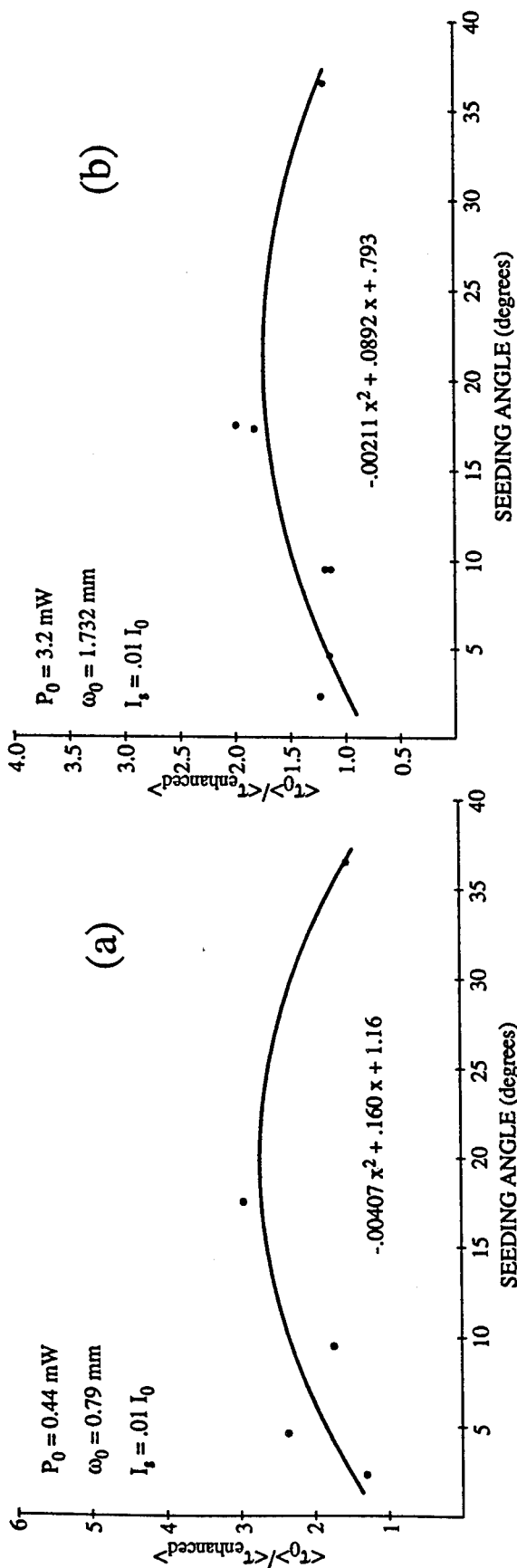
SUMMARY

We have demonstrated that the speed of response for a beam fanning optical limiter can be enhanced by using a grating in front of the photorefractive crystal in order to seed the fanning effect. One possible extension of the work is to investigate the possibility of fabricating a grating right on the crystal entrance face.
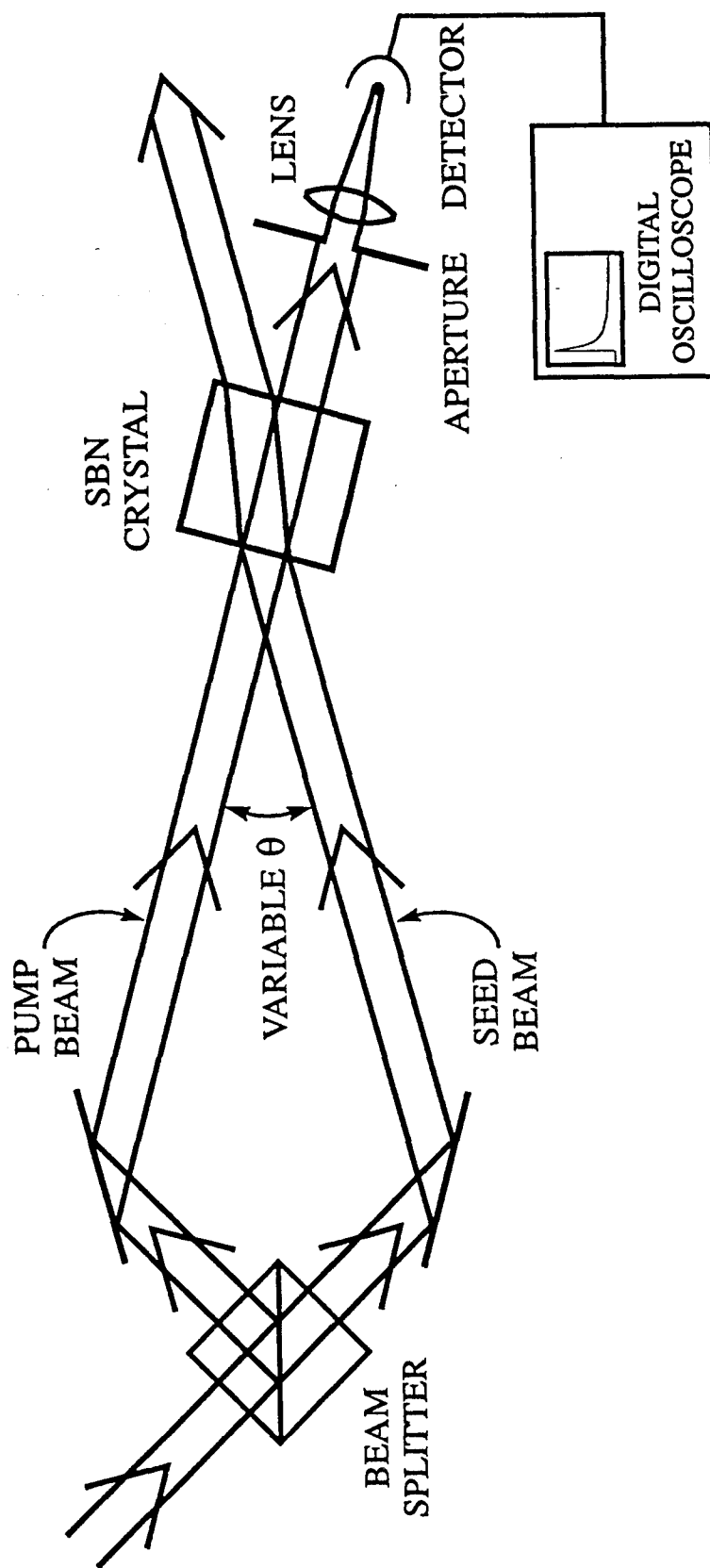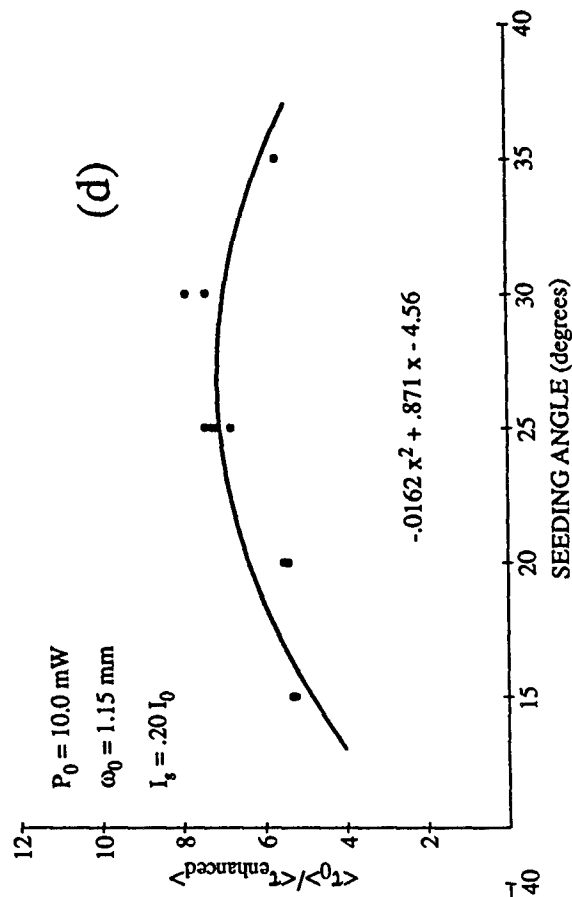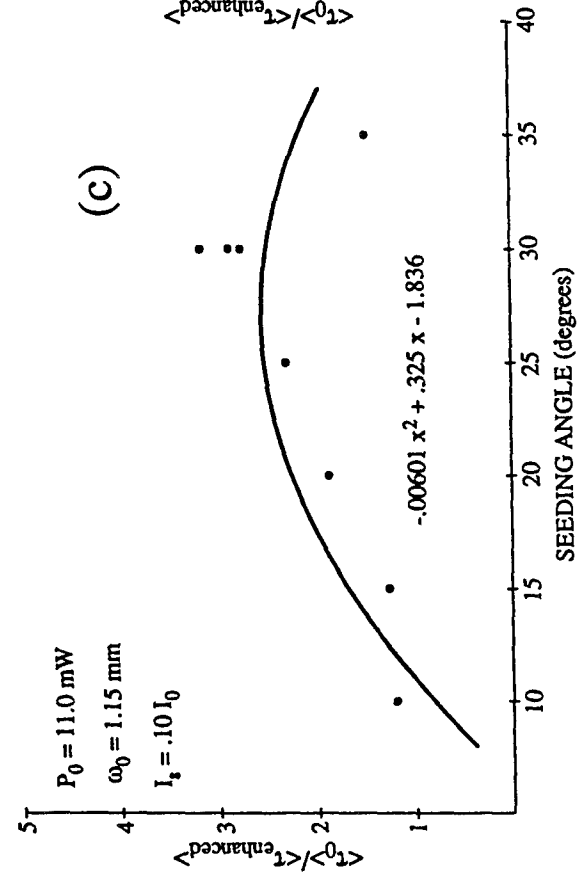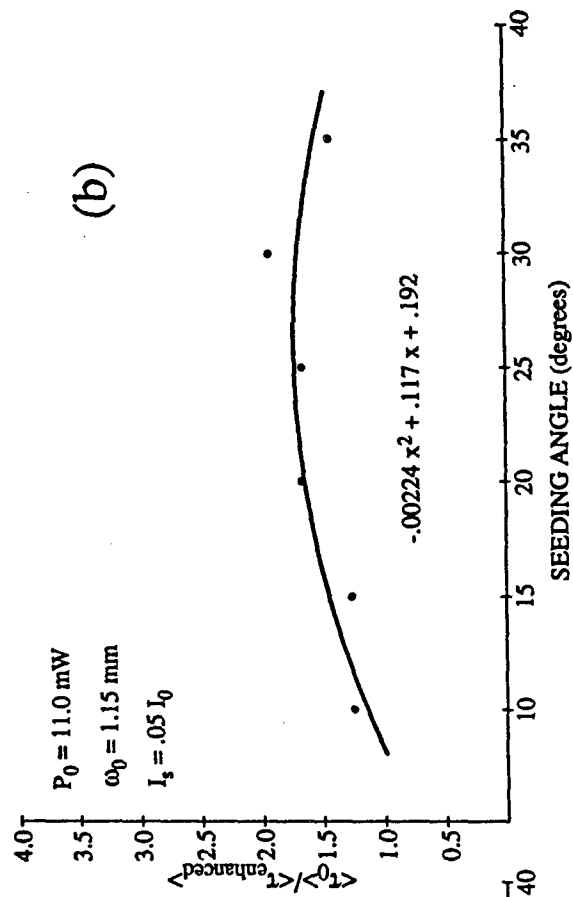
FIGURE CAPTIONS
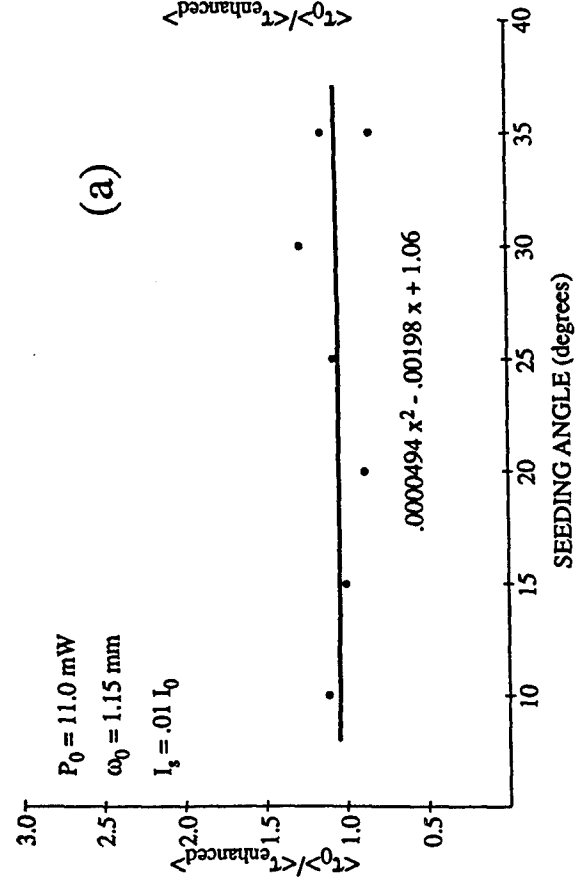
FIGURE 1: Conceptual diagram showing the basic idea behind the use of a grating to produce a weak beam to couple energy out of the incident beam propagating through the crystal.

FIGURE 2: Data showing the enhancement of the beam fanning effect due to the placement of a diffraction grating at the input face of the SBN crystal. The data show a dependence on the angle of seeding, i.e., on the resolution of the diffraction grating, as well as a dependence on the seeding intensity and the pump beam size.

FIGURE 3: Experimental apparatus for simulating the effect of a diffraction grating on the beam fanning effect. Translation of the SBN crystal along the symmetry axis of the beam splitter and rotation to maintain normal pump incidence allow for varying the seeding angle, θ.

FIGURE 4: Data showing beam fanning enhancement obtained with the apparatus shown in Figure 3 for seeding beam intensities of 1%, 5%, 10% and 20% of the pump intensity. Note the negligble enhancement for a seed intensity of 1% of the pump intensity.

FIGURE 5: (a) Unseeded transmission curve and (b) seeded transmission curve. Note the greater depletion of the transmitted beam in the seeded case as well as the enhanced time response.
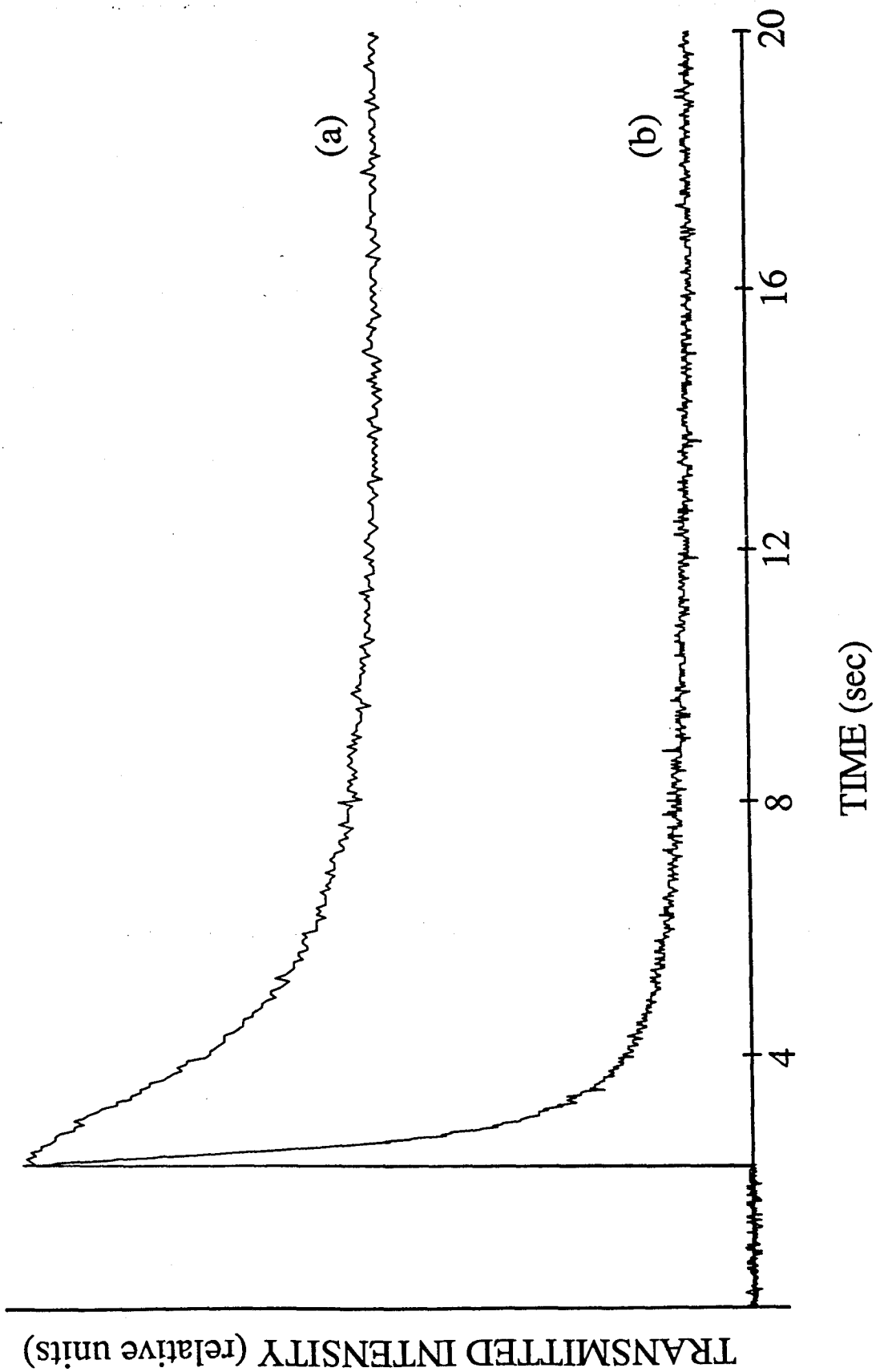
LASER LIGHT THROUGH-PUT

1ST ORDER INTENSITY ENHANCEMENT

CRYSTAL

GRATING

INPUT LASER

(a)

$P_0 = 0.44$ mW
$\omega_0 = 0.79$ mm
$I_s = .01\, I_0$

$-.00407\, x^2 + .160\, x + 1.16$

$\langle \tau_0 \rangle / \langle \tau_1 \text{enhanced} \rangle$

SEEDING ANGLE (degrees)

(b)

$P_0 = 3.2$ mW
$\omega_0 = 1.732$ mm
$I_s = .01\, I_0$

$-.00211\, x^2 + .0892\, x + .793$

$\langle \tau_0 \rangle / \langle \tau_1 \text{enhanced} \rangle$

SEEDING ANGLE (degrees)

(c)

$P_0 = 0.44$ mW
$\omega_0 = 0.79$ mm
$I_s = .05\, I_0$

$-.0220\, x^2 + .927\, x - 1.75$

$\langle \tau_0 \rangle / \langle \tau_1 \text{enhanced} \rangle$

SEEDING ANGLE (degrees)

(d)

$P_0 = 3.2$ mW
$\omega_0 = 1.732$ mm
$I_s = .05\, I_0$

$-.00927\, x^2 + .382\, x - .0894$

$\langle \tau_0 \rangle / \langle \tau_1 \text{enhanced} \rangle$

SEEDING ANGLE (degrees)

PUMP
BEAM

SEED
BEAM

VARIABLE θ

SBN
CRYSTAL

LENS

APERTURE   DETECTOR

DIGITAL
OSCILLOSCOPE

BEAM
SPLITTER

(a)

$P_0 = 11.0$ mW
$\omega_0 = 1.15$ mm
$I_s = .01 I_0$

$.0000494 \, x^2 - .00198 \, x + 1.06$

(b)

$P_0 = 11.0$ mW
$\omega_0 = 1.15$ mm
$I_s = .05 I_0$

$-.00224 \, x^2 + .117 \, x + .192$

(c)

$P_0 = 11.0$ mW
$\omega_0 = 1.15$ mm
$I_s = .10 I_0$

$-.00601 \, x^2 + .325 \, x - 1.836$

(d)

$P_0 = 10.0$ mW
$\omega_0 = 1.15$ mm
$I_s = .20 I_0$

$-.0162 \, x^2 + .871 \, x - 4.56$

The Use of Applied Electric Fields on the Photorefractive Tungsten Bronze Ferroelectrics

Nianyu Bei[1], Galen C. Duree[1], and Gregory J. Salamo[1], Rakesh Kapoor[2], Edward J. Sharp[3], and Ratnaker R. Neurgaonkar[4]

[1]Physics Department of the University of Arkansas, Fayetteville, Arkansas 72701
[2]Physics Department of Alabama A&M, Normal, Alabama 35762
[3]Army Research Laboratory, Fort Belvoir, Virginia 20060
[4]Rockwell International Science Center, Thousand Oaks, California 91360

Abstract--The traditional method of determining the photorefractive effective charge density is to plot the photorefractive space charge field versus the crossing angle in a two-beam coupling experiment. The difficulty with this traditional measurement technique is that the apparatus must be moved several times in order to obtain data over the sufficient number of crossing angles needed for an accurate fit with theory. Moreover, with small crossing angles the overlap between the two crossing beams can easily extend over the entire crystal, while with larger crossing angles the overlap between the two beams becomes less certain.

In this paper we demonstrate an alternative method of determining the photorefractive charge density. In this approach we measure the phase shift between the optical intensity pattern in the crystal and the resulting index pattern, as a function of the magnitude of an applied d.c. field. By comparing the measured value of the d.c. field which produces a minimum phase shift with that predicted by theory the photorefractive effective charge density is found. In this case, only the magnitude of the applied field is varied and the apparatus remains fixed. The result is obtained quickly and with little error.

INTRODUCTION

In this paper we discuss a technique to measure the trap density in photorefractive crystals. The technique is based on the use of interfering two laser beams in a crystal in the presence of an applied electric field. In the crystal the two light waves can be expressed as

$$E_T(x,z) = E_{T0} \exp[i(k_x x + k_z z)] \quad (1)$$

$$E_D(x,z) = E_{D0} \exp[i(-k_x x + k_z z)] \quad (2)$$

where k_x and k_z are components of the wavevector. The two light beams cross at an angle 2θ in the crystal with each beam making an angle θ with the normal to the incident surface. If ϕ is the phase shift between the grating and the interference pattern, the intensities of the output beams from the crystal can be written [Ref. 1] as

$$I_T(d) = I_T\cos^2(\kappa d) + I_D\sin^2(\kappa d) - (I_T I_D)^{1/2}\sin(2\kappa d)\sin\phi \quad (3)$$

$$I_D(d) = I_D\cos^2(\kappa d) + I_T\sin^2(\kappa d) + (I_T I_D)^{1/2}\sin(2\kappa d)\sin\phi \quad (4)$$

where I_T and I_D are the incident intensities and $I_T(d)$ and $I_D(d)$ are their intensities after passing through a crystal of thickness d with a coupling coefficient κ. In expressions (3) and (4), the first term corresponds to the transmitted component, the second term is the diffracted component, and the third term is the energy-exchange component between the two beams. From expressions (3) and (4) we can write the diffraction efficiency η as

$$\eta = \sin^2(\kappa d) \quad (5)$$

If the intensity of both beams is adjusted to be equal at the entrance of the crystal we can write the energy exchange efficiency in terms of the diffraction efficiency as

$$\varepsilon = 2[\eta(1-\eta)]^{1/2}\sin\phi \quad (6)$$

Therefore, expression (6) yields an expression for the phase shift between the intensity pattern and the index grating and is given by

$$\sin\phi = \varepsilon/\{2[\eta(1-\eta)]^{1/2}\} \quad (7)$$

$$\sin\phi = I_\varepsilon/\{2[I_d(I_0 - I_d)]^{1/2}\} \quad (8)$$

where I_ε, I_d and I_0 are the magnitude of the energy exchange, the diffraction signal and the intensity of the transmitted beam. From these expressions we can see that by measuring I_d, I_ε, and I_0, ϕ can be determined [Ref 2,3,4].

EXPERIMENTAL TECHNIQUE

The apparatus which we used to measure ϕ as a function of applied d.c. electric field consisted of a HeNe laser oscillating at 6328A with an output power of 5mw. We used ordinary polarized beams in order to minimize beam fanning and the corresponding intensity fluctuations which appear in energy exchange signals. After the polarizer, the laser beam was split into two beams I_D and I_T which intersected inside a thin sample of SBN 60 with 0.015% Cesium as a dopant (static dielectric constant $\varepsilon' = 950$) such that the grating vector is parallel to the c-axis. The beam splitter is 50% /50% to make the beam I_D have the same intensity as I_T. The angle 2θ

between the two beams was 22°. The beam $I_T(d)$ was detected with a photodiode. For all our observed intensity values the photodiode was linear. To avoid the observation of multi-exponential growth and decay times, the detected beam was expanded with a beam expander so that only the uniform portion of the beam was detected by the photodiode. The output of the diode was fed into a 602A Digitizing Signal Analyzer. After turning on both beams a growth curve was recorded and the energy exchange signal I_ε was measured. When the grating reached its steady state we blocked the detected beam. The transmitted beam immediately went to zero, and the diffraction signal I_d was detected. Finally, the intensity of the transmitted beam I_0 was measured. By substituting I_0, I_ε, and I_d into expression (8), we can calculate the phase shift between the grating and the interference pattern in the crystal.

After applying a d.c. field across a crystal we carried out the measurement described above yielding values for I_0, I_ε, and I_d. By substituting them into expression (8) we calculated both the $\sin \varphi$ and the $\tan \varphi$. In order to get accurate results we varied the magnitude of the d.c. field and measured I_0, I_ε, and I_d for each d.c. field value E_0.

From the band transport theory we have

$$\tan \varphi = \frac{E_D}{E_0} + \left(\frac{E_D^2}{E_0} + E_0 \right) \frac{1}{E_q} \tag{9}$$

$$\frac{1}{E_q} = \left(\tan \varphi - \frac{E_D}{E_0} \right) \Big/ \left(\frac{E_D^2}{E_0} + E_0 \right) \tag{10}$$

Expression (9) gives a value of E_0 for minimum ϕ of $E_0 = \left[E_D E_q + E_D^2 \right]^{1/2}$. Using expression (10) we are able to calculate a set of data for $1/E_q$ vs E_0. E_q is defined as $E_q = 4\pi e N_{eff}/\varepsilon K_g$ where N_{eff} is approximately the trap density N_A for our crystal. Since we observe that E_q depends on E_0 the dielectric constant ε must depend on E_0. For the parameters used in our experiment we have

$$K_g = \frac{2\pi}{\lambda}(2\sin \theta) = 3.79 \times 10^4 \, cm^{-1}$$

$$E_D = \frac{K_B T K_g}{e} = 963.24 \, v/cm \tag{11}$$

$$E_q = \frac{4\pi e}{K_g} \left(\frac{N_{eff}}{\varepsilon} \right) = \left(4.776 \times 10^{-11} \right) \left(\frac{N_{eff}}{\varepsilon} \right)$$

For our work we assume that the dependence of the dielectric constant ε on the magnitude of the d.c. field E_0 is

$$\varepsilon (E_0) = \varepsilon' \left(1 + \alpha E_0 + \beta E_0^2 \right)$$
$$= \varepsilon' \left[1 + f(E_0) \right] \tag{12}$$

where α and β are constants to be determined.

By combining expressions (10), (11) and (12) we can calculate $1/E_q$ and N_{eff}/ε' for each value of d.c. field E_0. Using these values we plotted $\{[1+f[(E_0)_i]\}/\{1+f[(E_0)_1]\}$ versus $(E_0)_i$ as shown in Fig. 1. By fitting the data we found that $\alpha = 0.0009515$ and $\beta = -2.51 \times 10^{-7}$. As a result we can write
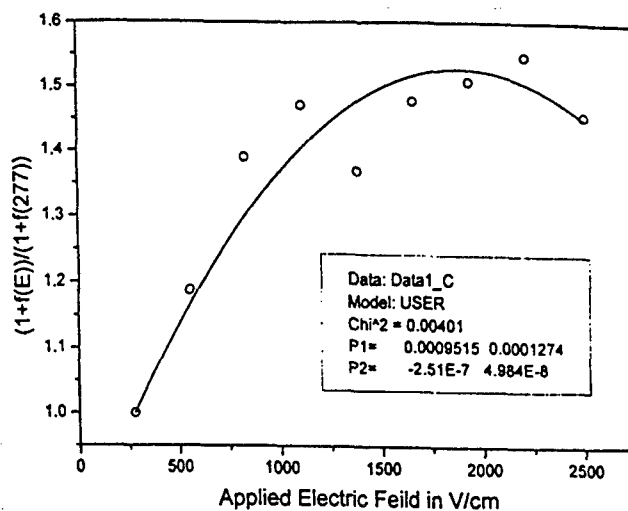

Fig 1. Determining the electric field dependence of the dielectric constant

$$E_q = \frac{4.776 \cdot 10^{-11}}{1 + 0.0009515 E_0 - \left(2.51 \cdot 10^{-7} \right) E_0^2} \left(\frac{N_{eff}}{\varepsilon'} \right) \tag{13}$$

For each pair of E_0 and E_q we can now calculate the value of N_{eff}/ε'.

By taking the average, we obtained $N_{eff}/\varepsilon' = (4.54 \pm 0.38) \times 10^{13}(cm^{-3})$. For our crystal the value of ε' is 950. Therefore, we get $N_{eff} = (4.31 \pm 0.36) \times 10^{16}(cm^{-3})$. In [Ref. 2] an N_A value of $(4.2 \pm 0.2) \times 10^{16}$ (cm^{-3}) was reported for the crystal of SBN: 60 with 0.015% Rh. concentration. Our results are in good agreement with their reported value.

Also we plotted curves of $\sin\varphi$ vs E_0, $\tan \varphi$ vs E_0 and ε vs E_0, respectively. They are shown in Fig. 2, 3, and 4.

In order to exam the accuracy of the N_A value which we obtained by using the phase-electric field method, we also did an experiment to measure N_A by using the traditional
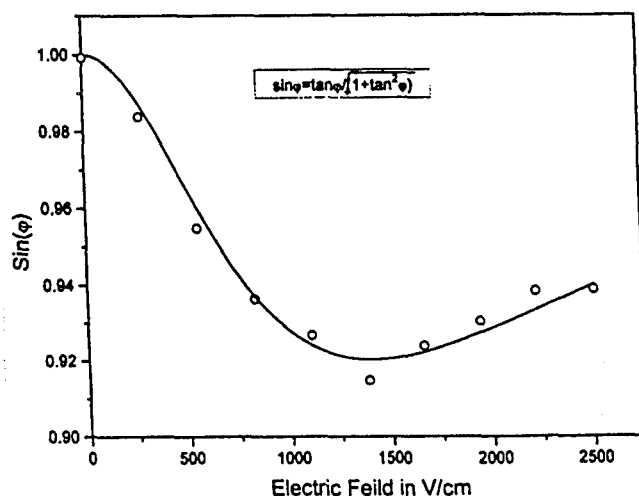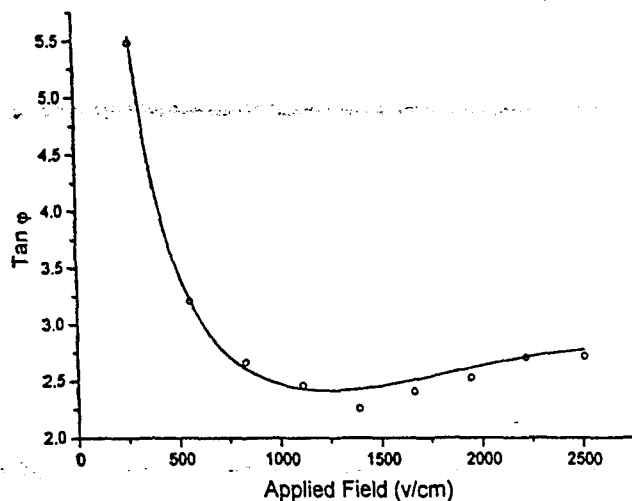

Fig 2. The $\sin\varphi$ as a function of applied field

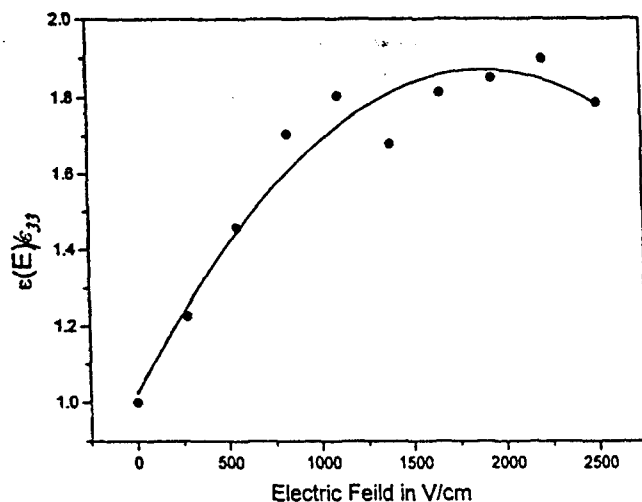Fig 3. The tanφ as a function of applied field

Fig 4. The dielectric constant as a function of applied field

method of changing the angle between the two crossing beams. The basic theory and measurement procedure are described in detail in [Ref. 5].

Due to two-beam coupling, the weak beam I_1 experiences an increase in intensity along its propagation direction which is given by

$$\frac{I_{1c}}{I_1} = \frac{(1+m)e^{\gamma L_{eff}}}{1+me^{\gamma L_{eff}}} \qquad (14)$$

where $m = I_{01}/I_{02}$, the ratio of the weak beam intensity to the strong beam intensity. Experimentally, we measured I_{1c}, I_1 and m, and then calculated γL_{eff}. On the other hand

$$\gamma L_{eff} = A \frac{R_{eff}}{\cos\theta} \cdot \frac{K_g}{1+\left(K_g/K_0\right)^2} \qquad (15)$$

where $R_{eff} = n_e^4 r_{33}\cos^2\theta - n_0^4 r_{13}\sin^2\theta$ for an extraordinary ray, A is a constant, K_g is the grating constant and $K_0^2 = \frac{4\pi e^2}{K_B T}\left(\frac{N_{eff}}{\epsilon}\right) = C\left(\frac{N_{eff}}{\epsilon}\right)$ provided $C = 4\pi e^2/K_B T$. By

defining

$$f(\theta) = \frac{\cos\theta}{\cos^2\theta - \frac{n_0^4 r_{13}}{n_e^4 r_{33}}\sin^2\theta} \qquad (16)$$

we will have

$$\gamma L_{eff} f(\theta) = B\frac{K_g}{1+\frac{K_g^2}{C}\bigg/\left(\frac{N_{eff}}{\epsilon}\right)} \qquad (17)$$

where B is a constant. By plotting the data of $\gamma L_{eff}f(\theta)$ vs K_g and fitting the data, we then obtained a value of N_{eff}/ϵ. The fitting result (Fig. 5) gave us a value of $N_{eff}/\epsilon = (4.59 \pm 0.31) \times 10^{13}(cm^{-3})$ which is in good agreement with our results using the phase measurement technique.
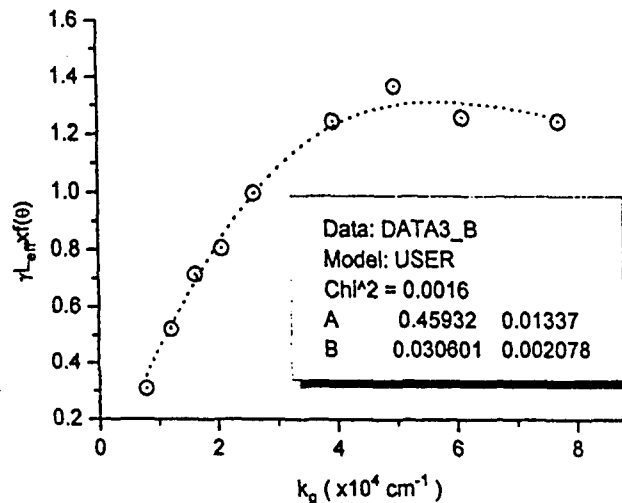

Fig 5. The photorefractive gain as a function of crossing angle

CONCLUSION

We have demonstrated a technique for the measurement of the trap density in photorefractive materials. This technique has been shown to give the same result for the trap density as the conventional two-beam coupling technique but is more convenient to carry out in practice. The technique presented here also yields the electric field dependence of the dielectric constant.

REFERENCES

1. H. Kogelnik, Bell Syst. Tech. J. Vol 48, 6929 (1969).
2. R.A. Vazquez et al, JOSA B, Vol 9, 1416 (1992).
3. R. Kapoor et al, Opt. Lett. Vol 8, No 9, May 1, (1993).
4. J.P. Wilde et al, Opt. Lett. Vol 17, 853 (1992).
5. G.L. Wood, G.J. Salamo et al, IEEE J. Quan. Electro. Vol QE-23, 2126 (1987).

Enhanced photorefractive beam fanning due to internal and external electric fields

William W. Clark III, Gary L. Wood, Mary J. Miller, Edward J. Sharp, Gregory J. Salamo, Brian Monson, and Ratnakar R. Neurgaonkar

Significant increases (×10) in both speed and gain of the beam fanning process were obtained via three different methods in SBN and BSKNN. These methods involve the creation of a dc electric field either (1) externally, (2) by the pyroelectric effect, or (3) by thermally cycling the crystal and the presence of laser radiation. The enhanced effects were observed for both ordinary and extraordinary polarized light.
Key words: photorefraction, SBN, BSKNN, space-charge field, beam coupling.

I. Introduction

Beam fanning[1] is a well-known photorefractive phenomenon in which light from a laser is scattered asymmetrically as it passes through a high gain crystal. This is a result of the two-beam coupling[2] process where the input beam interacts with its own scattered light, forms a diffraction grating, and couples additional energy into the scattered light. This weakens the transmission in the direction of propagation and produces a broad fan of light to one side of the main beam as shown in Fig. 1.

Beam fanning has possible use in optical communications,[3] optical limiting,[4] motion detection,[5] and plays an auxiliary role in the formation of self-pumped phase conjugators[6] and double phase conjugate mirrors.[7] Most of these applications demand both fast response and high gain, but few, if any, current materials are considered able to meet both criteria. We report on experiments which show that significant increases in both speed and gain can be obtained from application of an electric field in SBN and BSKNN. In addition, these increases were obtained for ordinary as well as extraordinary polarized light. An example of the enhanced fan is shown in Fig. 2. Note that much

more light appears in the enhanced fan in just two seconds than in the normal (zero-field) fan after a considerably longer time [Fig. 1(b)].

The electric field which produces the enhanced effect could be applied directly or it could be self-generated through temperature changes. In fact, three alternate techniques were used to produce enhanced effects: (1) the external field method, (2) the pyroelectric method, and (3) the thermal cycle method. In Fig. 2 the crystal was prepared using the latter method, although similar results were observed by using any of the three methods. Each of these methods along with corresponding quantitative results are presented below.

II. Experimental Apparatus

For these experiments, the amount of beam fanning was measured by observing the decrease in the straight-through transmission of a laser beam as it passed through a photorefractive crystal. As seen in Fig. 3, radiation from either a He–Cd laser (442 nm) or a He–Ne laser (633 nm) was directed normally to the (100) face of the crystal which was housed in a temperature controlled oven. The power at the crystal from each laser was ~5 mW in a TEM_{00} mode and the spot size was ~1.8 mm in diameter. After leaving the crystal, the on-axis radiation passed through an aperture (~3-mm diameter) and the decrease in transmission was measured by use of a silicon diode detector. For visual observation the aperture and detector were replaced by a screen and the transmitted light could be photographed or recorded with a video camera. Although enhanced results were observed for many of our SBN and BSKNN crystals, most of the curves and calculations which follow will be for our 0.65-cm cube of cerium doped SBN:60 (crystal 3 of Ref. 8) because of knowledge of its material properties.
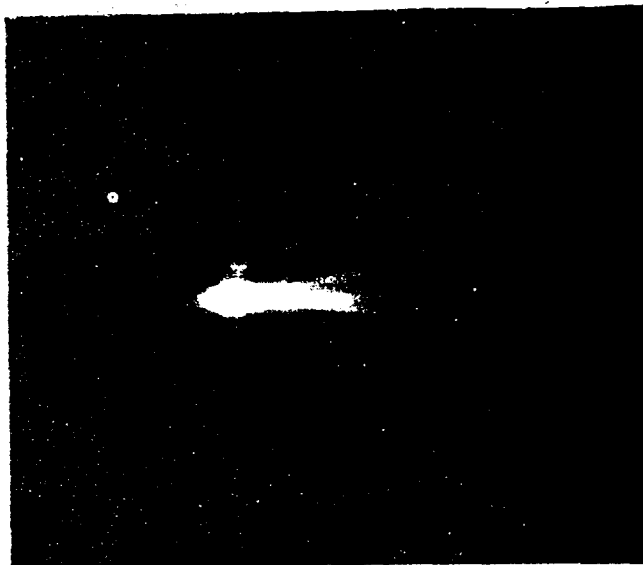
Ratnakar Neurgaonkar is with Rockwell International Science Center, Thousand Oaks, California 91360; G. J. Salamo and B. Monson are with University of Arkansas, Fayetteville, Arkansas 72701; and the other authors are with CECOM Center for Night Vision & Electro-Optics, Fort Belvoir, Virginia 22060-5677.

(a)

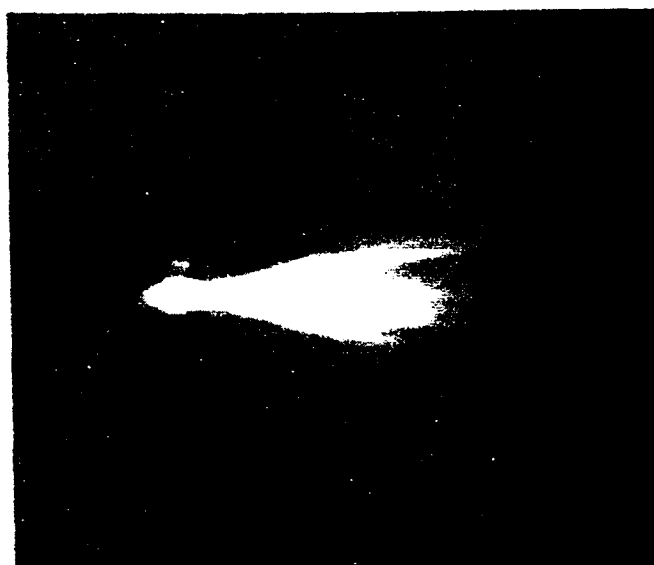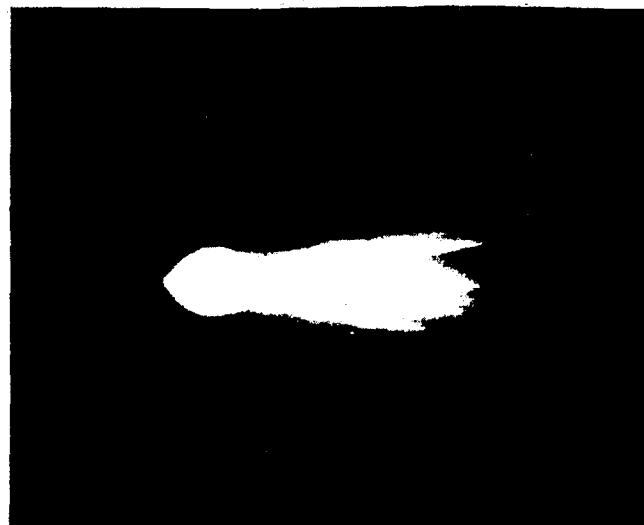Fig. 2. Enhanced beam fan with ordinary light and a self-generated field after 2 s. The photograph was taken with the same exposure setting and crystal orientation as Fig. 1.
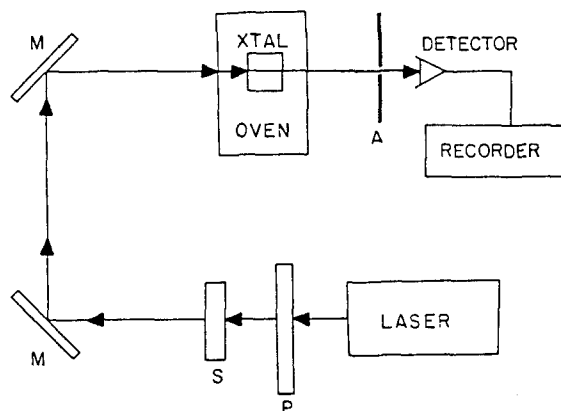

(b)

Fig. 1. Beam fanning from a crystal of Ce-SBN:60 using ordinary polarized light and no applied field: (a) Two seconds after turn-on, (b) steady state, and 60 s after turn-on. The photographs were taken by replacing the aperture in Fig. 3 with a screen. The crystal c-axis pointed to the left.

Fig. 3. Experimental apparatus: P, polarization rotator; S, shutter; M, mirror; A, aperture; LASER, He–Cd or He–Ne.

Two different ovens were used in the experiments. The first oven was an Inrad 5-15 temperature phase matching SHG system which totally enclosed the crystal in a dry air environment and could change temperature at a rate of about 1°C/min. It had a narrow field-of-view and no connections for electrodes. The second oven was a homemade thermoelectric hot plate which left the crystal exposed to room air and had a rate of 16°C/min. It had a wide field-of-view which permitted visual observation of the beam fan. It also allowed electrodes to be connected to the crystal. The enclosed oven had a temperature range of −70°C to +30°C while the open oven had a range from +10°C to 100°C. At no time was the temperature raised above the Curie point of the crystal. Temperature gradients were present in the second oven but did not appear to affect the experimental results which were similar for both ovens. Unfortunately, the geometrical features of the ovens made it impractical to perform phase-conjugation or two-beam coupling experiments. Modifications are planned to enable these experiments to be carried out in the near future.

III. Theory

MKS units are used in this paper along with the following basic symbols:

h Planck constant
K_B Boltzmann constant
m intensity modulation index
n index of refraction
q elementary charge
r_{eff} effective electrooptic coefficient
T temperature
α absorption coefficient
ϵ_0 permittivity of vacuum
ϵ_r relative dielectric constant
Θ beam crossing angle
Λ_g grating period $= \lambda_0/[2n \sin(\Theta/2)]$
λ_0 wavelength of laser light in vacuum
μ mobility
ν light frequency

The effect of electric fields on beam fanning is found by examining the theory for two-beam coupling. This is justified because the scattering due to beam fanning can be modeled as two-beam coupling between the incident beam and many scattered beams.[9] In two-beam coupling, two laser beams overlap and produce an interference pattern. The modulated light pattern ionizes some fraction of neutral donors and excites charges into the conduction band (or valence band). The liberated charges then diffuse or drift to dark regions in the crystal where they recombine with ionized donors. As a result of the charge transport, a charge separation develops which is eventually limited by the restoring force of the corresponding space charge field, E_{sc}. The variation of the electric field in the crystal causes a distortion of the lattice and develops a modulated refractive index pattern or grating. Since the space-charge field is related to the space-charge density (ρ_{sc}) by the Poisson equation, there is a phase shift between the intensity pattern and the index pattern. The consequence of the phase shift is asymmetric energy transfer from one beam to the other. The energy transfer that occurs in two-beam coupling is physically responsible for the beam fanning effect.

For a small intensity modulation index, the two-beam coupling gain coefficient can be expressed as,[10]

$$\gamma = [2\pi n^3 r_{eff}/m\lambda_0] \times E_{sc}(90°), \qquad (1)$$

where $E_{sc}(90°)$ is the amplitude of the space-charge field which is 90° out of phase with the light interference pattern. $E_{sc}(90°)$ is the only term with a significant dependence on an applied field for the field strengths encountered in this work. The steady-state value of the space-charge field is given by[10–12]

$$E_{sc}(90°) = mE_q \frac{E_D(E_q + E_D) + E_0^2}{(E_q + E_D)^2 + E_0^2}. \qquad (2)$$

where $E_q = qN_{eff}\Lambda_g/2\pi\epsilon_r\epsilon_0$ is the limiting space-charge field, $E_D = 2\pi K_B T/\Lambda_g q$ is the diffusion field, E_0 is the component of the applied field normal to the grating planes, and N_{eff} is the effective number of photorefractive charges. By looking at the limits of $E_{sc}(90°)$ as $E_0 \rightarrow 0$ and $E_0 \rightarrow \infty$, it can be seen that

$$mE_q/(1 + E_q/E_D) < E_{sc}(90°) < mE_q. \qquad (3)$$

Fig. 4. Criteria for enhancement of steady state gain coefficient with applied electric field: E_0, applied field; E_q, limiting space-charge field; and E_D, diffusion field.

Equations (2) and (3) indicate that $E_{sc}(90°)$ will always increase with applied field; the amount of increase depends upon the relations between E_D, E_q, and E_0 shown in Fig. 4. As seen in that figure, when $E_q \gg E_D$, $E_{sc}(90°)$ is approximately mE_D at $E_0 = 0$ but increases to mE_q at large E_0. In this case, the application of an electric field can produce a substantial increase in $E_{sc}(90°)$. On the other hand, when $E_q \ll E_D$, $E_{sc}(90°)$ is approximately mE_q regardless of E_0. In this case, the application of an electric field produces a small change in $E_{sc}(90°)$.

To get some physical insight into the behavior of the gain coefficient it is useful to examine the amplitude of the 90° phase-shifted space-charge distribution with an applied field:

$$\rho_{sc} = mqN_{eff} \frac{E_D(E_q + E_D) + E_0^2}{(E_q + E_D)^2 + E_0^2} \qquad (4)$$

When $E_0 = 0$, the maximum allowed value of the space-charge density is $\rho_{sc} \approx mqN_{eff}$, which is also the limiting value for large E_0. If the diffusion is small ($E_D \ll E_q$) and no external field is applied, only a small amount of space-charge density (i.e., charge separation) is necessary to offset the diffusion. When an external field is present the amount of charge separation increases to balance both the diffusion force and E_0. Thus, a large variation in the space-charge density is obtained at $E_0 \gg E_q$. However, when the diffusion field is large compared with E_q, the space-charge density is already near maximum; therefore, an applied field cannot produce much more charge separation or a significantly higher space-charge field. This usually occurs at small Λ_g, i.e., large crossing angles.

The calculated increase in the gain for our Ce-doped SBN:60 sample with a ratio of $N_{eff}/\epsilon_r = 6 \times 10^{19}$ m^{-3} is shown in Fig. 5. Note that the functional dependence on applied field is similar for both extraordinary and ordinary light at these angles. In addition, Fig. 5 shows that the potential increase in gain is greatest at small crossing angles (large grating periods), although at very small crossing angles the field required to realize this increase may be quite large.

As can be seen from Figs. 1 and 2, in addition to a more intense beam fan, the application of an electric
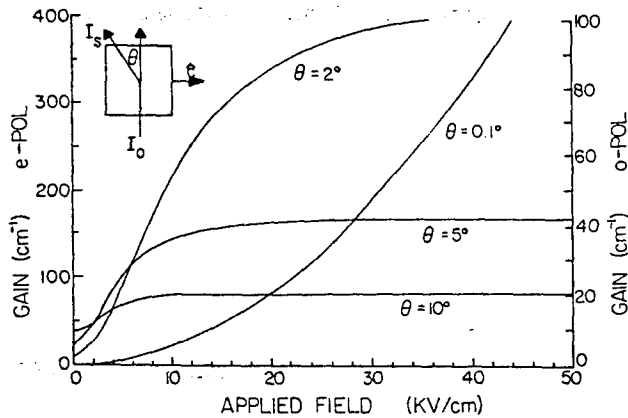
Fig. 5. Theoretical plots of coupling gain vs applied field for different crossing angles in Ce-SBN:60, for normal incidence. The left y-axis is for extraordinary polarized light and the right y-axis is for ordinary polarized light. The parameters used for this calculation are for crystal 3 of Ref. 8.

Fig. 7. Beam fanning with extraordinary polarized light and externally applied electric fields. The y-axis represents the intensity transmitted into an apertured detector.

Fig. 6. Criteria for change in response time with applied electric field: τ_I, optical excitation time; τ_{di}, dielectric relaxation time; τ_R, recombination time; τ_D, diffusion time; τ_E, drift time.

field has also significantly reduced the response time. The reason for this is seen by examination of the expression for the response time τ[12]:

$$\tau = \tau_I \frac{\left(\frac{1}{\tau_R}+\frac{1}{\tau_D}\right)^2 + \left(\frac{1}{\tau_E}\right)^2}{\left(\frac{\tau_I}{\tau_{di}}\frac{1}{\tau_R}+\frac{1}{\tau_D}\right)\left(\frac{1}{\tau_R}+\frac{1}{\tau_D}\right) + \left(\frac{1}{\tau_E}\right)^2}, \quad (5)$$

where $\tau_I = N_{eff}(h\nu/\alpha I_0)$ is the optical excitation time, $\tau_{di} = \epsilon_0\epsilon_r/q\mu n_0$ is the dielectric relaxation time, $\tau_D = q\Lambda_g^2/4\pi^2\mu K_B T$ is the diffusion time, τ_R is the recombination time, $\tau_E = \Lambda_g/2\pi\mu E_0$ is the drift time, and $n_0 = N_{eff}\tau_R/\tau_I$. From the above expression we see that if τ_E is the shortest time in the problem, the carriers reach their equilibrium position in time $\tau \approx \tau_I$. Note, however, that the response time can increase or decrease with the electric field applied depending upon the relations shown in Fig. 6. If $\tau_I < \tau_{di}$, the response time will be reduced with applied field; whereas if $\tau_I > \tau_{di}$, the response time will lengthen with applied field.

The physical reason that the response time gets faster is that the applied electric field increases the speed with which charges move to their equilibrium
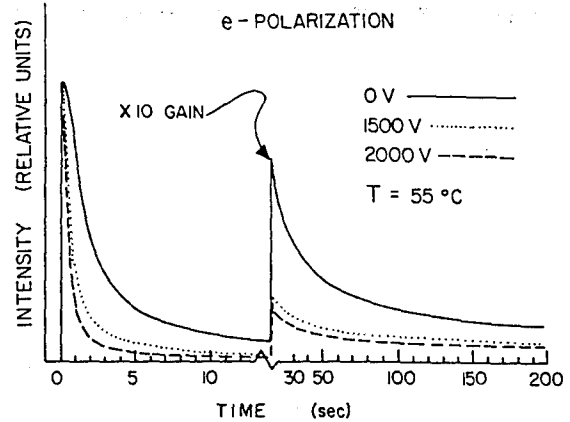
locations. If $\tau_I < \tau_{di}$ this reduces the number of retraps to zero and τ reaches a limiting time of τ_I, the excitation time. When $\tau_I \gg \tau_{di}$, the transit time is already short compared with the excitation time. In this case, an applied field cannot decrease the response time because it is limited to the excitation time, but it will increase the amount of charge moved which lengthens the response time.

For our crystal, both μ and τ_R are unknown, making it difficult to compare τ_I with τ_{di}. Experimentally, however, the response time significantly decreases with applied field indicating that τ_I is smaller than τ_{di} in our crystals.

IV. Results

A. External Field

Electrodes were connected by the use of silver paste to the (001) crystal faces in order to apply an external voltage in a direction parallel (positive voltage) or antiparallel to the c-axis. Up to 2100 V (≈ 3.2 kV/cm) were applied. Figure 7 shows the on-axis transmission of an extraordinary polarized beam of light for various voltages applied and for the zero-field state. It can be seen that the transmission decreases much faster and to a lower level when a voltage is applied. A similar result was obtained using ordinary polarized light as seen in Fig. 8. In this figure the curves for positive voltages decrease much faster and deeper than the zero-field curve but then slowly increase to about the zero-field level. The slow recovery is due to compensation of the external field as freed photorefractive charges move to offset the field. This recovery did not occur if the laser beam was expanded to fill the crystal, because the freed charges would be neutralized at the electrodes.

Figure 8 also shows that when a field of −3 kV/cm (a potential of about −2 kV) was applied, no beam fanning was observed, indicating that the crystal had depoled. The degree of depoling depended on the amplitude of the negative voltage and the temperature; complete depoling (no beam fan) occurred around −2.5 kV/cm at room temperature and polarization re-
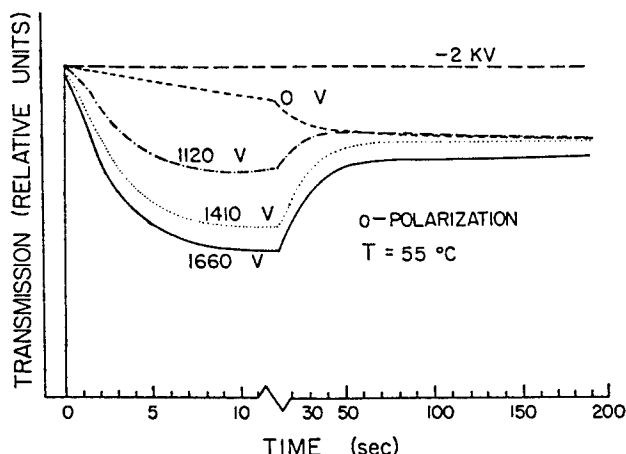
Fig. 8. Beam fanning with ordinary polarized light and externally applied electric fields. Positive fields are in the same direction as the poling field. The y-axis represents the intensity transmitted into an apertured detector.

versal (change in direction of fan) began around -3 kV/cm. It was found that the crystal could be repoled by application of about 3 kV/cm in the positive direction. These results are consistent with depolarizing fields reported by others.[13]

B. Pyroelectric Method

Enhanced photorefractive effects can also be observed by generating internal fields via temperature changes. These fields are caused by changes in the spontaneous polarization which occur whenever a ferroelectric crystal experiences a temperature change. This polarization change is due to pyroelectric currents and creates a field along the polar axis called the depolarizing field. This field is not normally encountered in photorefractive experiments because of a compensating field created by internal or external neutralizing charges. However, the depolarizing field may be observed if the temperature is changed faster than the response of the compensating field. Figure 9 shows how such an internal field can be formed with the assumption that the compensation field changes much slower than the spontaneous polarization. At $T_{initial}$ the depolarizing field, E_{DP}, is balanced by the compensating field, E_C, such that the crystal contains zero net field. As the temperature is lowered the spontaneous polarization (and consequently the depolarizing field) increases faster than the compensating field and generates a net field in the direction of the depolarizing field at the lower temperature, T_{low}. The opposite of this process occurs when the temperature is raised from $T_{initial}$; this produces a net field in the direction of the compensating field. Note that this reversal of the pyroelectric current will cause a polarization field to disappear for a complete cycling of the temperature if no compensating charges are allowed to form.

The magnitude of the internal field generated by changing the temperature was estimated by use of[13,14]:
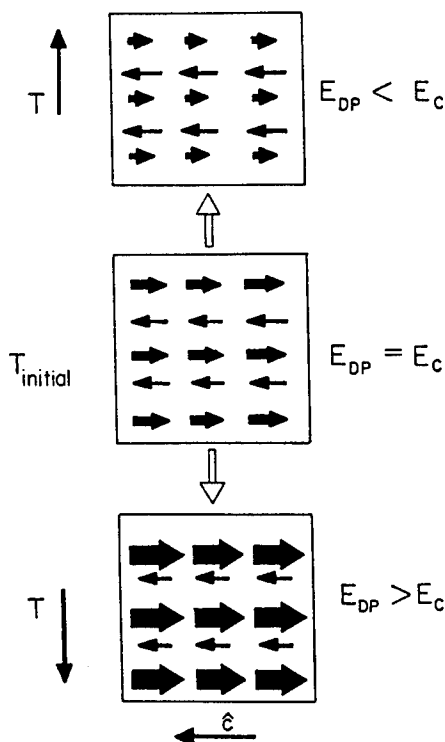
$$E_0 = [P(T_f) - P(T_i)]/\epsilon_{rf}\epsilon_0, \tag{6}$$

Fig. 9. Self-generated fields via the pyroelectric method. At $T_{initial}$ the crystal is neutral and the compensating field, E_C ($\leftarrow$), balances the depolarizing field, E_{DP} ($\rightarrow$). As the temperature is raised/lowered the depolarizing field decreases/increases such that a net field is produced in the crystal at the final temperature.

where $P(T)$ is the temperature dependent spontaneous polarization, T_i and T_f are the initial and final temperatures, and ϵ_{rf} is the relative dielectric constant at the final temperature. These calculations show that fields of up to 1000 V/cm/°C can be generated in SBN and BSKNN crystals over the temperature ranges of our ovens. For verification, a Keithley 610C Electrometer and a high impedance (10^{12} ohms) voltage divider were used to measure the voltage generated across our SBN crystal. The crystal was shorted before each run to insure a zero-field initial condition. As the temperature was increased the voltage would rise to a maximum, then fall at a much slower rate as external charges in the air started to compensate the pyroelectric field. About 5 kV (7.7 kV/cm) was measured for a temperature rise from 30–60°C. Due to capacitive loading of the measurement system and, to a lesser extent, the external compensation, this was somewhat less than that expected from direct calculation. However, the applied field measurements implied that this field was large enough to produce enhanced fanning effects.

The enhanced effects observed after raising the temperature are shown in Fig. 10 for ordinary light. For this figure the measured voltages were the same as those shown in Fig. 8 for externally applied fields. The small discrepancies between Figs. 8 and 10 can be attributed to different internal compensation mecha-
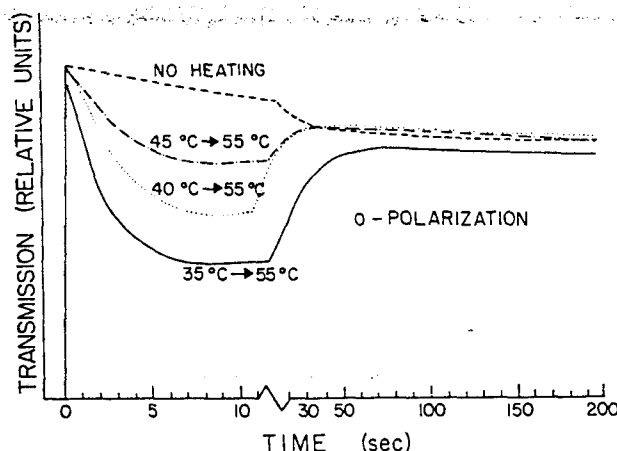
Fig. 10. Beam fanning with ordinary polarized light and self-generated electric fields via the pyroelectric method. The measurements were all made at 55°C.
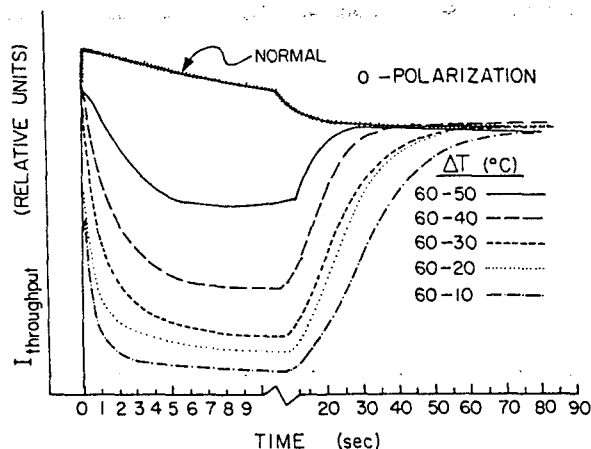

Fig. 11. Beam fanning with ordinary polarized light and self-generated electric fields via the thermal cycle method. The measurements were all made at an equilibrium temperature of 60°C.

nisms. Enhanced effects, similar to Fig. 7, were also seen for extraordinary light after raising the temperature.

On the other hand, lowering the temperature produced only a small enhancement. In conjunction, voltage measurements revealed smaller increases in the internal polarization upon cooling than upon heating over the same temperature range, contrary to that predicted by calculation. The measured voltage on cooling would increase to a value of ~1 kV and then dramatically slow down and level off. This was in sharp contrast with the continuously rising voltage observed when warming the crystal over the same range. In addition, the magnitude of the beam fan at the lower temperature, obtained by shorting the crystal after it reached thermal equilibrium, was less than that observed if the crystal was shorted continuously as the temperature was lowered. Together these observations indicate that as the temperature of the crystal is lowered a spontaneous polarization develops which becomes partially compensated by the flipping of domains at about 1.5 kV/cm; i.e., the depolarizing field starts to depole the crystal. Therefore, the field generated across the crystal during cooling is limited by the depoling field to 1–2 kV/cm.

C. Thermal Cycle Method

Enhanced beam fanning was also observed after the crystal was first prepared by thermal cycling in the presence of laser radiation. In the thermal cycle method, the crystal is cooled with laser light incident on it and then warmed to its original temperature with no laser light. Electric fields generated by the thermal cycling method produced the enhanced results shown in Fig. 11. Similar to the previous results for ordinary polarized light (Figs. 8 & 10), the transmission initially decreases rapidly, then slowly increases as freed charges move to compensate the field. As seen in Fig. 11, the effect is more pronounced for a larger temperature cycle. Similar effects were also observed for extraordinary light.

The production of self-generated fields via the thermal cycle method can be explained with the help of Fig. 12. In what follows, laser light used to observe the beam fanning effect will be called the probe beam and light used to generate internal fields will be called the preparation beam (both beams had the same diameter and followed the same path). As the crystal was lowered in temperature from a neutral state, the depolarizing field increased throughout the crystal [Fig. 12(a–b)]. However, in the region of the preparation beam, photorefractive charges were liberated and induced to move to spatial locations, which compensated for the newly developed field. At the lowest temperature, the beam was switched off and the photorefractive charges became trapped; thus, the crystal contained a neutral area surrounded by an uncompensated depolarizing field [Fig. 12(c)]. When the crystal was warmed to its original temperature without light, the recently created depolarizing field disappeared, but the field generated by the trapped charge distribution remained [Fig. 12(d–e)]. When the probe beam was switched on, it propagated through a prepared crystal with a large internal electric field and enhanced beam fanning was observed. Note that this model requires that the photorefractive currents be much larger than the normal compensating currents.

The model is essentially the same when the depolarizing field becomes large enough to depole the crystal. When this occurs, the photorefractive compensating charges prevent depoling in the beam area as the temperature is lowered, but outside the beam area depoling and repoling occur over the thermal cycle. At the final temperature, the fields generated by trapped charges persist and produce enhanced fanning. However, depoling prevented large fields from being created when the cycle was reversed, i.e., enhanced effects were negligible when the crystal was taken from a low temperature to a high temperature with light and returned to the low temperature without light. For this case, depoling limited the field to ~1.5 kV/cm in the region traversed by the beam.
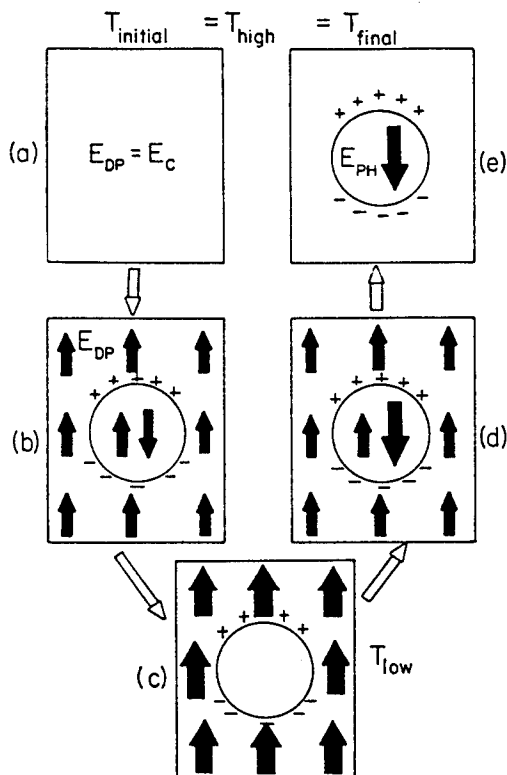
Fig. 12. Thermal cycle method of producing internal electric fields (the c-axis points down in this figure): (a) neutral crystal at $T_{initial}$; (b) development of a photorefractive field (E_{PH}, ↓) in the beam area and a net depolarizing field (E_{DP}, ↑) throughout the crystal as the temperature is lowered with a preparation beam; (c) neutral area in volume traversed by the preparation beam surrounded by strong depolarizing field; (d) depolarizing field decreases as temperature is raised with preparation beam off; (e) at final temperature the depolarizing field is again balanced by the compensation field (E_C), but the field of the trapped photorefractive charges remains.
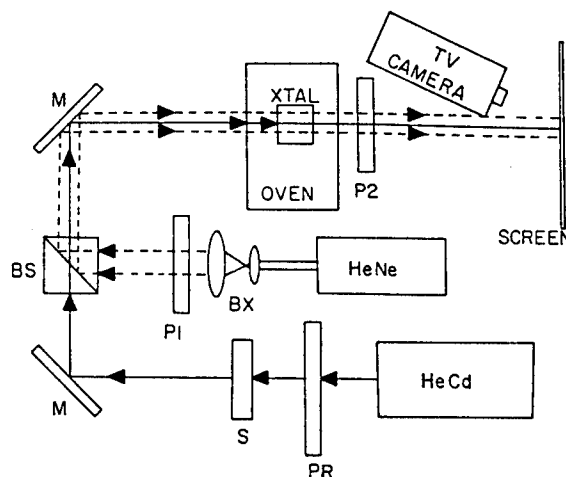

Fig. 13. Apparatus used to view crystal birefringence: PR, polarization rotator; S, shutter; M, mirror; BS, beam splitter; BX, beam expander; P1 and P2, polarizer and analyzer combination.

This model of thermal cycling is supported by observation of birefringent fringes during the thermal cycle. This was seen by aligning an expanded He–Ne beam with a He–Cd preparation beam as shown in Fig. 13. The He–Ne beam was polarized at 45° to the c-axis and an analyzer was used to create birefringent patterns on the screen. This technique yielded clear indications of temperature changes, temperature gradients, and temperature equilibrium. More importantly, areas in the crystal, which were under strong electric fields, created a discernible fringe pattern as the field-induced index change rotated the polarization of the light and produced spatial changes in the transmission of the He–Ne beam through the analyzer.

Photographs of the fringe pattern during the thermal cycle are shown in Fig. 14 for a BSKNN crystal. These photographs correspond to the drawings in Fig. 12. Figure 14(a) shows the crystal in thermal equilibrium at $T_{initial}$. The light and dark vertical fringes are due to changes in the crystal thickness. In Fig. 14(b), the temperature of the hot plate was lowered and temperature gradients were observed as horizontal fringes. These gradient fringes were caused by the temperature

dependence of the crystal birefringence. These fringes would move from bottom to top until thermal equilibrium was reached. During this stage of the cycle, the area containing the preparation beam became apparent as the electric field became different in this region. At the low temperature, the beam region was clearly noticeable [Fig. 14(c)] and the horizontal gradient fringes spread out at thermal equilibrium. Upon raising the temperature, the gradient fringes reappeared and additional lines appeared above and below the beam area [Fig. 14(d)]. At the final temperature [Fig. 14(e)] the lines above and below the beam area were distinct and resembled a dipole field pattern. Direct visual observation at this point revealed a dark spot in the area of the beam. This was apparently due to the creation of an index change by the strong electric field in this region. Upon application of the probe beam, the dark area would gradually become bright as photorefractive currents compensated the thermal cycle field (Fig. 15).

Optical birefringence was also used to show that the influence of the internal field was primarily in the bulk of the crystal and not a surface phenomenon. This was seen by directing the expanded He–Ne beam along the [010] crystal direction. After the crystal was cycled in temperature, the region traversed by the preparation beam was clearly evident through the analyzer, an indication that the field existed internally from the front to the back of the crystal.

V. Discussion

For all three methods used to produce enhanced beam fanning, the response time of the decrease in transmission was slower for longer wavelengths and for lower probe beam intensities (similar to normal, zero-field beam fanning). In particular, using the He–Ne probe beam showed similar but slower enhanced effects than for the He–Cd probe beam. Also, decreasing the probe intensity by an order of magnitude yielded an order of magnitude slower response time. In the
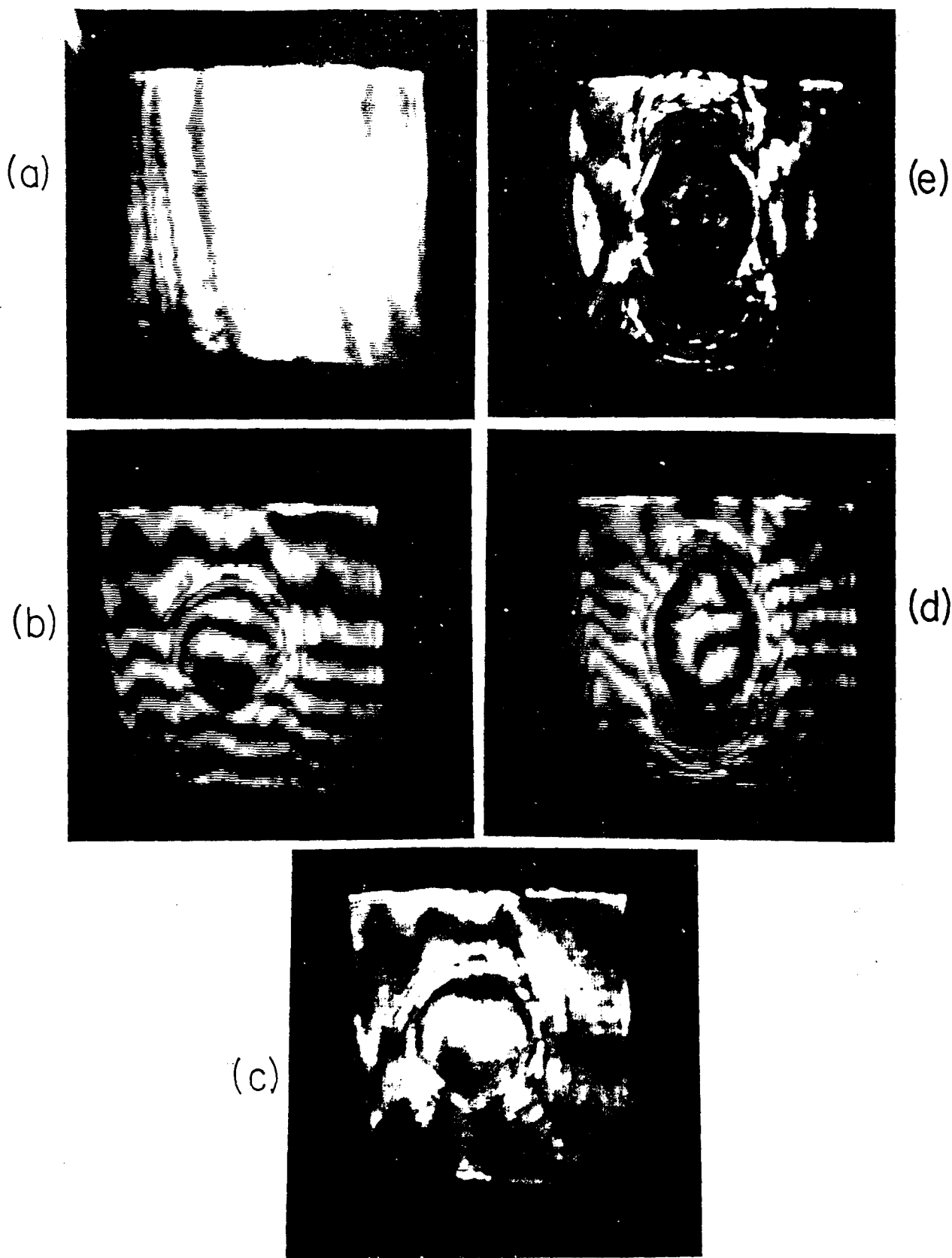
Fig. 14. Birefringent fringes observed during thermal cycling in BSKNN (the c-axis runs from top to bottom): (a) neutral crystal at thermal equilibrium—vertical fringes denote different crystal thicknesses; (b) as the temperature is lowered—horizontal fringes denote temperature gradients; (c) thermal equilibrium at T —the center spot marks the area of the preparation beam; (d) as the temperature is raised without light—area of prior preparation beam becomes more distinct; (e) thermal equilibrium at T_{final}—fringes suggesting field patterns created by trapped photorefractive charges are evident above and below the center spot—the thermal cycle is now complete and the crystal is in the prepared state.

Fig. 15. Birefringent fringes after application of probe beam. Erasure of the dark central spot occurs as photorefractive charges begin to neutralize the field.

thermal cycle method, the intensity of the preparation beam had little effect on the enhancement above intensities of ≈ 0.01 W/cm^2. Below this intensity the enhancement began to decrease. The effect was also independent of the speed at which the crystal thermally cycled, at least for the rates available with our ovens. For example, the observed response was similar whether the crystal was cycled 60°C in 60 min or in 4 min.

Enhanced beam fanning was seen in several photorefractive crystals, including SBN:60, SBN:75, BSKNN II, BSKNN III, and BaTiO$_3$. Enhanced effects could be seen in BaTiO$_3$ only with an externally applied field, as large electric fields were not observed with reasonable temperature changes in our sample. Several different crystals of Ce-SBN:60 were examined, each of which had different dark currents. It was found that the enhancement was greater for low values of the dark current as might be expected.

In general, the results were similar for both ovens when the crystals were prepared by the pyroelectric method or the thermal cycle method. One notable exception occurred when there was a large delay between the temperature changes and the initiation of the probe beam. For large delays (>10 min) the fields/effects were diminished in the open air oven because of compensating charges provided by the air in the room. In the Inrad oven, with a dry air atmosphere, the fields persisted for several days in crystals with low dark currents.

VI. Conclusions

There are several reasons why the experimental results reported here are significant. First, while most applications for photorefractive materials demand high speed and gain, very few, if any, are presently considered able to meet both requirements. The experiments reported here achieve at least an order of magnitude increase in both speed and gain. Second, while several crystals have demonstrated strong photorefractive effects using extraordinary polarized light, there are no crystals available which have performed well for both ordinary and extraordinary polarized light. The experimental results described here are achievable for either or both polarizations. Third, previous studies on the effect of temperature on gain and response time have not noted the potential role of large self-generated internal electric fields. Although temperature changes can directly alter the photorefractive gain and response time via changes in the dielectric constant, electrooptic coefficient, and dark current, they can also produce even larger effects indirectly through the action of a large self-generated internal electric field. Consequently, it becomes necessary to separate out the direct from the indirect changes to correctly identify the role each one plays in modifying the crystal behavior. Fourth, while experiments have indicated that application of electric fields can result in the poling or depoling of a photorefractive crystal at temperatures well below their Curie temperature (T_c) no studies have noted that the electric fields generated from temperature change alone could depole or pole a crystal. The experiments reported here show that, at temperatures below T_c, lowering the crystal temperature can result in crystal depoling. These results point out that the space-charge field itself may be of sufficient magnitude to cause depoling and limit the achievable performance in a given material.

References

1. J. Feinberg, "Asymmetric Self-Defocusing of an Optical Beam from the Photorefractive Effect," J. Opt. Soc. Am. 72, 46–51 (1982).
2. J. Feinberg, D. Heiman, A. R. Tanguay, Jr., and R. W. Hellwarth, "Photorefractive Effects and Light-Induced Charge Migration in Barium Titanate," J. Appl. Phys. 51, 1297–1305 (1980).
3. M. D. Ewbank, "Mechanism for Photorefractive Phase Conjugation Using Incoherent Beams," Opt. Lett. 13, 47–49 (1988); "Incoherent beams sharing photorefractive holograms," in Digest of Topical Meeting on Photorefractive Materials, Effects and Devices (Optical Society of America, Washington, D.C., 1987), p. 179.
4. M. Cronin-Golomb and A. Yariv, "Optical Limiters Using Photorefractive Nonlinearities," J. Appl. Phys. 57, 4906–4910 (1985).
5. J. Ford, Y. Fainman, and S. Lee, "Time-Integrating Interferometry Using Photorefractive Fanout," Opt. Lett. 13, 856–858 (1988).
6. J. Feinberg, "Self-Pumped, Continuous-Wave Phase Conjugator Using Internal Reflection," Opt. Lett. 7, 486–488 (1982).
7. G. J. Salamo, M. J. Miller, W. W. Clark III, G. L. Wood, E. J. Sharp, and R. R. Neurgaonkar, "Double Phase Conjugation in Strontium Barium Niobate," OSA 1988 Annual Meeting Technical Digest, FL5, in press.
8. G. L. Wood, W. W. Clark III, M. J. Miller, E. J. Sharp, G. J. Salamo, R. R. Neurgaonkar, "Broadband Photorefractive Properties and Self-Pumped Phase Conjugation in Ce-SBN:60," IEEE J. Quantum Electron. QE-23, 2126-2135 (1987).
9. G. C. Valley, "Competition Between Forward- and Backward-Stimulated Photorefractive Scattering in BaTiO$_3$," J. Opt. Soc. Am. B 4, 14–19 (1987); Errata, J. Opt. Soc. Am. B 4, 934 (1987).

10. F. P. Strohkendl, J. M. C. Jonathan, and R. W. Hellwarth, "Hole-Electron Competition in Photorefractive Gratings," Opt. Lett. 11, 312–314 (1986).

11. N. V. Kukhtarev, "Kinetics of Hologram Recording and Erasure in Electrooptic Crystals," Sov. Tech. Phys. Lett. 2, 438–440 (1976).

12. G. C. Valley and M. B. Klein, "Optimal Properties of Photorefractive Materials for Optical Data Processing," Opt. Engr. 22, 704–711 (1983).

13. J. R. Oliver, R. R. Neurgaonkar, and L. E. Cross, "A Thermodynamic Phenomenology for Ferroelectric Tungsten Bronze $Sr_{0.6}Ba_{0.4}Nb_2O_6$ (SBN:60)," J. Appl. Phys. 64, 37–47 (1988).

14. R. R. Neurgaonkar, W. K. Cory, J. R. Oliver, W. W. Clark III, G. L. Wood, M. J. Miller, E. J. Sharp, "Growth and Ferroelectric Properties of Tungsten Bronze $Ba_{2-x}Sr_xK_{1-y}Na_yNb_5O_{15}$ (BSKNN) Single Crystals," J. Cryst. Growth 84, 629–637 (1987).

Photorefractive self-focusing and defocusing as an optical limiter

Galen C. Duree Jr. and Gregory J. Salamo

University of Arkansas
Physics Department
Fayetteville, Arkansas 72701

Mordechai Segev and Amnon Yariv

California Institute of Technology
Department of Applied Phyiscs
Pasadena, California 91125

Edward J. Sharp

Army Research Laboratory
Fort Belvoir, Virginia 22060

and

Ratnakar R. Neurgankar

Rockwell International Science Center
Thousand Oaks, California 91360

ABSTRACT

Focusing and defocusing of laser light has been observed for many years. Optical Kerr type materials exhibit this effect only for high intensities. We show experimental evidence that photorefractive materials can also produce dramatic focusing and defocusing. Whereas Kerr materials produce this effect for high intensities, photorefractive materials produce these effects independent of intensity indicating that this effect would be ideal for an optical limiter. We compare the characteristics of Kerr and photorefractive materials, discuss the physical models for both materials and present experimental evidence for photorefractive defocusing. Self-focusing and defocusing was observed for any incident polarization although the effect was more pronounced using extraordinary polarized light. In addition, self-focusing or defocusing could be observed depending on the direction of the applied electric field. When the applied field was in the same direction as the crystal spontaneous polarization, focusing was observed. When the applied field was opposite the material spontaneous polarization, the incident laser light was dramatically defocused.

INTRODUCTION

One of the attractive features of laser light is that it can be focused to a very small spot. While a small, intense laser spot has found many useful applications, it is this same feature which makes laser light dangerous to the eye and to optical sensors in general. One class of materials which has been proposed to limit the transmission of high intensity laser light are Kerr materials. Optical limiters based on the use of optical Kerr materials take advantage of the fact that these materials exhibit an intensity dependent refractive index given by

$$n = n_0 + n_2 I \qquad (1)$$

where n_0 and n_2 are material constants. Since the incident laser beam usually has a near Gaussian intensity profile, the index of refraction of the material mimic the beam and possesses a Gaussian profile as well as shown in Figure 1. In this case n_2 is assumed positive. The result is that the laser beam itself induces a lensing effect which in this case focuses the laser beam in much the same way that a converging lens focuses a laser beam. If on the other hand the material chosen has a material constant n_2 which is negative then the laser beam would induce a defocusing effect and affect the beam in a manner similar to a diverging lens.
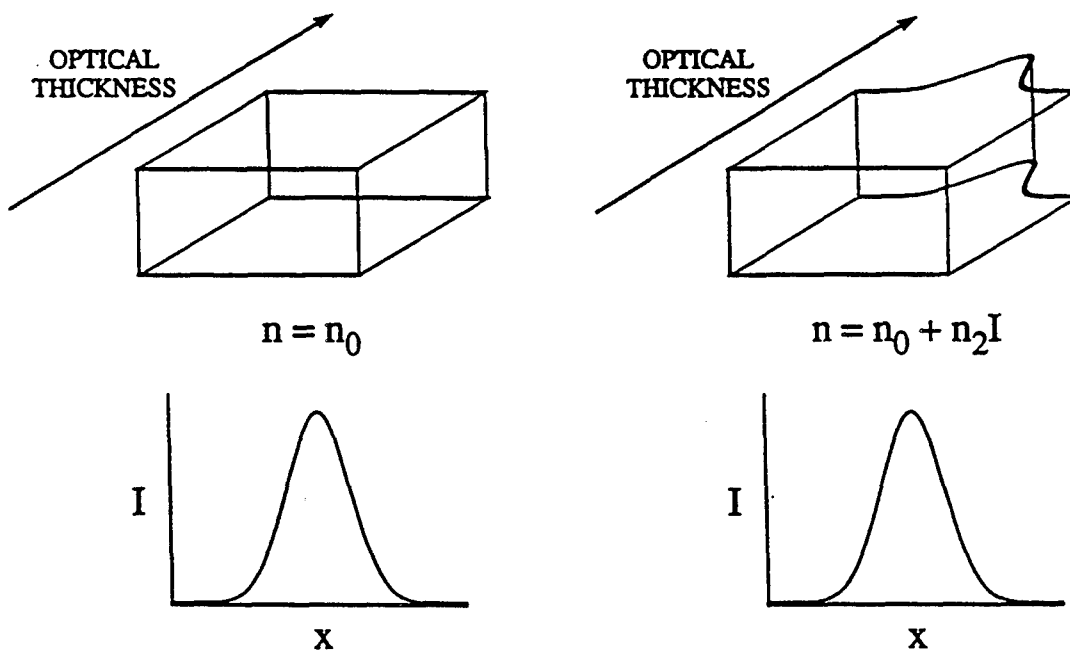

Figure 1. Simulation showing intensity dependent index.

While the Kerr limiter can be effective, it does suffer from two important difficulties. First, the laser intensity required before a significant value of $n_2 I$ can develop is extremely high and is generally on the order of megawatts per square centimeter (MW/cm^2). Since even milliwatts per square centimeter (mW/cm^2) continuous wave beams are dangerous to optical sensors, Kerr materials have restricted application. Second, once an index change $n_2 I$ is induced it affects all light passing through the material. This means that normal vision by the optical sensor does not

continue as long as laser light passes through it. These two restrictions make the Kerr limiter less than ideal.

PHOTOREFRACTIVE FOCUSING AND DEFOCUSING

In this paper, we present a new class of materials which produce dramatic focusing and defocusing effects[1]. These materials produce the same degree of focusing or defocusing independent of the incident intensity and produce an index change which only affects light of the same wavelength at propagation direction of the incident laser light. This class of materials, photorefractives, can potentially limit laser light of any intensity while maintaining normal vision through the material. Photorefractives would, therefore, appear to be a near optimal class of materials. There is, however, one difficulty with photorefractives. These materials have a much slower response than Kerr materials which are near instantaneous. Fortunately, this difficulty is not insurmountable. By simply reducing the incident laser light to a small spot at the material, sufficient intensities can be generated to produce the needed response time. For example, a typical response time for photorefractives is 0.1 s for an incident power of 1 W in a 1 centimeter diameter beam. If this beam is focused to a 100 μm spot the intensity in the material rises to 10^4 W/cm^2. Since the photorefractive response time is inversely proportional to the incident intensity this gives a response time of 10 μs. With a response time of 10 μs for an incident beam of 1 W in power, only 10 μJ are transmitted before focusing and defocusing are switched on. Since the photorefractive response time scales as the inverse of the intensity, 10 μJ is the amount of energy transmitted before focusing or defocusing is completed, independent of the incident power. That is, if P is the power of the incident beam and A its cross sectional area the energy transmitted through the limiters is

$$E = \int_0^\infty P_0 e^{-t/\tau} dt = C = cons \tan t \qquad (2)$$

using $\tau = C/P_0$. For powers below 1 W the response time is longer than 10 μs, but the energy transfer per unit time is lower. The result is that 10 μJ is transmitted during the time that focusing or defocusing is developing. Likewise, for powers above 1 W the response time is faster than 10 μs, but the energy transfer per unit time is higher. As a result, 10 μJ is again the energy transmitted before focusing-defocusing is completed. In addition to reducing the incident spot size there are also other parameters which reduce the photorefractive response time. On the whole, therefore, photorefractives have the potential to act as the ideal defocusing or focusing device or corresponding optical limiter.

PHYSICAL MODEL

As in the case of Kerr focusing and defocusing, photorefractive focusing and defocusing can also be physically understood. To illustrate the photorefractive effect, we can first consider two plane waves of light overlapping in a crystal producing an optical interference pattern as shown in Figure 2. In the bright regions of the interference pattern carriers are excited into the conduction band. The excited carriers then diffuse or drift and are finally trapped in the dark regions of the interference pattern. The resulting charge separation in turn generates a space charge electric field. The drift and diffusion process continues until equilibrium is reached where the diffusion or drift current is exactly balanced by the current generated by the induced space charge field. In this way the magnitude of the field is simply determined by the value necessary to balance

the diffusion or drift current. The space charge field can then distort the lattice and produce via the electro-optic effect an index change given by

$$\Delta n = \frac{n^3}{2} r_{eff} E_{sc}$$
(3)

where r_{eff} is the effective electro-optic coefficient of the material, E_{sc} is the induced space charge field, and n is the unperturbed index of refraction of the material.
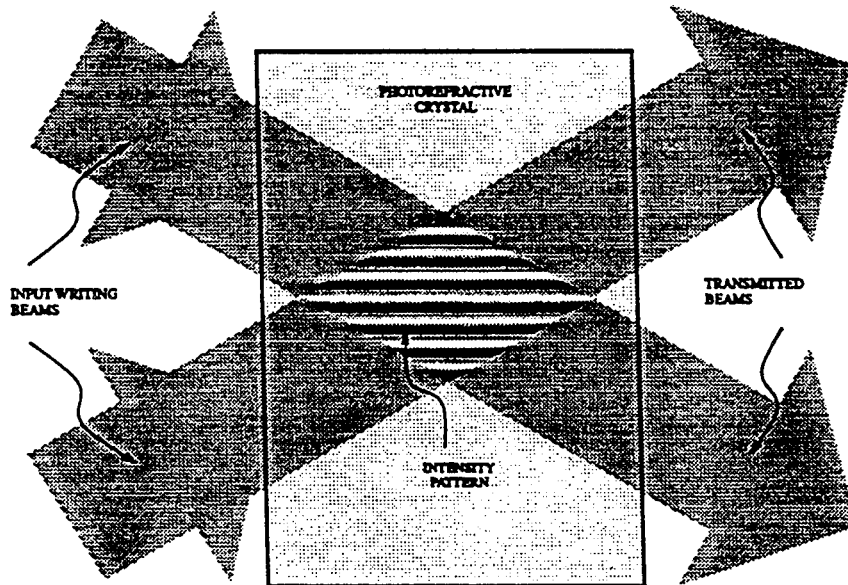

**Figure 2. Illustration for the formation of photorefractive gratings.**

The resulting induced index change can then be used in Maxwell's equation to predict the propagation behavior of the two overlapping laser beams. The result is that the induced index causes a coupling between the two beams which can be written as

$$\frac{dE_1}{dr_1} = i(\gamma_R + i\gamma_I) \frac{E_1 |E_2|^2}{I_0}$$
(4a)

$$\frac{dE_2}{dr_2} = i(\gamma_R - i\gamma_I) \frac{E_2 |E_1|^2}{I_0}$$
(4b)

where γ is the coupling coefficient and is determined by the material effective electro-optic coefficient and the magnitude of the laser-induced space charge field. The fact that γ has real and imaginary parts points out that the coupling between the two waves causes energy exchange between them and causes each of them to see a modified index of refraction.

In the physical picture we present here, we consider a propagating finite beam to be made up of Fourier plane-wave components. As shown in Figure 3(a) we can form a physical picture of diffraction that is based on "watching" each Fourier component propagating through the material. Since each component has a different k-vector projection along the propagation direction, the relative phase between Fourier components changes as a function of propagation distance z. Consequently, the sum of the Fourier components produces a different wave form at each z or propagation position. In the photorefractive picture each Fourier component produces an interference pattern with each and every other Fourier component. The result is that each component, therefore, "sees" a modified index of refraction which is determined by summing the index modification produced between a given Fourier component and every other component. When the low frequency Fourier components "see" a lower index than the higher frequency components due to the coupling, focusing is induced. (Fibure 3(b)) Likewise, when the low frequency components "see" a higher index than the higher frequency components, defocusing is induced (Figure 3(c)). In practice, the sign of the index change depends on the sign of an applied external field so that focusing is induced with an applied field along the c-axis direction while defocusing is produced with an applied field opposite the c-axis direction. One interesting possibility not discussed here occurs when diffraction is exactly compensated by photorefractive focusing. In this case, shape pursuing propagation or soliton formation is observed[2-5]. This picture neglects energy coupling which would result in an amplitude change of the Fourier components and would be important for a more complete analysis. In this paper the effect of energy coupling was minimized by the choice of input beam diameter, the value of applied field, and the time at which the measurement was made.
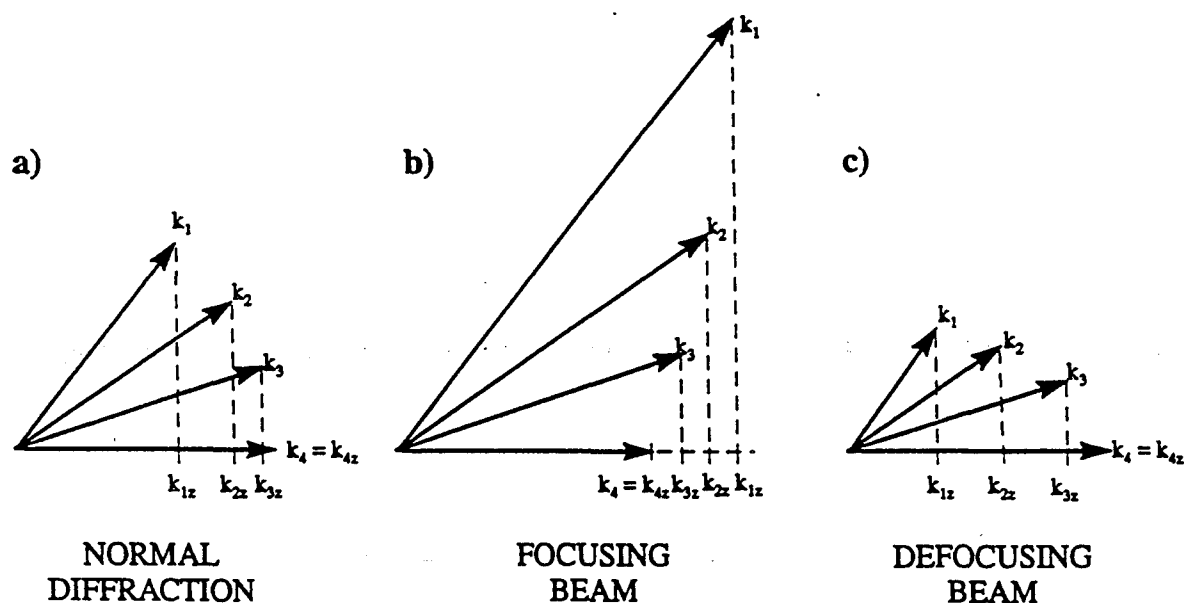
Figure 3. Wave-vector diagram of some of the Fourier components that make up a given laser spot showing what happens to the wave vectors as the beam passes through a photorefractive crystal with a) no voltage, b) an applied electric field parallel to the c-axis and c) an applied electric field anti-parallel to the c-axis.

the focusing lens. The imaging system, therefore, imaged the beam spot at the SBN entrance face with some magnification onto the detector array. As the imaging lens and the detector array are moved away from the SBN crystal, different cross sections of the Gaussian beam are then imaged onto the array. In this manner, the beam diameter at different locations throughout the SBN crystal was monitored. The magnification of the imaging system was determined by placing a thin aperture on the crystal exit (and entrance) face and imaging the aperture onto the detector array. Using the known value of the reference aperture, the magnification was determined to be about 15.6 and the positions of the exit and entrance faces of the SBN crystal were located. Using this information the horizontal cross section of the incident beam on the entrance and exit faces of the crystal was determined. Beam diameter and viergence data where taken at a time when these quantities reached a maximum value.
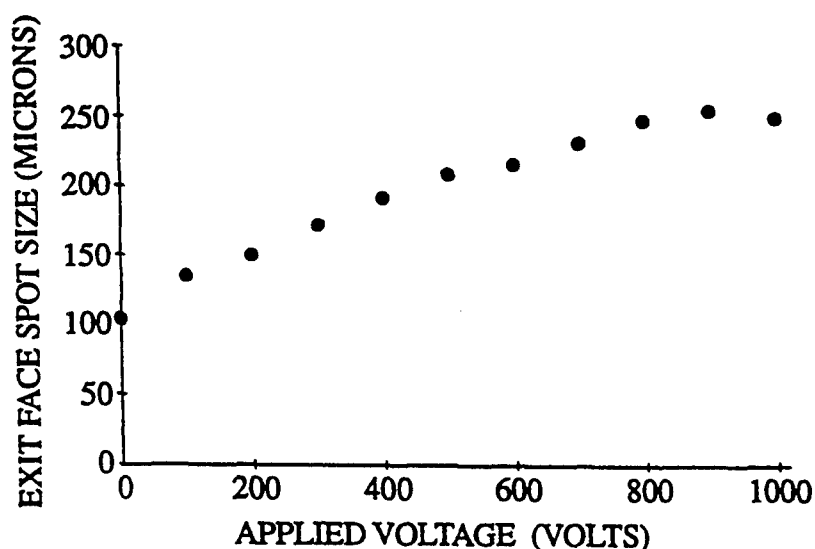

Figure 5. A graph showing the laser spot size diameter at the exit face of the crystal for different applied voltages.
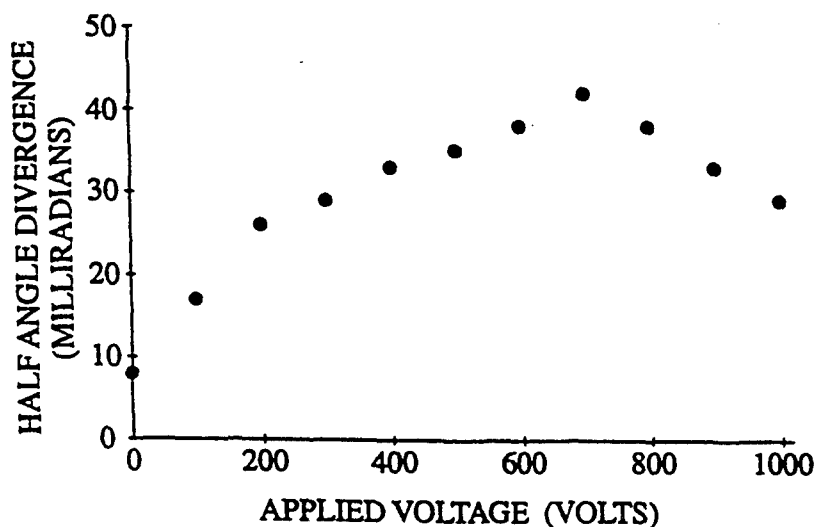

Figure 6. A graph showing the half angle divergence of the laser beam as it leaves the crystal with different applied voltages.

Figure 5 shows the effect of applied voltage on the exiting beam diameter while Figure 6 shows its effect on the divergence of the incident beam. As shown in these two figures the photorefractive defocusing is a dramatic effect. Similar results have been observed for focusing. Only the sign of the applied d.c. electric field was reversed when producing focusing or defocusing effects. Defocusing effects are seen when the field is opposite the c-axis direction.

CONCLUSION

In conclusion we have demonstrated that focusing and defocusing can be a dramatic effect in photorefractive crystals. This effect is also independent of the incident intensity, working at low intensities whereas the effects in Kerr matrerials are only present at high intensities. Both the focusing and defocusing effects were characterized for SBN:60 crystals. Similar results were found for all SBN samples as well as for BSKNN crystals. Photorefractive focusing and defocusing can now be investigated using traditional optical limiting geometries.

REFERENCES

1.   M. Segev, Y. Ophir, and B. Fischer, Appl. Phys. Lett. **56**, 1086 (1990).

2.   M. Segev, B. Crosignani, A. Yariv and B. Fischer, Phys. Rev. Lett. **68**, 923 (1992).

3.   B. Crosignani, M. Segev, D. Engin, P. DiPorto, A. Yariv and G. Salamo, J. Opt. Soc. Am. **B 10**, 446 (1993).

4.   G. Duree, J.L. Shultz, G. Salamo, M. Segev, A. Yariv, B. Crosignani, P. DiPorto, E. Sharp and R.R. Neurgaonkar, Phys. Rev. Lett. **71**, 533 (1993).

5.   M. Segev, A. Yariv, G. Salamo, G. Duree, J. Shultz, B. Crosignani, P. DiPorto and E. Sharp, Opt. & Phot. News **4**, 8 (1993).

Improved photorefractive time response using a cylindrical lens

Gregory J. Salamo, Brian D. Monson, William W. Clark III, Gary L. Wood, Edward J. Sharp, and Ratnakar R. Neurgaonkar

Experimental observations are reported which demonstrate that the response time for beam fanning, self-pumped phase conjugation, and double phase conjugation can be shortened by more than an order of magnitude without a significant reduction in coupling strength by using a cyclindrical lens to focus incident laser light into a photorefractive crystal. These results are compared with those obtained using a spherical lens where a reduction in the photorefractive response time is accompanied by a corresponding reduction in coupling strength. It is shown that the fidelity of a phase conjugate beam is not degraded when cylindrical optics are used.

I. Introduction

Over the last few years beam fanning,[1] self-pumped phase conjugation,[2] and double phase conjugation[3] have been demonstrated in photorefractive materials. While these effects are intriguing and have potential application, one of the noted drawbacks has been the slow time response associated with high gain materials.[4] The search for new materials and the modification of existing materials are two efforts currently being pursued to improve the response time.[5-7] For presently available materials, three other methods have been used: increased intensity,[8] higher temperature,[9,10] and applied electric fields.[11,12] This paper is an investigation of the use of higher laser intensities via focusing to improve the response time. In addition, the intensity distribution of the focused spot is used to maintain a high gain-length product.

Higher laser intensities decrease the response time by increasing the rate at which charges are excited in the illuminated areas in photorefractive crystals. Higher intensities can be achieved by turning up the laser power or by focusing the available laser light to a smaller spot. Both techniques produce faster photorefractive response times but not necessarily the same coupling strength. It will be shown that the use of a spherical lens to focus the incident beam to a tight waist decreases the response time but also decreases the magnitude of the photorefractive effect for processes involving beam fanning; however, the response time can be improved without decreasing the gain by focusing with a cylindrical lens. In particular, the photorefractive response times for beam fanning, self-pumped phase conjugation, and double phase conjugation were observed to improve by use of cylindrical focusing while maintaining approximately the original coupling strength.

In addition to response time, the fidelity of phase conjugate images produced by a self-pumped phase conjugate mirror based on cerium doped strontium barium niobate (Ce-SBN:60) was compared for the cases of spherically focused, cylindrically focused, and unfocused light. A fidelity of ~70 line pairs/mm was obtained in each case.

II. Physical Description of Beam Fanning

Beam fanning is a well known photorefractive phenomenon in which coherent light is scattered asymmetrically as it passes through a high gain crystal. The beam fan originates from conventional scattered light which crosses the incident beam and writes index gratings in the crystal via the photorefractive effect. As a result of these index gratings, energy is coupled from the incident beam into the weaker scattered beams, which can result in significant depletion of the incident beam. The magnitude of the coupling depends on the number of scatterers, the gain of the

Ratnakar R. Neurgaonkar is with Rockwell International Science Center, Thousand Oaks, California 91360; G. J. Salamo and B. D. Monson are with University of Arkansas, Physics Department, Fayetteville, Arkansas 72701; and the other authors are with CECOM Center for Night Vision & Electro-Optics, Fort Belvoir, Virginia 22060-5677.
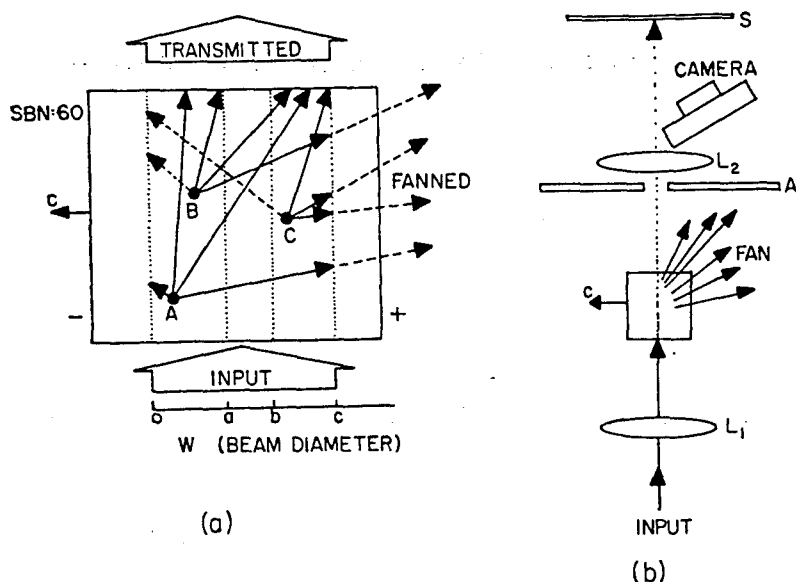Received 14 June 1990.

Fig. 1. (a) Laser beam of variable width propagating through a photorefractive crystal of thickness L. Weak scattered beams originating from crystal imperfections A, B, and C are shown crossing the input beam at different angles. (b) Experimental arrangement used to produce the photographs of Fig. 2: L, lens; S, shutter; A, aperture; and S, screen.

crystal, and the available length (interaction length) over which the incident beam and the scattered beams can interact. In the case of an unfocused beam the interaction length can typically be several millimeters long (i.e., of the order of a few beam waists). This interaction length does not change as the intensity is increased by turning up the laser power and an intensity dependence of approximately I^{-1} is typically observed for the beam fanning time response.[4] However, for a beam focused with a spherical lens the interaction length may be of the order of 50 μm or less. Beam fanning is almost absent for such small interaction lengths even though the time response still exhibits an I^{-1} intensity dependence. The improved time response achieved at the expense of strong coupling is generally not desirable for most photorefractive applications. The following examination of the beam fanning effect yields additional information and provides a way to avoid the decrease in coupling gain.

Figure 1(a) shows the top view of one plane of the illuminated crystal volume, which contains weakly scattered beams originating, for example, from crystal imperfections. For the sake of clarity only three scattering centers and a few of the many scattered beams are shown in the plane depicted in Fig. 1(a). This same process, however, occurs over the entire volume of the crystal occupied by the input beam. The resulting scattered waves and the input wave form a multitude of interaction regions where two-beam coupling occurs. Since the scattered beams cross the incident beam at different angles, both the gain and the interaction length are different for each ray. The amount of energy coupled out of the incident beam depends on the gain-length product associated with each of the scattered beams as well as the total number of scattered beams.

The gain depends on the polarization and propagation direction of the scattered beams relative to the electrooptic (EO) coefficients. For the following dis-

cussion it will be assumed that the gain is strongest for extraordinary rays which form gratings parallel to the c-axis (similar to SBN). However, at very small crossing angles ($\theta \leq 2°$) the gain is weak.[13] Thus, for the plane in Fig. 1(a), the gain will be strongest for (extraordinary) scattered rays at moderate crossing angles ($\theta \sim 5°$) to the input beam. For this example it will be assumed that energy is coupled in the direction of the positive c-face [to the right in Fig. 1(a)]. Rays which scatter to the left will couple their energy back into the main beam and not contribute to beam depletion.

The interaction length depends on the direction of the scattered ray as well as the spot size of the incident beam. Consider an incident beam with a diameter w as shown in Fig. 1(a). The interaction length is confined by either the beam waist or the back crystal face. If $w = a$, the beam will encounter two scattering centers (A and B), resulting in several low intensity scattered beams. If the beam is expanded to $w = b$ an increase in beam depletion will occur due to an increase in the interaction length for some of the rays scattered at A and B. If the input beam waist is increased again to $w = c$, the interaction length is made even longer, and, in addition, another scattering center is encountered which leads to even more beam depletion. According to this physical description, both the number of scattering centers and the effective interaction length are increased with a large spot size.

The above description suggests that less light will be coupled from the left side (the side nearest the negative c-face) of the input beam shown in Fig. 1(a) since there are fewer crossing beams traveling to the right. This was demonstrated by use of the beam fanning arrangement shown in Fig. 1(b). In this figure L_1 and L_2 are of a similar type (both spherical or both cylindrical) and produce a circular spot on the viewing card. Figures 2(a) and (b) show photographs for an unfocused beam and for a beam focused with a cylindrical

(a)
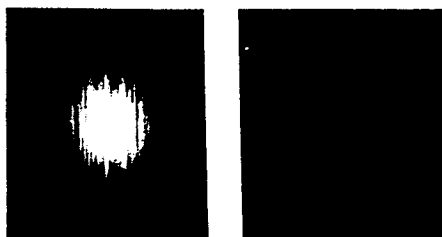
(b)
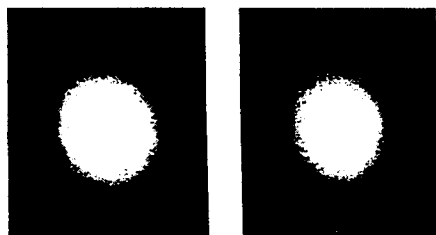
(c)

Fig. 2. Spatial distribution of an extraordinary polarized beam after passing through a cerium doped SBN:60 crystal to show the evolution of the beam depletion: (a) an unfocused beam before beam fanning has occurred, after a time comparable with the $1/e$ response time, and during the steady state; (b) a beam focused with a cylindrical lens before fanning and in the steady state; and (c) a beam focused with a spherical lens before beam fanning and in the steady state.
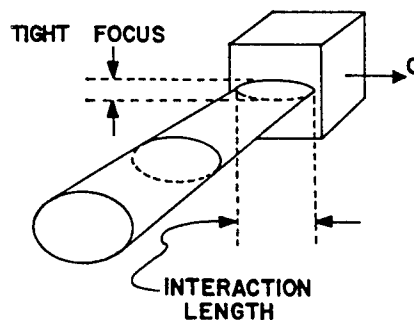

Fig. 3. Cross section of a beam focused by a cylindrical lens on the front face of a photorefractive crystal illustrating the tight focus in the dimension perpendicular to the crystal c-axis.

lens. In Fig. 2(a) the image of an unfocused extraordinary polarized beam which has passed through the Ce doped SBN:60 crystal is photographed at three different times after the onset of beam fanning to show the evolution of the beam depletion: (1) immediately after the shutter is opened, (2) after a time comparable with the $1/e$ response time, and (3) during steady state. Figure 2(b) shows the transmitted image before fanning and in steady state for a beam focused with a cylindrical lens. As can be seen from this figure the depletion of the input beam due to fanning can be significant. Steady state transmission as low as 0.1% (corresponding to optical density 3) has been measured for bean fanning with an unfocused beam and the same SBN:60 sample used in these photographs.[14]

Figure 2(c) shows the transmitted image before fanning and in the steady state for a beam focused with a spherical lens of 200-mm focal length. The amount of beam depletion is negligible in this case because only a

few scattering centers are encountered and the interaction lengths are small for the small spot size. The largest interaction length is virtually along the beam waist, but both the gain and scattering are small in this direction. As a result, the gain-length products are small and little beam depletion occurs for very small spot sizes.

The situation is different with a cylindrical lens which can produce faster response times without a reduction in coupling strength. This is because a cylindrical lens focuses in one dimension (see Fig. 3). It can, therefore, produce a tight focus in the dimension which has a small gain and still maintain a large interaction length in the other dimension. For example, in SBN the relevant EO coefficients are $r_{33} = 224 \times 10^{-12}$ m/V and $r_{13} = 55 \times 10^{-12}$ m/V, where r_{33} provides the maximum gain for extraordinary polarized beams propagating at near normal incidence to the c-axis (the grating wave vector parallel with the c-axis). As a result, the greatest beam depletion is achieved by combining the large gain associated with r_{33} and the large interaction length associated with the major axis of the elliptical beam spot produced by the cylindrical lens. The gain coefficient in the other direction is dominated by r_{13} and is small by comparison, so little is lost by having a tight focus in this direction. In the cylindrical focusing geometry the intensity is increased although not as much as the spherical lens case (i.e., πr_0^2 vs $\pi r_0 r$). However, the increase in intensity decreases the response time at no cost to beam depletion.

III. Experiment

A cw argon-ion laser oscillating at 476.5 nm was used to study the photorefractive time response in Ce doped SBN:60 as a function of intensity. The output beam was TEM_{00} and extraordinary polarized with respect to the crystal. The beam power was varied using a series of calibrated neutral density filters to permit a comparison of the intensity dependent time response for three experimental configurations: (1) an unfocused beam, (2) a beam focused with a cylindrical lens, and (3) a beam focused with a spherical lens. These experiments were carried out for photorefractive beam fanning, self-pumped phase conjugation, and double phase conjugation.
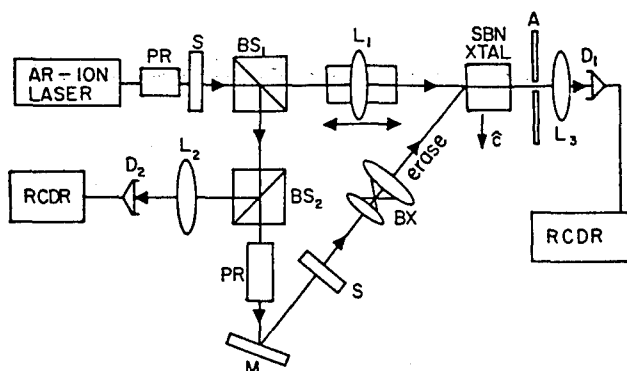
Fig. 4. Experimental arrangement for determining the response time for beam fanning: *PR*, polarization rotator; *S*, shutter; *BS*, beam splitter; *D*, detector; *L*, lens; *M*, mirror, *BX*, beam expander; *RCDR*, recorder. Lens L_1 is mounted on a translation stage.

Fig. 5. Relative transmission through a Ce doped SBN:60 crystal as a function of time for three focusing arrangements. The focused spot sizes $(FW1/e^2M)$ are: unfocused, 2.12 mm; cylindrically focused, 0.11×2.12 mm; and spherical focused, 0.10 mm.

Fig. 6. Plot of the characteristic beam fanning response time of Ce doped SBN:60 as a function of power. Triangles represent unfocused light, and squares represent light focused with a cylindrical lens. The intensity fitting parameters for $\tau = A(I/I_0)^{-b}$ are $A = 0.15$ (seconds) and $b = 1.01$ for the unfocused case and $A = 0.15$ (seconds) and $b = 1.02$ for the focused case.

Although power was the independent experimental variable, the response time curves were fit to an analytical expression involving intensity I:

$$\tau = A(I/I_0)^{-b},$$

where τ is the $1/e$ response time, $I_0 = 1$ W/cm^2, and A and b are the fitting parameters. The beam areas were determined by spot size measurements with an optical multichannel analyzer (OMA) except for tightly focused beams, in which case the Gaussian propagation analysis was used to calculate the spot sizes.

A. Beam Fanning

The experimental arrangement shown in Fig. 4 was used to determine the beam fanning response time for the three lens configurations. The decrease in transmission was monitored at detector D_1 as a function of time. A translation stage at L_1 was fitted with either a cylindrical or spherical lens or was left empty for the unfocused case. The arrangement of Fig. 4 also allowed for monitoring of the input beam and for grating erasure between measurements. The decrease in transmission is a measure of the photorefractive coupling strength, and the speed with which the transmission decreases is a measure of the photorefractive response time.

A comparison of the beam fanning response is shown in Fig. 5. In this figure the *c*-axis of the crystal is into the plane of the page and the beams are focused in the crystal. In these conditions there is virtually no beam fanning produced when focusing to a spot size of 0.1 mm $(FW1/e^2M)$ with a spherical lens. This comparison is somewhat striking since the unfocused spot size was 2.12 mm, and the cylindrical lens focused the beam to an elliptical spot with axes of 0.11×2.12 mm.

The response times vs power for unfocused and cylindrical focusing are compared in Fig. 6 for the same spot sizes used in the measurements of Fig. 5. The observed shortening of the response time (factor of 20) by the cylindrical lens compares well with the ratio of the areas of the focused and unfocused beams. In other words, the improvement in the time response obt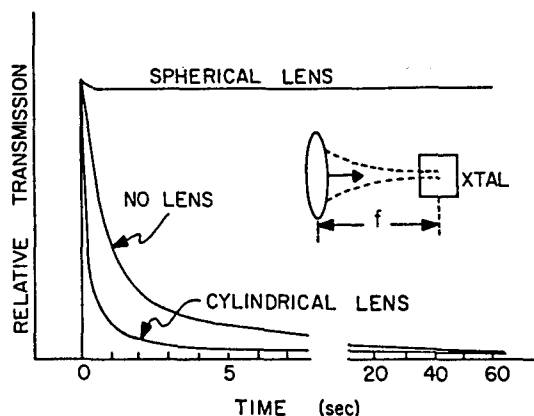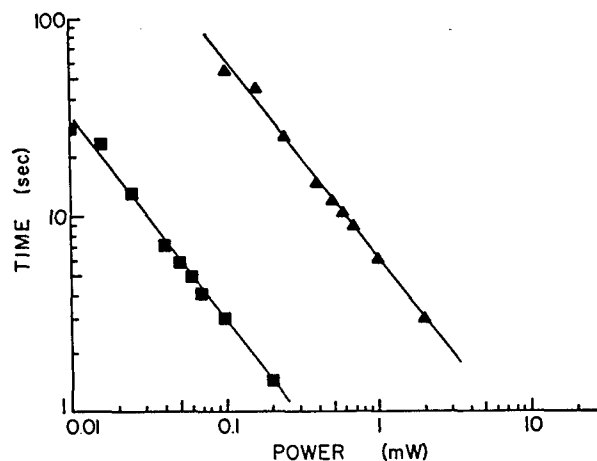ained for the cylindrical lens is just due to the increase in intensity achieved by reducing the spot size. The parameters A and b, given in the caption, were obtained from a least-squares fit to the data and agree well with previous measurements of the beam-fanning response time where an approximate I^{-1} intensity dependence was found for Ce doped SBN crystals.[4] The present measurements indicate that the I^{-1} intensity dependence of the time response is valid over at least 3 orders of intensity variation.

In another experiment, a spherical lens with a focal length of ~200 mm was used on the translation stage to change the spot size at the crystal face as shown in the diagram in Fig. 7. The relative transmission through the crystal is plotted against time for different values of L (lens to crystal distance). Initially, when the beam waist at the crystal is a minimum, there is virtually no beam fanning or reduction in transmission. As
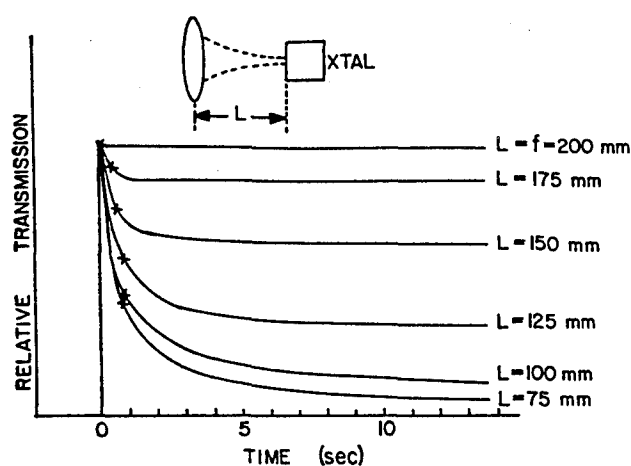
Fig. 7. Plot of the relative transmission through a Ce doped SBN:60 crystal as a function of time for a laser beam which has been focused with a 200-mm focal length spherical lens. Each curve corresponds to the response obtained when the crystal is positioned at different distances relative to the plane of the lens. The $1/e$ response times are marked for each curve. The $FW1/e^2M$ focal spot was 61 μm.

Fig. 9. Determination of the minimum beam waist location via photorefractive beam fanning. The relative spot size as determined with an OMA (circles) is compared to the beam fanning response time (squares) as a function of the distance D. The position of the minimums corresponds to the focal length of the lenses.
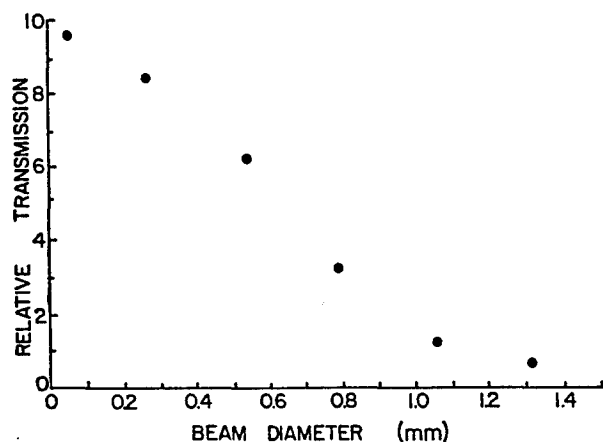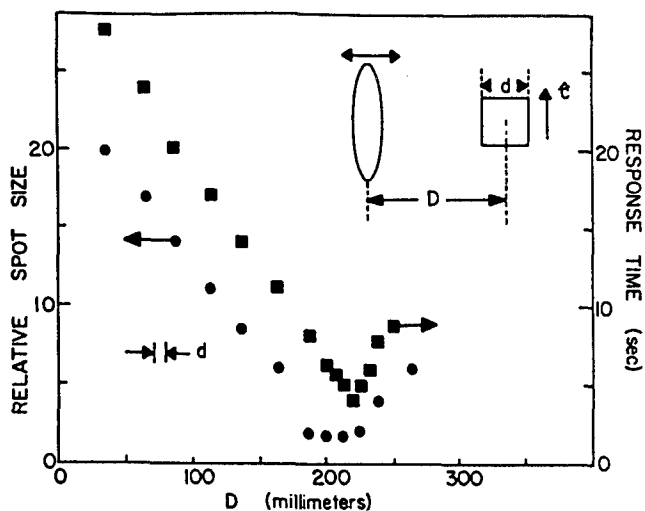

Fig. 8. Plot of the relative steady state transmission as a function of the e^{-2} spot diameter for the curves in Fig. 7.

the spot size on the front face of the crystal is increased (i.e., the intensity is decreased), the response time becomes slower. On the other hand, the steady state beam depletion becomes more significant. These observations are consistent with the explanation of beam fanning presented in connection with Fig. 1. In fact, the transmission in the steady state as a function of the $1/e^2$ beam diameter associated with the different distances from the 200-mm focal length lens decreases with increasing spot size as shown in Fig. 8.

The dramatic change in response time with spot size was used to determine the location of the minimum beam waist of a focused beam. These results are shown in Fig. 9 where they are compared to spot size measurements made with an OMA. The values of D correspond to the distance from the lens to the center of the crystal and are plotted against the measured

beam fanning response time. The dimension of the crystal d is indicated for comparison. Here the focal length of the lens is determined by finding the value of D, which corresponds to the minimum response time for photorefractive beam fanning. As seen, the response time is very sensitive to focal position. The offset between the minimum obtained with the OMA and that of the photorefractive technique in Fig. 9 is due to the relatively large pixel separation (25 μm) and the uncertainty of determining the position of the pixels in the OMA head.

Another method of determining the focal spot was to observe the change in the amount of beam fanning as the lens was translated. Near the focal spot the beam fan would disappear; i.e., the transmission would maximize. This technique is more convenient and timely than use of the OMA or measurement of the response time at different positions.

B. Self-Pumped Phase Conjugation

The time response of a self-pumped phase conjugate mirror was monitored and recorded for input beams at an oblique angle of incidence. The experimental setup used for these measurements is shown in Fig. 10. The phase conjugate signal was recorded at D_1 as a function of time for each value of the intensity. The magnitude of the reflected conjugate signal is a measure of the coupling strength, and the speed with which the conjugate signal forms is a measure of the response time.

The $1/e$ response time is plotted in Fig. 11 as a function of the corresonding beam power. The intensity dependence for the phase conjugate buildup is approximately I^{-1}, which agrees with earlier data[15] on SBN:60 but does not agree with data for SBN:75, BSKNN, and $BaTiO_3$.[4,15] The fitting parameters representing the best fit to these data for the three differ-
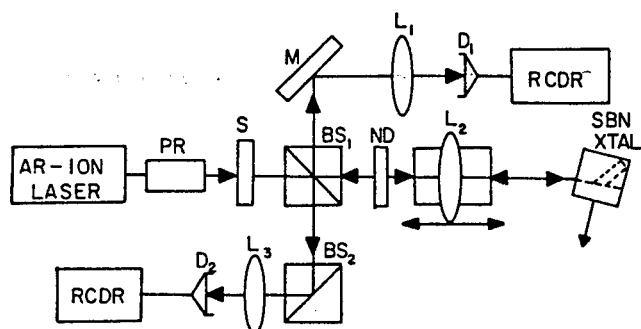
Fig. 10. Experimental arrangement for determining the phase conjugate buildup from a self-pumped phase conjugate mirror: PR, polarization rotator; S, shutter; BS, beam splitter; D, detector; L, lens; M, mirror; and RCDR, recorder. Lens L_2 is mounted on a translation stage.
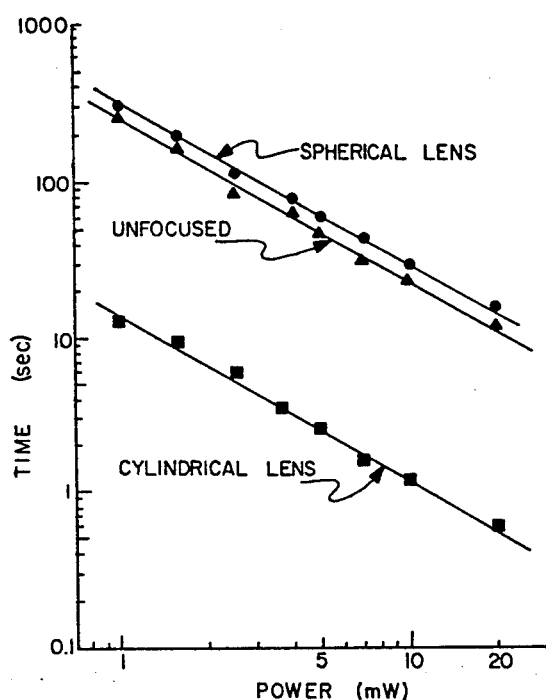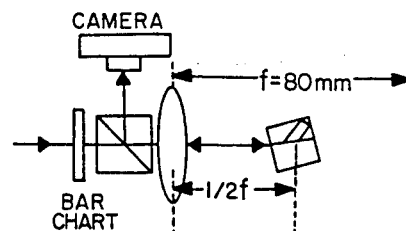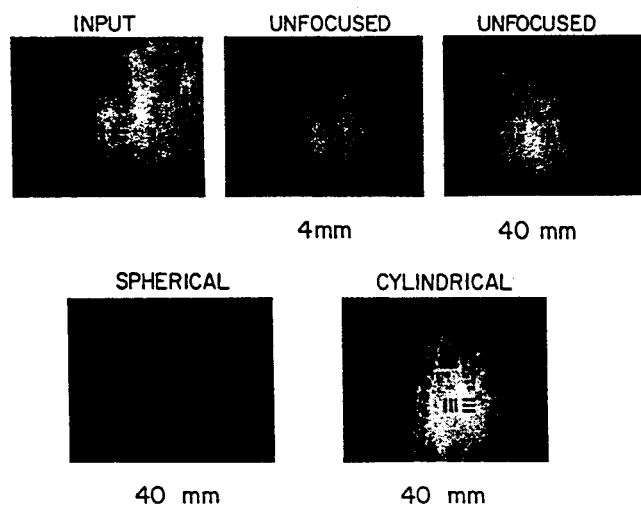

Fig. 11. Plot of the phase conjugate buildup time for a laser beam incident at 45° on a cerium doped SBN:60 crystal. An elliptical beam spot of dimensions of 2 × 2.2 mm ($FW1/e^2M$) was used for the unfocused case. For the spherical lens a focal length of 200 mm was used with the crystal positioned at approximately one-half of the focal length. For the cylindrical lens f = 200-mm lens with the crystal positioned at the focus. The intensity fitting parameters for $\tau = A(I/I_0)^{-b}$ are: unfocused, A = 5.0 s, b = 1.06; spherical focusing, A = 27 s, b = 0.98; cylindrical focusing, A = 10.0 s, b = 1.04.

(a)

(b)

Fig. 12. (a) Experimental arrangement used to test the fidelity of phase conjugate images produced by a self-pumped phase conjugate mirror. The lens was removed for the unfocused cases. (b) Input image and images formed by the phase conjugate beams for the crystal placed at the indicated distances from the lens.

ent focusing conditions are included in the caption of Fig. 11. The data indicate that when the cylindrical lens is used the phase conjugate response time is shortened by a factor of 20 over the unfocused case. Again, as in the case of beam fanning, this shortening follows the reduction in spot size for the focused beam. The measured phase conjugate reflectivity was 10% for both the cylindrical lens and the unfocused case, indi-

cating that the faster response time was achieved at little cost to the coupling strength.

The oblique angle of incidence was used to facilitate self-pumping. Since the beams were not incident perpendicular to the crystal face, the beam profile at the crystal was elliptical for all measurements and the horizontal spot size was increased by a geometrical factor in the intensity fit. The angle of incidence used for the unfocused case and the cylindrically focused case was 45°. To obtain a conjugate signal with the spherical lens it was necessary to place the crystal at about half of the focal length or to increase the angle of incidence. However, at large oblique angles the Fresnel losses at the crystal face prohibited performance comparable to the cylindrical lens case.

A comparison of the phase conjugate fidelity was carried out for the three focusing arrangements using a self-pumped phase conjugate mirror and an Air Force resolution chart. In the experimental setup shown in Fig. 12(a) the expanded laser beam bearing the resolution pattern was imaged into the crystal. The conjugate return for each case was photographed and is shown with the input for comparison in Fig. 12(b). For these demonstrations the crystal was placed at half
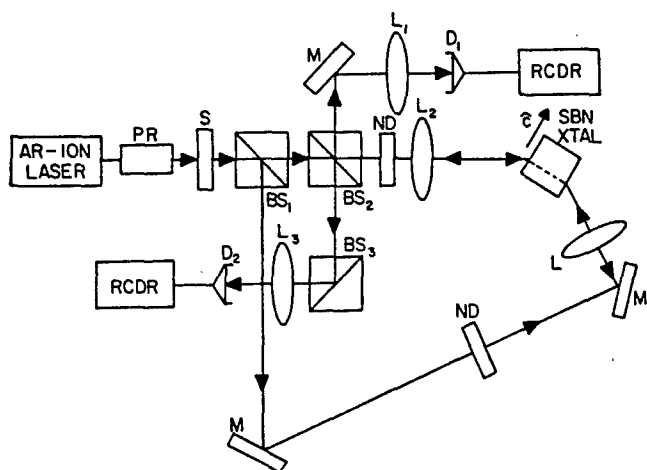
Fig. 13. Experimental arrangement used to determine the phase conjugate buildup time of an SBN:60 double phase conjugator: *PR*, polarization rotator; *S*, shutter; *BS*, beam splitter; *D*, detector; *L*, lens; *M*, mirror; *RCDR*, recorder. Both beams have equal intensity and equal angles of incidence (= 45°). L and L_2 are cylindrical lenses of 200-mm focal length and are removed for the unfocused case. A $FW1/e^2M$ beam spot of 2.12 × 3.00 mm was used for the unfocused case due to the oblique angle of incidence.
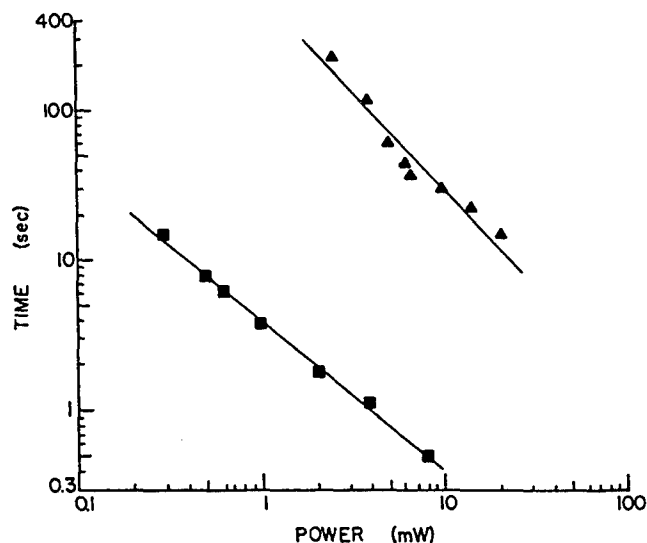

Fig. 14. Plot of the phase conjugate buildup time as a function of input power for the bridge conjugator shown in Fig. 13. Triangles represent unfocused light, and squares represent light focused with a cylindrical lens. The intensity fitting parameters for $\tau = A(I/I_0)^{-b}$ are: unfocused, $A = 5.7$ s; $b = 1.25$ and cylindrical focusing; $A = 3.0$ s, $b = 0.89$.

of the focal length of lens L (40 mm) for two reasons; first, self-pumping was not possible in our crystals using a spherical lens unless this condition was met, and, second, the high spatial frequencies of the image are filtered by the effective aperture introduced by the finite crystal dimensions when the crystal is placed in the transform plane. The resolution of the input image was ~100 line pairs/mm, and the resolution of the conjugates was ~70 line pairs/mm for all three cases with the crystal at half of the focal distance. About 80 line pairs/mm were obtained for an unfocused beam when the crystal was placed directly adjacent to the beam splitter.

C. Double Phase Conjugation

The experimental arrangement shown in Fig. 13 was used to examine the phase conjugation properties of a double phase conjugate mirror, the bridge conjugator.[16] Both input beams were extraordinary polarized and introduced into the crystal at equal angles of incidence ($\theta = 45°$). In this conjugator both conjugate beams build up simultaneously, although care was taken to maintain equal beam intensities for the two input beams for the power measurements. The results of these measurements are shown in Fig. 14 for unfocused beams and for beams focused with cylindrical lenses.

The conjugate signal buildup is ~2 orders of magnitude faster for the cylindrical lens case (squares). The intensity dependence of the time response for the unfocused and focused conditions is not the same for the bridge conjugator. However, the $I^{-1.25}$ dependence measured for the unfocused case is in good agreement with earlier data.[16] For the particular crystal used in this experiment a conjugate signal could not be ob-

tained for beam powers below 2.5 mW in the unfocused case.

The case of spherical focusing is not included in the double phase conjugator comparison because the double conjugator was difficult to start and maintain with very small beam diameters. For the bridge conjugator to operate there must be beam overlap from fanning, and for small spot sizes there is almost no fanning as illustrated in Figs. 2(c) and 5. In fact, double phase conjugation could only be achieved when the spherical lenses were brought in close proximity to the crystal (i.e., well within the focal length of the lenses) so that there was virtually no focusing effect produced by the lenses.

IV. Conclusions

We have shown that order-of-magnitude improvements in the response time can be obtained in presently available photorefractive materials without loss of coupling strength. This was accomplished by using cylindrical optics to increase the intensity in the low gain direction without reducing the effective interaction length in the high gain direction. The improvements were demonstrated for beam fanning, self-pumped phase conjugation, and double phase conjugation. In addition, high fidelity images were obtained using cylindrical optics and a self-pumped phase conjugate mirror.

References

1. J. Feinberg, "Asymmetric Self-Defocusing of an Optical Beam from the Photorefractive Effect," J. Opt. Soc. Am. **72**, 46–51 (1982).

2. J. Feinberg, "Self-Pumped, Continuous-Wave Phase Conjugator Using Internal Reflection," Opt. Lett. 7, 486–488 (1982).

3. S. Weiss, S. Sternklar, and B. Fischer, "Double Phase-Conjugate Mirror: Analysis, Demonstration, and Applications," Opt. Lett. 12, 114–116 (1987).

4. M. J. Miller, E. J. Sharp, G. L. Wood, W. W. Clark III, G. J. Salamo, and R. R. Neurgaonkar, "Time Response of a Cerium-Doped $Sr_{0.75}Ba_{0.25}Nb_2O_6$ Self-Pumped Phase-Conjugate Mirror," Opt. Lett. 12, 340–342 (1987).

5. R. R. Neurgaonkar and W. K. Cory, "Progress in Photorefractive Tungsten Bronze Crystals," J. Opt. Soc. Am. B 3, 274–282 (1986).

6. M. B. Klein and R. N. Schwartz, "Photorefractive Effect in $BaTiO_3$: Microscopic Origins," J. Opt. Soc. B 3, 293–305 (1986).

7. S. P. Ducharme and J. Feinberg, "Altering the Photorefractive Properties of $BaTiO_3$ by Reduction and Oxidation at 650°C," J. Opt. Soc. Am. B 3, 283–292 (1986).

8. J. Feinberg, D. Heiman, A. R. Tanguay, Jr., and R. W. Hellwarth, "Photorefractive Effects and Light Induced Charge Migration in Barium Titanate," J. Appl. Phys. 51, 1297–1305 (1980).

9. D. Rytz, M. B. Klein, R. A. Mullen, R. N. Schwartz, G. C. Valley, and B. A. Wechsler, "High-Efficiency Fast Response in Photorefractive $BaTiO_3$ at 120°C," Appl. Phys. Lett. 52, 1759–1761 (1988).

10. D. Rytz et al., "Temperature Dependence of Photorefractive Properties of Strontium-Barium Niobate ($Sr_{0.6}Ba_{0.4}Nb_2O_6$)," J. Appl. Phys. 66, 1920–1924 (1989).

11. K. Sayano, A. Yariv, and R. R. Neurgaonkar, "Order-of-Magnitude Reduction of the Photorefractive Response Time in Rhodium-Doped $Sr_{0.6}Ba_{0.4}Nb_2O_6$ with a dc Electric Field," Opt. Lett. 15, 9–11 (1990).

12. W. W. Clark III et al., "Enhanced Photorefractive Beam Fanning Due to Internal and External Electric Fields," Appl. Opt. 29, 1249–1258 (1990).

13. G. L. Wood, W. W. Clark III, M. J. Miller, E. J. Sharp, G. J. Salamo, and R. R. Neurgaonkar, "Broadband Photorefractive Properties and Self-Pumped Phase Conjugation in Ce-SBN:60," IEEE J. Quantum Electron. QE-23, 2126–2135 (1987).

14. G. J. Salamo, M. J. Miller, W. W. Clark III, G. L. Wood, and E. J. Sharp, "Strontium Barium Niobate as a Self-Pumped Phase Conjugator," Opt. Commun. 59, 417–422 (1986).

15. B. Monson et al., "Self-Pumped Phase Conjugation with Nanosecond Pulses in Strontium Barium Niobate," Opt. Lett. 15, 12–14 (1990).

16. E. J. Sharp et al., "Double Phase Conjugation in Tungsten Bronze Crystals," Appl. Opt. 29, 743–749 (1990).

Observation of Self-Trapping of an Optical Beam Due to the Photorefractive Effect

Galen C. Duree, Jr., John L. Shultz, and Gregory J. Salamo

Department of Physics, University of Arkansas, Fayetteville, Arkansas 72701

Mordechai Segev and Amnon Yariv

California Institute of Technology, Department of Applied Physics, Pasadena, California 91125

Bruno Crosignani and Paolo Di Porto

Dipartimento di Fisica, Università dell'Aquila, L'Aquila, Italy and Fondazione Ugo Bordoni, Roma, Italy

Edward J. Sharp

Army Research Laboratory, Fort Belvoir, Virginia 22060

Ratnakar R. Neurgaonkar

Rockwell International Science Center, Thousand Oaks, California 91360

(Received 19 April 1993)

We report on the first observation of self-trapping of an optical beam due to the photorefractive effect. The self-trapping occurs at microwatt light power levels, is intensity independent, and results in significant spatial pulse reshaping.

PACS numbers: 42.65.Jx, 42.50.Rh, 42.65.Hw

Self-trapping of laser beams in nonlinear Kerr media is a well studied phenomenon [1–6] in which the diffraction effects are exactly compensated by focusing effects caused by a light induced index change. In these cases, the propagation of a light beam is spatially confined and a shape-preserving transverse profile or spatial soliton is observed. Recently, a new type of spatial soliton has been suggested [7]. It has been predicted to occur in a photorefractive medium and differs from Kerr solitons by the fact that the focusing effect is produced by an internal nonlocal space-charge dc field, as opposed to the local intensity dependent Kerr effect. A dramatic consequence of the difference in the focusing origin is that the photorefractive soliton is observable at low light powers on the order of 10 μW (intensities of about 200 mW/cm^2) or less while the observation of "bright" [5] or "dark" [6] Kerr solitons requires much higher powers. Moreover, photorefractive solitons are independent of the laser light power. As a result, they propagate while maintaining their spatial profile even in the presence of loss or gain.

In this Letter, we report the observation of photorefractive solitons. These solitons preserve their profile, which are independent of input power, and can be observed at low light powers of less than 10 μW. The degree of self-focusing due to the photorefractive index change is shown to be controllable by an applied dc voltage across the photorefractive crystal. For small applied voltages, diffraction is seen to exceed the photorefractive focusing effect and the transmitted beam is observed to diverge through the crystal. For large applied voltages, the photorefractive focusing effect exceeds diffraction and the transmitted beam is observed to converge throughout the crystal. Only for a small range of applied voltages is a shape-preserving spatial profile observed to propagate throughout the crystal. This voltage range has been predicted in Ref. [7] and is dictated by the crystal parame-

ters, such as its electro-optic coefficients, the dielectric constant, the density of traps, and the light wavelength and polarization. For very large applied voltages, photorefractive focusing greatly exceeds diffraction and the incident beam converges in the crystal to a spot size smaller than its original waist. Following the formation of the new waist, the beam diverges and is then trapped as diffraction is once again compensated for by the focusing produced via photorefraction. In all cases, the laser beam is observed to reshape and take on a "smooth" spatial profile.

For photorefractive solitons the photorefractively induced change in the index of refraction of the medium can be thought of as arising from the photorefractive two-wave mixing between all possible pairs of the plane-wave spatial-frequency spectrum of the incident laser beam [7,8]. That is, for each pair of plane-wave components of the incident beam which interferes and produces an interference grating throughout the crystal, a perturbation in the refractive index is generated $\delta n(r,z)$, where z is along the propagation direction and r is in the plane perpendicular to z. Each corresponding index grating may be viewed as a composition of two grating components: One is in phase, spatially, with the original interference pattern and the other is 90° out of phase. The in-phase component is responsible for phase coupling between the plane waves, and therefore can compensate for diffraction while the 90° phase shift component is responsible for energy exchange between each pair of spatial-frequency plane-wave components of the incident beam and for stimulated scattering or "beam fanning" [9,10]. In order to generate a nondiffracting light beam, we require $\delta n(r,z) = \delta n(-r,z)$, for all z, since diffraction is symmetric about the z axis. Following the discussion in Ref. [7] on the symmetry properties of the coupling coefficient, δn in the simple scalar 2D case, we have used

the experimental configuration suggested there. However, in this configuration, where the light propagates perpendicular to the optic axis (c axis) and a voltage is applied along the c axis, the energy-exchange process is asymmetric about the direction of propagation, and may deteriorate the shape-preserving propagation. For most of the experimental results reported here, we used external fields E_0 in the range $E_d \ll |E_0| \ll E_p$ (as suggested in Ref. [7] where E_p is the limiting space-charge field and E_d is the diffusion field) in order to minimize the out-of-phase component of the index grating and hence energy-exchange effects. Meanwhile, the relative magnitude of the in-phase gratings must be controllable in order to compensate for diffraction. This was accomplished by adjusting the value of an applied dc electric field, and by proper choice of the transverse profile of the incident light beam. For example, soliton solutions include the hyperbolic-secant and Gaussian spatial shape-preserving profiles. These solutions exist for applied fields in a range calculated using the appropriate experimental and crystal parameters in the expression given in Ref. [7].

The basic apparatus consisted of a cw argon-ion laser and a 5 mm×5 mm×6 mm strontium barium niobate (SBN) crystal with 0.01% by weight rhodium dopant. The cw argon-ion laser wavelength was 457 nm and its output beam diameter was 1.5 mm. A schematic diagram of the apparatus is shown in Fig. 1. The output beam was directed onto a 10 cm focal length lens and the SBN crystal was placed 3.6 mm beyond the beam waist of $2\omega_0 \approx 33$ μm. The beam diameter at the SBN crystal entrance face was 71 μm in the vertical plane and 81 μm in the horizontal plane. The crystal was oriented with its c axis in the horizontal plane and perpendicular to the propagation direction of the incoming laser light. The polarization of the incoming light could be varied using a polarization rotator but was initially chosen to be along the c axis (extraordinary polarization). The beam diameter throughout the crystal was measured using an imaging system consisting of an imaging lens, L_2, and a two-
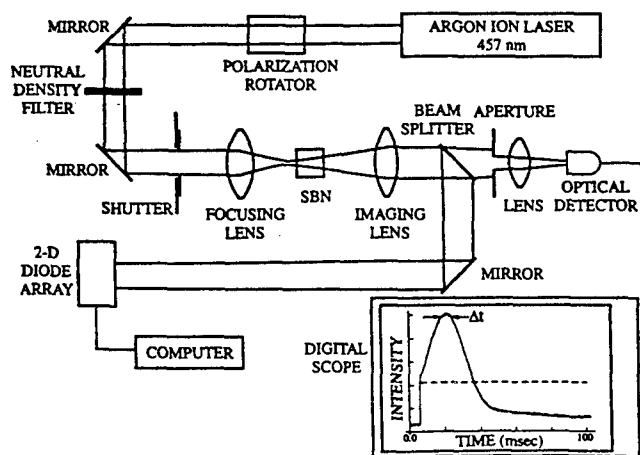
dimensional detector array. The input face of the 6 mm long SBN crystal was well beyond the Rayleigh range of 1.5 mm from the beam waist formed by the focusing lens, L_1. The imaging system, therefore, imaged the beam spot at the SBN entrance face with some magnification onto the detector array. As the imaging lens and the detector array are moved away from the SBN crystal, different cross sections of the Gaussian beam are then imaged onto the array. In this manner, the beam diameter at different locations throughout the SBN crystal was monitored. The magnification of the imaging system was determined by placing a thin aperture on the crystal exit (and entrance) face and imaging the aperture onto the detector array. Using the known value of the reference aperture, the magnification was determined to be about 15 and the positions of the exit and entrance faces of the SBN crystal were located. Using this information the horizontal cross section of the incident beam on the entrance and exit faces of the crystal was determined and is shown in Figs. 2(a) and 2(b).

A potentially serious problem in the observation of the photorefractive soliton is the interaction of the light beam with scattered light. The scattered light is amplified toward a preferential direction (given by the symmetry properties of the energy-exchange coupling coefficient, or the imaginary part of δn), and transforms the input beam into a broad fan of light. This "fanning" appears in most photorefractive crystals with nonzero energy-exchange coupling. We minimized the fanning effects by using a focused beam inside the crystal [9]. In fact with zero applied field no noticeable beam fanning was observed. Even with the applied voltage of 400 V/cm, which was

FIG. 1. Experimental apparatus used to observe photorefractive solitons.
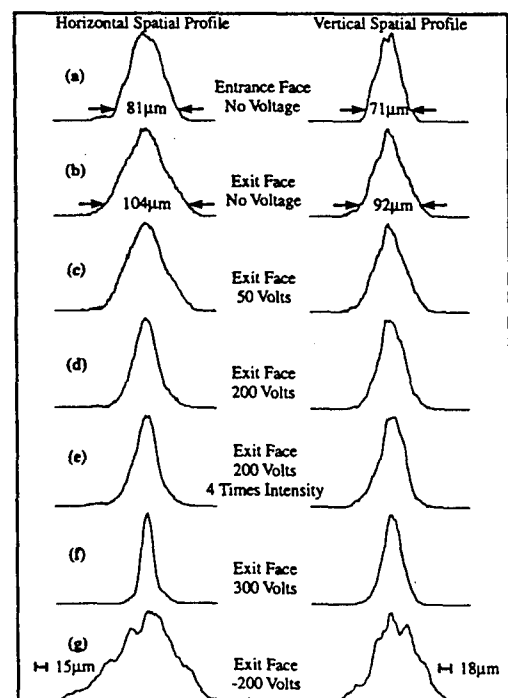

FIG. 2. The horizontal and vertical spatial beam profiles are shown for various applied voltages.

needed to observe soliton formation, beam fanning was observed to be a small effect. This was true for two reasons. First, the resulting small beam diameter provides small gain length to interactions with noise in directions that deviate significantly from $\hat{z}$ due to small interaction lengths. Second, for directions at small angles to $\hat{z}$, where large interaction lengths are possible, the gain length is again small due to small gains at the low voltage of 400 V/cm. In all directions, therefore, at voltages of 400 V/cm the gain-length product was small and beam fanning was correspondingly weak. Moreover, given that the gain length was small and the intensity modulation also small (due to the low intensity of the scattered light) the fanning which was observed was seen to form at times much longer [10,11] than the time for soliton formation. This means that for the experiment reported here, at applied voltages of 400 V/cm, soliton formation reached equilibrium before beam fanning effects needed to be considered. Consequently, a direct comparison between theory and experiment is possible. Therefore, experimentally we observed the propagating spatial profile early in time, before any beam fanning took place. This observation region is referred to as the "steady-state" region since the propagating spatial profile remained constant during this time period. This period was determined by monitoring the intensity of the incident beam after passing through the crystal and an exit aperture which was adjusted to be about the size of the incident beam. The transmission data indicated that self-focusing took place before fanning could be observed. The inset in Fig. 1 shows the total energy transmitted through the aperture as a function of time. Without an applied voltage, no self-focusing or beam fanning effects were observed (dashed curve). When self-focusing effects occurred (after applying an external dc voltage), the transmitted energy first increased, reached a steady state, and then diminished for large times (solid curve) due to screening of the applied field in the case of low applied voltages and both beam fanning and screening for large applied voltages. The steady-state region provided a window in time when diffraction effects (or solitons) could be observed with very little fanning present. For a voltage of 50 V (or an electric field of 100 V/cm) applied along the c axis, the spatial profile and beam diameter at the plane containing the crystal is shown in Fig. 2(c). The figure indicates that the beam is diverging as it propagates from the entrance face to the exit face. Comparing Fig. 2(b) to Fig. 2(c), however, it is evident that the divergence experienced by the beam along the c direction in propagating through the crystal is less with an applied field. Increasing the applied voltage to 300 V or an applied field of 600 V/cm, we can see in Fig. 2(f) that the beam now converges as it propagates through the SBN crystal. Apparently the photorefractive focusing produced with 50 V is not sufficient to compensate for diffraction while the focusing produced for 300 V overcompensates. Figure 3 shows the beam diameter and spatial profile of the laser
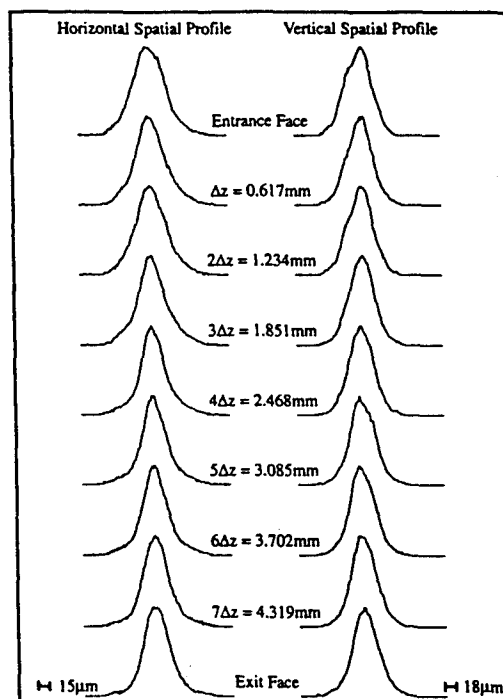

FIG. 3. Spatial beam profiles inside the crystal with 200 V.

beam propagating through the crystal with 200 V or a field of 400 V/cm applied. In this case, the beam diameter and spatial profile are observed to remain nearly constant as it propagates through the crystal and can be described as a photorefractive spatial soliton. The temporal window or steady-state region for this measurement was at least 130 msec. Experimentally, therefore, we have observed the formation of a shape-preserving propagating beam with an applied voltage in the range of 400 to 500 V/cm across the crystal. Theoretical prediction, using the parameters for our particular SBN:60 rhodium doped crystal, is also in the range of 400 to 500 V/cm. For the very large field case, $V = 3000$ V, Fig. 4 shows the beam diameter and spatial profile of the laser beam propagating through the crystal. In this case, a smooth spatial profile is more apparent. In both high and low voltage cases, a spatial soliton appears to have formed along both the c direction and the direction perpendicular to c (but with different cross section). The immediate consequence is that a soliton was formed in both transverse dimensions, a capability that was until now restricted to dark soliton stripes and grids [6]. In fact, this is the first observation, to our knowledge, of any two-dimensional bright soliton. From the temporal evolution of this high voltage soliton we infer that the perturbation in the index did *not* reach its steady state at the time at which we made the trapped-profile measurement. Unlike all other cases, where the temporal evolution had a flat, steady-state region, this high voltage case always had a temporal gradient: first due to the evolution of the soliton, then due to its breakdown (when the value of the index change exceeds the soliton upper limit), and finally due to the evolution of fanning. We have used a narrow temporal
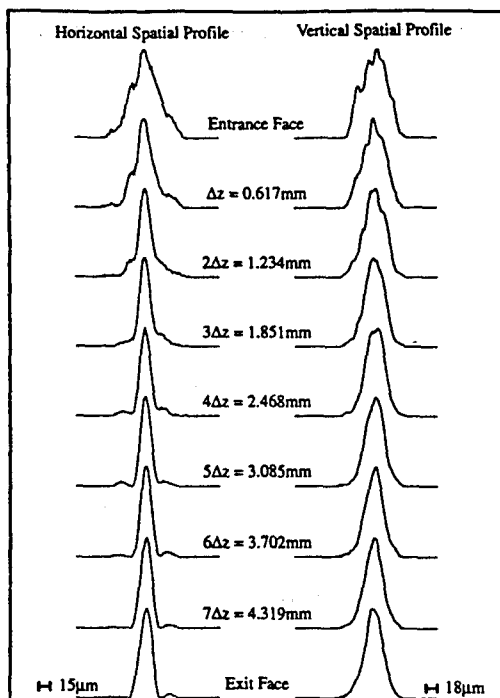
FIG. 4. Spatial beam profiles inside the crystal with 3000 V.

window of about 4 msec in this case. However, the temporal curve had a significant gradient even within this window, which indicates that the index change never reached a steady state before evolution of fanning.

In addition to comparing theory and experiment for the applied voltage range for which soliton formation is observed and predicted we also compared theory and experiment for the parameters of incident light polarization, incident light intensity, the polarity of the applied voltage, and the transverse phase of the photorefractive soliton. For example, when the polarization of the incident laser light was changed to be perpendicular to the c axis, the voltage necessary to compensate for diffraction was experimentally estimated to be about 500 to 600 V or an electric field of 1000 to 1200 V/cm. This would suggest, according to the derivation in Ref. [7], that r_{33} is an order of magnitude larger than r_{13}. This difference is consistent with published reports of this ratio. We also observed that with ordinary polarization the beam fanning appeared only after about 1 sec and was minimal during the temporal window of the measurement.

When the incident intensity was increased by a factor of 4, we observed that both the beam diameter and spatial profile were unchanged in full support of the prediction that photorefractive spatial solitons would form and be independent of the incident intensity. This is demonstrated in Figs. 2(d) and 2(e). Also, to be sure that the observed soliton propagation or formation was indeed photorefractive in origin, we intentionally interrupted the writing of the phase gratings and observed that they remained in the crystal for days but could be immediately erased with an incoherent intense light source.

Finally, when the polarity of the dc voltage was reversed, no soliton was observed. This can be explained by the sign of the in-phase part of the index grating, which causes the input beam to diverge. Intuitively, the self-generated positive lens turns into a negative self-generated lens, and increases diffraction. This is shown in Fig. 2(g). Again, these results are in full agreement with theoretical predictions.

Another issue is the transverse phase of the photorefractive soliton. In Ref. [7] it was assumed, rather than proved, that the transverse phase of the soliton is uniform. We have experimentally verified that this is the case by examining the diffraction or propagation of the exiting light beam using our imaging system. In particular, the beam exiting the crystal is observed to propagate while maintaining a smooth near Gaussian shape. Moreover, the beam diameter at the crystal exit face is seen to play the role of "minimum waist" for the beam propagating from the exit face. We have in fact recently proven theoretically that all soliton solutions possess uniform transverse phase.

Following these experimental observations, we have succeeded in showing theoretically and experimentally that the photorefractive solitons are stable in the presence of small perturbations, but break down in the case of large perturbations. The stability is manifested in the work presented here through the reshaping and the shape-preserving profiles of the solitons, *despite* the material inhomogeneities that cause the profile perturbation seen in Figs. 2(a) and 2(b).

In conclusion, we report the first observation of photorefractive spatial solitons. These observations are in full agreement with earlier theoretical predictions.

[1] R. Y. Chiao, E. Garmire, and C. H. Townes, Phys. Rev. Lett. 13, 479 (1964).
[2] V. E. Zakharov and A. B. Shabat, Zh. Eksp. Teor. Fiz. 61, 118 (1971) [Sov. Phys. JETP 34, 62 (1972)].
[3] J. E. Bjorkholm and A. Ashkin, Phys. Rev. Lett. 32, 129 (1974).
[4] A. Barthelemy, S. Maneuf, and C. Froehly, Opt. Commun. 55, 201 (1985).
[5] J. S. Aitchison, A. M. Weiner, Y. Silberberg, M. K. Oliver, J. L. Jackel, D. E. Leaird, E. M. Vogel, and P. W. Smith, Opt. Lett. 15, 471 (1990).
[6] G. A. Swartzlander, D. A. Andersen, Y. Y. Regan, H. Yin, and A. J. Kaplan, Phys. Rev. Lett. 66, 1583 (1988).
[7] M. Segev, B. Crosignani, A. Yariv, and B. Fischer, Phys. Rev. Lett. 68, 923 (1992); B. Crosignani, M. Segev, D. Engin, P. DiPorto, A. Yariv, and G. Salamo, J. Opt. Soc. Am. B 10, 446 (1993).
[8] M. Segev and A. Yariv, Opt. Lett. 16, 1938 (1991).
[9] M. Segev, Y. Ophir, and B. Fischer, Opt. Commun. 77, 265 (1990).
[10] M. Segev, D. Engin, A. Yariv, and G. C. Valley, Opt. Lett. 18, 956 (1993).
[11] H. Rajbenbach, A. Delboulbé, and J. P. Huignard, Opt. Lett. 14, 1275 (1989).

OPTICS IN 1993

Welcome to "Optics in 1993"—a roundup of principal advances in the field of optics over the past year. Each summer, OSA members are asked to submit summaries of research that, in their view, represent major progress in optics during the last year. Because the collection of summaries we receive sometimes fails to cover all areas of optics, we occasionally consult with researchers working in those sub-disciplines that were omitted.

Submissions must be technically significant, written clearly so that the community at large can grasp the subject matter, and provide sufficient information to give the reader a context of the subfield in which the accomplishment took place.

We thank those who submitted their work for "Optics in 1993" and encourage all OSA members to keep us posted on significant findings that can be included in next year's edition.

Bob D. Guenther, Guest Editor
Director of Physics
U.S. Army Research Office
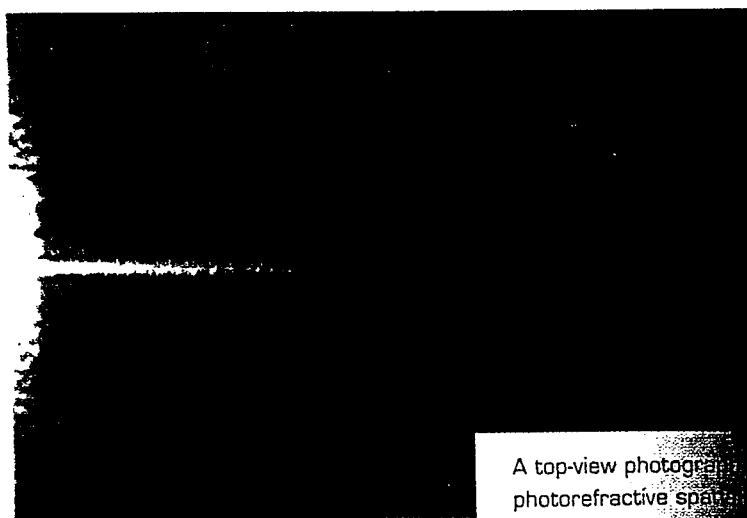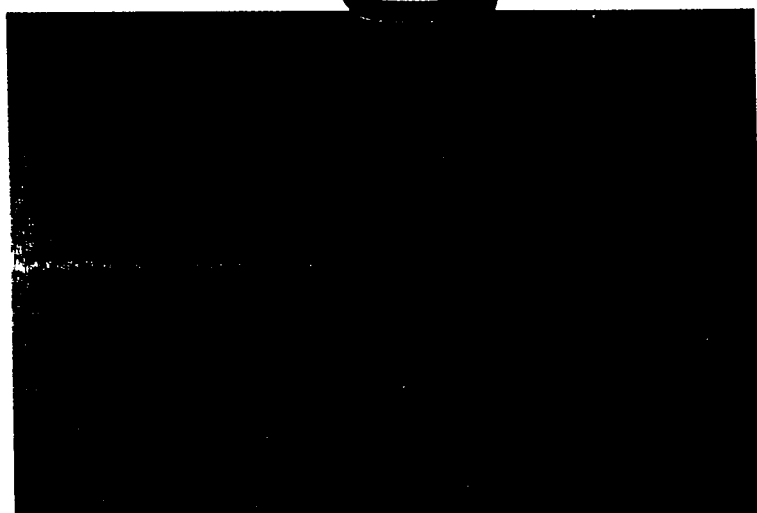
A top-view photograph photorefractive spatial soliton (above) and a normally-diffracting beam, no soliton (below).

Photorefractive Spatial Solitons

BY MORDECHAI SEGEV AND AMNON YARIV, CALIFORNIA
INSTITUTE OF TECHNOLOGY, PASADENA, CALIF.; GREGORY
SALAMO, GALEN DUREE, AND JOHN SHULTZ, UNIVERSITY
OF ARKANSAS, FAYETTEVILLE, ARK.; BRUNO CROSIGNANI
AND PAOLO DI PORTO, UNIVERSITA DELL'AQUILA,
L'AQUILA, AND FONDAZIONE UGO BORDONI, ROME, ITALY;
AND ED SHARP, ARMY RESEARCH LABORATORY, FORT
BELVOIR, VA.

L ight solitons in space (spatial solitons) exhibit a dual behavior of both waves and particles. They form when light interacts with the medium of propagation in a manner that exactly compensates for diffraction. This results in self-trapping of the light beam. It is obvious, however, that, since the medium is required to modify its properties in the presence of light, a strong light-matter interaction is required, i.e., the material must possess optical nonlinearities. All optical solitons that have thus far been discovered are a consequence of material nonlinearities that are proportional to the absolute light intensity (Kerr-like solitons). Therefore, they typically require intensities of the order of kW-MW/cm² for their operation threshold. On the other hand, photorefractive (PR) materials, which have been studied over the last two decades, possess strong nonlocal nonlinearities that do not depend upon the absolute light intensity. It was not initially obvious, however, that these materials are also capable of forming optical solitons.

We predicted the existence of photorefractive spatial solitons about two years ago.[1,2] The self-trapping effects occur when diffraction is exactly balanced by self-scattering (two-wave mixing) of the spatial (plane wave) components in the soliton beam. Since diffraction involves accumulation of phases that are linear with the propagation distance to each individual plane-wave component of the beam, it is desirable to balance it by nonlinear phase coupling. Photorefractive materials, however, typically exhibit amplitude coupling (energy-exchange interaction) due to a dominant diffusion transport mechanism for the redistribution of the photo-generated charge carriers. This, inherently, cannot compensate for diffraction, and therefore cannot form solitons. On the other hand, an external bias field (voltage) can cause strong phase coupling and is, therefore, required for the formation of PR solitons. Another consideration involves symmetry requirements. Diffraction, by its nature, is symmetrical about the axis of propagation. Since the photorefractive effect results from the electro-optic (Pockel's) effect, it possesses a complicated tensorial dependence on the angular propagation direction in the crystalline medium. We were, however, able to formulate the theory of spatial photorefractive solitons, extract their properties, and suggest configurations, materials, and crystalline orientations for practical experiments. Recently, we observed the first photorefractive spatial solitons.[3]

The experiment was performed in a 6 mm-long stron-tium barium niobate (SBN) crystal with a 10 µW laser beam from the 457 nm line of a cw argon-ion laser (intensity of about 200 mW/cm²). The beam propagated along the crystalline axis, and DC voltage was applied along the c axis. Cross sections of spatial solitons varying from 10-30 µm (FWHM) were observed, with DC fields of about 400 V/cm. Higher voltages cause the nonlinear perturbation in the index to greatly exceed diffraction, and the PR solitons break down before reaching a temporal steady state. The experimental observation is depicted in the figure, which consists of scans across a series of cross-sectional images along the propagation axis. A top-view of the observation is shown on the cover of this issue of OPN. The soliton evolves from an arbitrary input shape and the final waveform is smooth, regardless of material inhomogeneities that are seen at the entrance face in the figure shown. Unlike Kerr solitons, which are stable only in a single transverse dimension, PR solitons are formed, and remain stable, in both transverse dimensions (although with different cross sections, owing to different Pockel's coefficients). The solitons are indifferent to light intensity, and maintain the same structure with intensity variations (the signature of the PR interaction). However, the solitons could be easily erased by light using an incoherent beam from a flashlight. Reversing the polarity of the applied voltage transforms the self-induced "positive lens" into a negative one, and causes the solitonic behavior to disappear. The result is a doubling of the diffraction.[3]

REFERENCES
1. M. Segev et al., "Spatial solitons in photorefractive media," Phys. Rev. Lett. 68, 1992, 923.
2. B. Crosignani et al., "Self-trapping of optical beams in photorefractive media," JOSA B 10, 1993, 446.
3. G. C. Duree et al., "Observation of self-trapping of an optical beam due to the photorefractive effect," Phys. Rev. Lett. 71, 1993, 533.

Horizontal Spatial Profile   Vertical Spatial Profile

Entrance Face

Δz = 0.617mm

2Δz = 1.234mm

3Δz = 1.851mm

4Δz = 2.468mm

5Δz = 3.085mm

6Δz = 3.702mm

7Δz = 4.319mm

15µm   Exit Face   18µm